

Development of a Direct Evaporation Bismuth Hall Thruster

By:

Dean Richard Massey

A DISSERTATION submitted in partial fulfillment  
of the requirements for the degree of  
DOCTOR OF PHILOSOPHY  
(Mechanical Engineering-Engineering Mechanics)

MICHIGAN TECHNOLOGICAL UNIVERSITY

2008

Copyright © Dean R. Massey 2008

This dissertation, "Development of a Direct Evaporation Bismuth Hall Thruster," is hereby approved in partial fulfillment of the requirements for the degree of DOCTOR OF PHILOSOPHY in the field of Mechanical Engineering-Engineering Mechanics.

DEPARTMENT:  
Mechanical Engineering-Engineering Mechanics

Signatures:

Dissertation Advisor

\_\_\_\_\_  
Lyon B. King

Department Chair

\_\_\_\_\_  
William W. Predebon

Committee

\_\_\_\_\_  
Warren F. Perger

\_\_\_\_\_  
Jeffrey Burl

\_\_\_\_\_  
Paul Bergstrom

\_\_\_\_\_  
Richard R. Hofer

\_\_\_\_\_  
Date

*The sky doesn't ever end  
the air just gets much thinner further up  
-Modest Mouse*

## Acknowledgements

The finish line, finally. All told, my stint in graduate school lasted about 1,939 days. I would like to take this opportunity to give a nod to those who were standing next to me over the years wondering, among other things, exactly how you extinguish that hydrogen fire that is raging in front of us.

First up of course is my adviser Brad King. When I first darkened the door of the lab I didn't know a vacuum chamber from a hole in the wall. Over the years your guidance and friendship has molded me from a wide-eyed first year grad student to a competent researcher who is comfortable both inside the lab and outside. I'm honored to be your student and friend. And now on to my fellow members of the ISP Lab. The close quarters of lab sort of led to a social and emotional pressure cooker which forged a dysfunctional, yet supportive family. It was a pleasure working with each of you and I look forward to our future interactions. In order of appearance: Alex, although we didn't always see eye-to-eye (mainly because you're a solid foot taller than I am), you were always around to field my random questions I probably should not have been asking in the first place. Your insight likely kept me from leveling the lab when I started to get clever with chemicals. Emily, you're a good friend and cook. Our work didn't overlap much so all I can say is good luck with the electron flea circus. Jason, you mainly hid out in your office but when you did venture in to the lab I was always impressed by the stunning complexity of the tests that you were able to successfully run. Makela, we were thick as thieves both in the lab and out. Thank you for being such a good friend, co-worker and enabler. You're like a brother to me. Jerry, you have an uncanny ability to destroy lab equipment and also somehow take the heat when you and I are out doing questionable activities. I've enjoyed your company over the years. Finally, Carrie and Rob, you were new to the lab as I was running out the door so I didn't get much of a chance to interact with you on a technical level. However, it was a pleasure sharing the same oxygen in the lab and I'm sure you'll go far.

Outside of the walls of the ISP lab, I was supported by many other very competent hands and minds. I would like to thank Marty Toth and Jesse Nordeng (before he retired to the physics department) for performing magic with metals, ceramics and other strange materials. Much thanks to the 8<sup>th</sup> floor ladies Renee, Jo Ann and Nancy for helping me get away with murder and

tolerating late paperwork. Further down the road, Steve Forsell and Pat Quimby also had a heavy hand in this work not only by providing technical knowledge but also by allowing me to run around the M&M and play with large, dangerous materials processing equipment. When it came to electron microscopy I would like to thank Owen Mills for keeping the scopes running and also providing assistance in ~~reading clouds~~ sample analysis. I would also like to thank Dr. Pete Moran and Aaron LaLonde for letting me jump in and use (wreck?) the vacuum hot press.

I would also like to thank my small army of committee members: Bill Predebon, Warren Perger, Jeff Burl, Paul Bergstrom, and Rich Hofer. Thank you for your insight and feedback in this work. As Brad mentioned in his thesis, any mistakes left now are my own.

I would also like to thank the Air Force Office of Scientific Research (AFOSR) under the guidance of Dr. Mitat Birkan and the Michigan Space Grand Consortium for providing financial support and to Aerojet for providing hardware, spare parts and technical support.

Finally, I would like to thank my family and friends for hanging in there with me and occasionally tugging my head out of the clouds. I could not have done it without you. Now read on, it is a good story.

~Dean

September 1<sup>st</sup>, 2008

## **Abstract**

Hall thrusters have been under active development around the world since the 1960's. Thrusters using traditional propellants such as xenon have been flown on a variety of satellite orbit raising and maintenance missions with an excellent record. To expand the mission envelope, it is necessary to lower the specific impulse of the thrusters but xenon and krypton are poor performers at specific impulses below 1,200 seconds.

To enhance low specific impulse performance, this dissertation examines the development of a Hall-effect thruster which uses bismuth as a propellant. Bismuth, the heaviest non-radioactive element, holds many advantages over noble gas propellants from an energetics as well as a practical economic standpoint. Low ionization energy, large electron-impact cross-section and high atomic mass make bismuth ideal for low-specific impulse applications. The primary disadvantage lies in the high temperatures which are required to generate the bismuth vapors. Previous efforts carried out in the Soviet Union relied upon the complete bismuth vaporization and gas phase delivery to the anode. While this proved successful, the power required to vaporize and maintain gas phase throughout the mass flow system quickly removed many of the efficiency gains expected from using bismuth.

To solve these problems, a unique method of delivering liquid bismuth to the anode has been developed. Bismuth is contained within a hollow anode reservoir that is capped by a porous metallic disc. By utilizing the inherent waste heat generated in a Hall thruster, liquid bismuth is evaporated and the vapors pass through the porous disc into the discharge chamber. Due to the high temperatures and material compatibility requirements, the anode was fabricated out of pure molybdenum. The porous vaporizer was not available commercially so a method of creating a refractory porous plate with 40-50% open porosity was developed. Molybdenum also does not

respond well to most forms of welding so a diffusion bonding process was also developed to join the molybdenum porous disc to the molybdenum anode.

Operation of the direct evaporation bismuth Hall thruster revealed interesting phenomenon. By utilizing constant current mode on a discharge power supply, the discharge voltage settles out to a stable operating point which is a function of discharge current, anode face area and average pore size on the vaporizer. Oscillations with a 40 second period were also observed.

Preliminary performance data suggests that the direct evaporation bismuth Hall thruster performs similar to xenon and krypton Hall thrusters. Plume interrogation with a Retarding Potential Analyzer confirmed that bismuth ions were being efficiently accelerated while Faraday probe data gave a view of the ion density in the exhausted plume.

# Table of Contents

<b>ACKNOWLEDGEMENTS .....</b>	<b>I</b>
<b>ABSTRACT .....</b>	<b>III</b>
<b>TABLE OF CONTENTS.....</b>	<b>V</b>
<b>LIST OF FIGURES .....</b>	<b>IX</b>
<b>NOMENCLATURE .....</b>	<b>XV</b>
<b>1. INTRODUCTION .....</b>	<b>1</b>
1.1 ORBITAL FUNDAMENTALS.....	2
1.2 ORBITAL MANEUVERS .....	4
1.3 INTRODUCTION TO ROCKET PROPULSION .....	6
1.4 INTRODUCTION TO ELECTRIC PROPULSION .....	8
1.5 HALL-EFFECT THRUSTER OVERVIEW .....	10
1.6 CURRENT STATE OF THE ART HALL THRUSTERS AND ASSOCIATED LIMITS.....	12
1.7 CONTRIBUTION OF RESEARCH AND DOCUMENT ROADMAP .....	13
<b>2. INTRODUCTION TO BISMUTH .....</b>	<b>15</b>
2.1 PHYSICAL ATTRIBUTES OF BISMUTH .....	15
2.2 ADVANTAGES OF BISMUTH AS A PROPELLANT.....	20
2.3 DISADVANTAGES OF BISMUTH AS A PROPELLANT .....	33
2.4 OTHER BISMUTH HALL THRUSTER EFFORTS.....	35
2.4.1 <i>TsNIIMASH D-160 and D-200.....</i>	<i>35</i>
2.4.2 <i>Very High Specific Impulse Thruster Anode Layer - 160 (VHITAL).....</i>	<i>37</i>
2.4.3 <i>Busek Bismuth Hall Thruster.....</i>	<i>40</i>

2.5	SUMMARY .....	40
<b>3.</b>	<b>DIRECT EVAPORATION OF BISMUTH .....</b>	<b>41</b>
3.1	EVAPORATION KINETICS .....	42
3.2	EVAPORATION OF BISMUTH .....	44
3.3	THE POROUS VAPORIZER .....	49
3.4	THERMAL CONTROL WITH SEGMENTED ANODES .....	52
3.5	SUMMARY .....	54
<b>4.</b>	<b>EXPERIMENTAL DEVELOPMENT OF THE BISMUTH HALL THRUSTER .....</b>	<b>55</b>
4.1	THERMAL MODELING .....	56
4.2	TESTING FACILITIES AND INSTRUMENTATION .....	63
4.3	SEGMENTED ANODE XENON PERFORMANCE .....	65
4.4	BISMUTH AS AN ENGINEERING MATERIAL .....	71
4.5	POROUS VAPORIZER DESIGN AND EXTRUSION TESTING .....	76
4.6	MIXED XENON-BISMUTH OPERATION .....	80
4.7	MOLYBDENUM SHIM ANODES.....	87
4.8	SHIM-LESS OPERATION .....	89
4.9	VAPORIZER THERMAL FAILURES .....	91
4.10	RESISTIVE PRE-HEATING.....	95
4.11	BISMUTH PROPELLANT FLOW .....	97
4.12	SUMMARY .....	100
<b>5.</b>	<b>FABRICATION OF THE BISMUTH HALL THRUSTER .....</b>	<b>101</b>
5.1	STAINLESS-STEEL ANODES .....	101
5.2	BISMUTH HYDROSTATIC RESERVOIR.....	103
5.3	MOLYBDENUM ANODES.....	104

5.3.1	<i>Introduction to Powder Metallurgy</i> .....	104
5.3.2	<i>Previous Porous Tungsten and Molybdenum Efforts</i> .....	106
5.3.3	<i>Initial Porous Vaporizer Fabrication Efforts</i> .....	107
5.3.4	<i>Porous Mo Sintered in a Vacuum Hot Press</i> .....	116
5.3.5	<i>Bonding the Porous Vaporizer to a Solid Mo Body</i> .....	121
5.3.6	<i>Integrating Bismuth Reservoir with Mo Anode</i> .....	123
5.3.7	<i>Monolithic Molybdenum Anode</i> .....	125
5.4	SUMMARY .....	127
<b>6.</b>	<b>OPERATION OF THE BISMUTH HALL THRUSTER</b> .....	<b>128</b>
6.1	ANATOMY OF A BISMUTH TEST .....	128
6.1.1	<i>Warm-up</i> .....	129
6.1.2	<i>Ignition Transients</i> .....	130
6.1.3	<i>Steady State</i> .....	131
6.1.4	<i>Cool down</i> .....	131
6.2	OPERATIONAL TRANSIENTS .....	132
6.3	PRELIMINARY DIAGNOSTICS .....	133
6.3.1	<i>Thermal Imaging</i> .....	134
6.3.2	<i>Plume Characterization</i> .....	136
6.3.3	<i>Ion Energy Analysis</i> .....	139
6.4	SUMMARY .....	142
<b>7.</b>	<b>CONCLUSIONS</b> .....	<b>143</b>
7.1	BISMUTH AS A PROPELLANT .....	144
7.2	DIRECT EVAPORATION .....	144
7.3	THERMAL CONTROL WITH SEGMENTED ANODES .....	145

7.4	BISMUTH MATERIALS COMPATIBILITY .....	146
7.5	STAINLESS STEEL VAPORIZER FAILURES.....	147
7.6	MOLYBDENUM ANODES AND MOLYBDENUM POWDER METALLURGY .....	147
7.7	THRUSTER OPERATION AND DIAGNOSTICS .....	148
<b>APPENDICES .....</b>		<b>151</b>
<b>WORKS CITED .....</b>		<b>188</b>

# List of Figures

FIGURE 1: SCHEMATIC OF A HALL-EFFECT THRUSTER AS SHOWN IN REF [7]. REPRINTED WITH PERMISSION. PERMISSION LETTER CAN BE FOUND IN APPENDIX D.	11
FIGURE 2: SOLID BISMUTH	17
FIGURE 3: MAXIMUM THEORETICAL VOLTAGE EFFICIENCY AS A FUNCTION OF SPECIFIC IMPULSE	23
FIGURE 4: ELECTRON IMPACT IONIZATION CROSS SECTIONS FOR $\text{Bi}^{+1}$ , $\text{Bi}^{2+}$ AND $\text{Bi}^{3+}$	25
FIGURE 5: FIRST ELECTRON-IMPACT IONIZATION CROSS-SECTIONS OF BISMUTH AND XENON	25
FIGURE 6: OPTIMUM SPECIFIC IMPULSE FOR 30%, 50% AND 70% EFFICIENCIES AND A SPECIFIC MASS OF 10 KG/KW.	28
FIGURE 7: THRUST-TO-POWER RATIO AS A FUNCTION OF SPECIFIC IMPULSE ILLUSTRATING THE NICHE FOR BISMUTH.	30
FIGURE 8: SCHEMATIC OF THE TSNIIMASH FEED SYSTEM: 1) BISMUTH RESERVOIR, 2) VAPORIZER, 3) MOLYBDENUM PROPELLANT TUBE, 4) ELECTRICAL CONNECTION FOR THE VAPORIZER.	37
FIGURE 9: BLOCK DIAGRAM OF THE FLIGHT-LIKE BISMUTH FEED SYSTEM ASSEMBLY FOR VHITAL.	38
FIGURE: 10 VHITAL BISMUTH VAPORIZER.	39
FIGURE 11: A ILLUSTRATION OF AN OPEN POOL OF BISMUTH EVAPORATING IN A DISCHARGE CHAMBER. THE DASHED LINE REPRESENTS THE BOUNDARY WHERE IF GAS MOLECULES PASS, IT IS ASSUMED THEY WILL NOT RETURN.	42
FIGURE 12: FUNCTIONAL DIAGRAM OF A GAS PHASE BISMUTH HALL THRUSTER SHOWING THE VARIOUS HEATERS AND APPROXIMATE TEMPERATURES REQUIRED	45
FIGURE 13: VAPOR PRESSURE VS TEMPERATURE AND EVAPORATION RATE VS TEMPERATURE FOR BISMUTH	46
FIGURE 14: FUNCTIONAL DIAGRAM OF A LIQUID FED BISMUTH HALL THRUSTER UTILIZING DIRECT EVAPORATION	48
FIGURE 15: ILLUSTRATION OF CONTACT ANGLES: A) WETTING B) NON-WETTING.	50
FIGURE 16: SCHEMATIC OF INTERFACIAL FORCES IN RESPONSE TO A NON-WETTING FLUID IMPINGING ON A CAPILLARY	51
FIGURE 17: EVAPORATION SCHEMATIC SHOWING BISMUTH EVAPORATING FROM THE FREE SURFACE CREATED BY THE POROUS PLATES AND THE ELECTRONS DEPOSITING HEAT TO DRIVE THE EVAPORATION.	52
FIGURE 18 SEGMENTED ANODE THRUSTER	53

FIGURE 19: ELECTRONS IMPACTING AND DEPOSITING HEAT TO DRIVE DIRECT EVAPORATION	54
FIGURE 20: ORIGINAL UNMODIFIED AEROJET BPT-200 MOUNTED ON A THRUST STAND	57
FIGURE 21: SOLID MODEL SHOWING THE PARTS USED DURING THERMAL MODELING: 1) ANODE FACE, 2) ELECTROMAGNETS, 3) OUTER SHIM ANODE, 4) INNER SHIM ANODE, 5) FRONT PLATE, 6) BACK PLATE, 7) INNER BN GUARD RING, 8) OUTER BN GUARD RING, 9) CENTER MAGNETIC POLE AND 10) BN BODY.	58
FIGURE 22: SELECTED IDEAS THERMAL MODELS WITH DIFFERENT LOADS ON THE ANODES.	62
FIGURE 23: XENON TEST FACILITY	63
FIGURE 24: CONDENSABLE PROPELLANT FACILITY	64
FIGURE 25 - RESULTS FROM A TYPICAL OPERATING POINT. MAIN ANODE VOLTAGE IS $V_{\text{MAIN}} = 400$ VOLTS AND FLOW IS 6 MG/S OF XENON. EXPERIMENTAL ERROR FOR EFFICIENCY AND $I_{\text{sp}}$ IS +/- 5% OF THE VALUE.	66
FIGURE 26 - THRUSTER PERFORMANCE RESULTS SHOWING THE VARIATION IN ANODE EFFICIENCY AND SPECIFIC IMPULSE AS THE DISCHARGE CURRENT IS SHIFTED BETWEEN MAIN ANODE AND SHIMS. EXPERIMENTAL ERROR FOR EFFICIENCY AND $I_{\text{sp}}$ IS +/- 5% OF THE VALUE.	67
FIGURE 27 - THRUSTER THERMAL VARIATION DUE TO VARYING CURRENT ATTACHMENT. MAIN ANODE VOLTAGE WAS HELD CONSTANT AT 400 VOLTS	68
FIGURE 28 - TYPICAL OPERATING PERFORMANCE	70
FIGURE 29: CROSS-SECTION OF A BISMUTH BOILER WITH A HEATER ISOLATED FROM LIQUID BISMUTH	72
FIGURE 30: BISMUTH BOILER WITH ADDITIONAL STAINLESS STEEL DIFFUSER PLATES	73
FIGURE 31: COPPER ANODE DAMAGED BY HIGH TEMPERATURE BISMUTH	74
FIGURE 32: BISMUTH-COPPER PHASE DIAGRAM FROM REF. [56]. ACCORDING TO THE PHASE DIAGRAM, A COPPER SUBSTRATE SHOULD NOT BE EXPECTED TO WITHSTAND MOLTEN BISMUTH. REPRINTED WITH PERMISSION OF ASM INTERNATIONAL®. ALL RIGHTS RESERVED. PERMISSION LETTER CAN BE FOUND IN APPENDIX D.	75
FIGURE 33: BISMUTH WETTING TESTS ON STAINLESS STEEL (A), MOLYBDENUM (B) AND TUNGSTEN (C) SUBSTRATES. IN ALL CASES THE CONTACT ANGLE EXCEEDS 90° THEREFORE BISMUTH IS NON-WETTING ON THESE MATERIALS	77
FIGURE 34: APPARATUS FOR TESTING BISMUTH EXTRUSION PRESSURES	78

FIGURE 35: A HIGH-MAGNIFICATION SEM IMAGE OF A COMMERCIALY PURCHASED 10 $\mu$ M AVERAGE PORE SIZE POROUS STAINLESS STEEL PLATE	80
FIGURE 36: DUAL PROPELLANT ANODE CROSS-SECTION	81
FIGURE 37: SEM IMAGE OF THE 2.54 MM THICK POROUS STAINLESS STEEL PLATE	82
FIGURE 38: FRAME FROM A VIDEO TAKEN DURING THE FIRST DIRECT EVAPORATION BISMUTH TEST	83
FIGURE 39: DUAL PROPELLANT ANODE WITH AN INNER SHIM MELTED TO IT AFTER TESTING (LEFT) AND A PHOTO OF THE POROUS VAPORIZER AFTER TESTING SHOWING THE CRUDE TIG WELD (RIGHT)	84
FIGURE 40: PHOTO OF A DUAL PROPELLANT ANODE WITH FURTHER REDUCED FACE AREA AND A VACUUM ROTARY TIG WELDED POROUS PLATE	85
FIGURE 41 - BISMUTH HALL THRUSTER RUNNING AT 4kW	86
FIGURE 42 - CURRENT, POWER AND XENON FLOW DURING A TRANSITION. DISCHARGE VOLTAGE WAS INITIALLY HELD AT 400 VOLTS UNTIL XENON FLOW WAS REMOVED AND THE DISCHARGE WAS HELD AT A CONSTANT CURRENT.	87
FIGURE 43: PHOTO OF A MELTED STAINLESS STEEL SHIM ANODE (LEFT) AND A NEW MOLYBDENUM SHIM ANODE (RIGHT).	88
FIGURE 44: REPRESENTATIVE DATA SHOWING XENON MASS FLOW RATE, DISCHARGE VOLTAGE AND DISCHARGE CURRENT.	90
FIGURE 45 I-V CHARACTERISTICS FOR TYPICAL HET AT DIFFERENT MASS FLOW RATES ILLUSTRATING HOW DISCHARGE VOLTAGE COMPENSATES FOR VARYING MASS FLOWS.	91
FIGURE 46: VIEWS OF THE BISMUTH HALL THRUSTER IN OPERATION. THE LEFT PHOTOS WERE TAKEN LOOKING DIRECTLY INTO THE DISCHARGE CHAMBER AND THE RIGHT PHOTOS WERE TAKEN AT AN ANGLE TO SEE THE PLUME. TOP – BISMUTH THRUSTER DURING NORMAL OPERATION. BOTTOM – BISMUTH THRUSTER RUNNING WITH A POROUS VAPORIZER IN THE EARLY STAGES OF FAILURE.	93
FIGURE 47: CROSS SECTION OF THE INTEGRATED RESISTIVE HEATER WITH THE FOLLOWING PARTS: 1) UPPER BORON-NITRIDE BODY PART, 2) LOWER BORON-NITRIDE BODY PART, 3) ANODE, 4) UPPER BORON-NITRIDE INSULATOR AND 5) LOWER BORON-NITRIDE INSULATOR WITH GROOVES FOR THE RHENIUM DOPED TUNGSTEN WIRE.	96
FIGURE 48: PHOTO OF THE BORON-NITRIDE HEATER INSULATORS. LEFT IS THE LOWER PART, RIGHT IS THE UPPER PART.	96
FIGURE 49: TYPICAL XENON ANODE WITH GAS BEING FED FROM THE REAR	98

FIGURE 50 BISMUTH ANODE CONFIGURATIONS: A) TRADITIONAL REAR-FED STYLE AND B) VERTICALLY FED	99
FIGURE 51: WELDED ANODES, ROTARY TIG WELDING (LEFT) AND ELECTRON BEAM WELDING (RIGHT).	103
FIGURE 52: ILLUSTRATION OF THE TWO PARTICLE SINTERING PROCESS. 1) TWO PARTICLES IN CONTACT, 2) DURING INITIAL SHORT SINTERING TIME NECK GROWTH HAS BEGUN AND CREATED A GRAIN BOUNDARY BETWEEN THE TWO PARTICLES, 3) DURING INTERMEDIATE SINTERING TIME, NECK GROWTH CONTINUES AND THE GRAIN BOUNDARY EXPANDS AND 4) AFTER AN INFINITE AMOUNT OF TIME, THE TERMINAL CONDITION OF TWO COALESCED PARTICLES IS REACHED.	105
FIGURE 53 – MOLYBDENUM POWDER HEATED FOR 2 HOURS AT 950°C IN HYDROGEN ENVIRONMENT SHOWING LITTLE SINTERING	110
FIGURE 54 – MOLYBDENUM POWDER HEATED TO 1200°C FOR 30 MINUTES IN VACUUM.	111
FIGURE 55 – MOLYBDENUM POWDER AFTER 20 MINUTES IN A VACUUM INDUCTION FURNACE	113
FIGURE 56 - HEAT TREATING FURNACE INSTALLED IN THE VACUUM CHAMBER	114
FIGURE 57 – MOLYBDENUM SINTERED FOR 20 HOURS AT 1100°C UNDER VACUUM	115
FIGURE 58 - COMPLETED POROUS VAPORIZER DISCS	115
FIGURE 59 - FESEM IMAGE OF POROUS MOLYBDENUM BONDED BETWEEN LAYERS OF CARBON	117
FIGURE 60 - SEM IMAGE (LEFT) AND X-RAY ELEMENT MAP (RIGHT) OF THE POROUS MOLYBDENUM-CARBON INTERFACE	119
FIGURE 61 - LOW MAGNIFICATION FESEM IMAGE OF A HOT PRESSED POROUS MOLYBDENUM DISC	120
FIGURE 62 - HIGH MAGNIFICATION FESEM IMAGE OF A HOT PRESSED MOLYBDENUM DISC SHOWING FAVORABLE SINTERING	120
FIGURE 63 - A SEM IMAGE OF A DIFFUSION BOND. POROUS MOLYBDENUM (TOP) IS BONDED TO FULL DENSITY MOLYBDENUM (BOTTOM).	122
FIGURE 64: EDGE-ON PHOTO OF A COMPLETED MOLYBDENUM ANODE WITH DIFFUSION BONDED POROUS FACE	123
FIGURE 65: COMPLETED ANODE WITH DIFFUSION BONDED POROUS PLATE AND ELECTRON BEAM WELDED PROPELLANT TUBE	124
FIGURE 66: CRACK IN THE PROPELLANT LINE WELD	125
FIGURE 67: THE COMPLETED MONOLITHIC MOLYBDENUM ANODE ASSEMBLY	127
FIGURE 68: EXAMPLE OPERATIONAL CURVE OF A BISMUTH THRUSTER TEST	129
FIGURE 69: PLOT OF THRUST SHOWING A TRANSIENT OSCILLATION WITH A 42 SECOND PERIOD	132

FIGURE 70: TRANSMISSION CHARACTERISTICS OF THE SAPPHIRE WINDOW AS PROVIDED BY THE VENDOR KURT J. LESKER CO.	135
FIGURE 71: THERMAL IMAGE OF THE THRUSTER AFTER A THREE HOUR STEADY STATE RUN	136
FIGURE 72: SCHEMATIC OF A FARADAY PROBE	137
FIGURE 73: PHOTO OF A FARADAY PROBE WITH A DIME FOR SIZE COMPARISON	137
FIGURE 74: FARADAY PROBE SWEEP OF THE BISMUTH PLUME RUNNING AT A DISTANCE 250 MM, 382 VOLTS AND 4.5 AMPS OF DISCHARGE CURRENT	138
FIGURE 75: FARADAY SWEEP OF A XENON THRUSTER AT 400 VOLTS AND 6MG/S MASS FLOW FROM REF [55]. 42 DEG	139
FIGURE 76: SCHEMATIC OF A RETARDING POTENTIAL ANALYZER	140
FIGURE 77: RETARDING POTENTIAL ANALYZER DATA FOR THE BISMUTH THRUSTER RUNNING AT 383 VOLTS	141
FIGURE 78: RPA DATA FROM A XENON THRUSTER RUNNING AT 350 VOLTS, 5MG/S AT A DISTANCE OF 500 MM. FIGURE FROM REF [55].	142
FIGURE 79: SILVER-BISMUTH PHASE DIAGRAM FROM REF. [72]. ACCORDING TO THE PHASE DIAGRAM, A SILVER SUBSTRATE SHOULD NOT BE EXPECTED TO WITHSTAND MOLTEN BISMUTH. REPRINTED WITH PERMISSION OF ASM INTERNATIONAL®. ALL RIGHTS RESERVED. PERMISSION LETTER CAN BE FOUND IN APPENDIX D.	151
FIGURE 80: BISMUTH-ALUMINUM PHASE DIAGRAM FROM REF. [73]. ACCORDING TO THE PHASE DIAGRAM, AN ALUMINUM SUBSTRATE SHOULD NOT BE EXPECTED TO WITHSTAND MOLTEN BISMUTH. REPRINTED WITH PERMISSION OF ASM INTERNATIONAL®. ALL RIGHTS RESERVED. PERMISSION LETTER CAN BE FOUND IN APPENDIX D.	152
FIGURE 81: BISMUTH-COBALT PHASE DIAGRAM FROM REF. [73]. ACCORDING TO THE PHASE DIAGRAM, A COBALT SUBSTRATE SHOULD NOT BE EXPECTED TO WITHSTAND MOLTEN BISMUTH. REPRINTED WITH PERMISSION OF ASM INTERNATIONAL®. ALL RIGHTS RESERVED. PERMISSION LETTER CAN BE FOUND IN APPENDIX D.	153
FIGURE 82: BISMUTH-COPPER PHASE DIAGRAM FROM REF. [56]. ACCORDING TO THE PHASE DIAGRAM, A COPPER SUBSTRATE SHOULD NOT BE EXPECTED TO WITHSTAND MOLTEN BISMUTH. REPRINTED WITH PERMISSION OF ASM INTERNATIONAL®. ALL RIGHTS RESERVED. PERMISSION LETTER CAN BE FOUND IN APPENDIX D.	154

FIGURE 83: BISMUTH-IRON PHASE DIAGRAM FROM REF. [74]. ACCORDING TO THE PHASE DIAGRAM, IRON WILL HAVE SOME HIGH TEMPERATURE SUSCEPTIBILITY TO MOLTEN BISMUTH. REPRINTED WITH PERMISSION OF ASM INTERNATIONAL®. ALL RIGHTS RESERVED. PERMISSION LETTER CAN BE FOUND IN APPENDIX D.	155
FIGURE 84: BISMUTH-MOLYBDENUM PHASE DIAGRAM FROM REF. [74, 75]. ACCORDING TO THE PHASE DIAGRAM, THE USE OF MOLYBDENUM IN A MOLTEN BISMUTH ENVIRONMENT SHOULD NOT CREATE ANY ADVERSE MATERIAL COMPATIBILITY ISSUES. REPRINTED WITH PERMISSION OF ASM INTERNATIONAL®. ALL RIGHTS RESERVED. PERMISSION LETTER CAN BE FOUND IN APPENDIX D.	156
FIGURE 85: BISMUTH-NICKEL PHASE DIAGRAM FROM REF. [75]. ACCORDING TO THE PHASE DIAGRAM, A NICKEL SUBSTRATE SHOULD NOT BE EXPECTED TO WITHSTAND MOLTEN BISMUTH. REPRINTED WITH PERMISSION OF ASM INTERNATIONAL®. ALL RIGHTS RESERVED. PERMISSION LETTER CAN BE FOUND IN APPENDIX D.	157
FIGURE 86: BISMUTH-PLATINUM PHASE DIAGRAM FROM REF. ACCORDING TO THE PHASE DIAGRAM, A PLATINUM SUBSTRATE SHOULD NOT BE EXPECTED TO WITHSTAND MOLTEN BISMUTH. REPRINTED WITH PERMISSION OF ASM INTERNATIONAL®. ALL RIGHTS RESERVED. PERMISSION LETTER CAN BE FOUND IN APPENDIX D.	158
FIGURE 87: BISMUTH-TITANIUM PHASE DIAGRAM FROM REF. [76]. ACCORDING TO THE PHASE DIAGRAM, A TITANIUM SUBSTRATE SHOULD NOT BE EXPECTED TO WITHSTAND MOLTEN BISMUTH. REPRINTED WITH PERMISSION OF ASM INTERNATIONAL®. ALL RIGHTS RESERVED. PERMISSION LETTER CAN BE FOUND IN APPENDIX D.	159
FIGURE 88: PREPARED DIE WITH BORON-NITRIDE COATED RAMS	162
FIGURE 89: DIFFUSION BONDED ANODE IMMEDIATELY AFTER BONDING	168
FIGURE 90: PHOTOGRAPH OF THE LIQUID COOLED FREEZING VALVE	170
FIGURE 91: CLOSE VIEW OF THE TUNGSTEN HEATER WIRE INSTALLED IN THE LOWER BORON-NITRIDE INSULATOR	173
FIGURE 92: PHOTOGRAPH OF THE ANODE HEATER BEFORE THE UPPER BN INSULATOR IS INSTALLED	174
FIGURE 93: PHOTOGRAPH OF THE ANODE AND ANODE HEATER INSTALLED	175
FIGURE 94: ELECTRICAL SCHEMATIC	178
FIGURE 95: FUNCTIONAL DIAGRAM OF THE FREEZING VALVE PURGE SYSTEM.	180
FIGURE 96: THRUSTER MOUNTED ON THE THRUST STAND READY TO RUN	181

## Nomenclature

$a$	Semi-major axis length (m)
$A$	Area ( $m^2$ )
$e$	Elementary electric charge ( $1.6022 \times 10^{-19}$ C)
$E_{\text{ion}}$	Ionization energy (eV)
$F_{\text{esc}}$	Velocity distribution function of escaping particles (s/m)
$g$	Acceleration due to gravity ( $9.8 \text{ m/s}^2$ )
$G$	Gravitational constant ( $6.6732 \times 10^{-11} \text{ m}^3/\text{kg s}^2$ )
$I$	Current (A)
$I_{\text{sp}}$	Specific impulse (s)
$k$	Boltzmann constant ( $1.380710^{-23} \text{ J/ kg K}$ )
$M$	Mass of the Earth
$m$	Mass of particle (m)
$m_i$	Initial mass (kg)
$m_f$	Final mass (kg)
$\dot{m}$	Mass flow rate (mg/s)
$P_{\text{ion}}$	Power required to ionize (W)
$P_{\text{kin}}$	Kinetic power (W)
$P_s$	System power (W)
$P_{\text{st}}$	Surface tension pressure (Pa)
$q$	Charge (C)
$r$	Radius (m)
$t$	Time (s)
$T$	Thrust (N), temperature (C, K)
$U_g$	Gravitational potential energy (J)
$\Delta v$	Change in orbit velocity (km/s)

$v$	Velocity (m/s)
$v_e$	Exhaust velocity (m/s)
$v_{th}$	Thermal velocity (m/s)
$V$	Voltage (V)
$V_{dis}$	Anode discharge voltage (V)
$\beta$	Power system specific mass (kg/kW)
$\gamma$	Surface energy (mN/m <sup>2</sup> )
$\varepsilon$	Emissivity
$\eta_a$	Anode efficiency
$\eta_b$	Current utilization efficiency
$\eta_c$	Cathode neutralizer efficiency
$\eta_m$	Magnetic efficiency
$\eta_p$	Propellant utilization efficiency
$\eta_q$	Charge utilization efficiency
$\eta_T$	Total efficiency
$\eta_v$	Voltage utilization efficiency
$\theta$	Angle (deg)
$\theta_c$	Contact angle (deg)
$\sigma$	Cross-section (m <sup>2</sup> )
$\tau$	Trip time (s)
$\mu$	Standard gravitational parameter (GM = 398,600 km <sup>3</sup> /s <sup>2</sup> )

# 1. Introduction

At this point in history, there is no escaping the integral part that space, despite being comprised of essentially nothing, plays in our daily lives. From the mundane communications satellites to the more obscure weather and spy satellites and even out to those craft whose lenses, detectors and antennas point away from Earth, their common need of propulsion, navigation, power and communications has created an industry with the single-minded focus of creating the most efficient, reliable and precise tools for the job.

We are all familiar with the images and video of the rockets of days past and present erupting in a glorious controlled explosion which somehow move the equivalent of a 36-story building in the intangible void of space from which it might return though looking much worse for wear and significantly smaller in size. While this unbridled expulsion of pure power is certainly necessary to get off the ground and into orbit, the same cannot be said for craft already in orbit where the usually oppressive force of gravity and the stuffy atmosphere have given way to a simple nagging downward pointing vector and a faint wisp of an annoyance. It is in this realm where it is prudent to switch from the more familiar burn-and-exhaust sort of propulsion to one that can take advantage of the inherent environment of space.

This dissertation will examine only a small aspect of a relatively small field whose focus is very efficient in-space propulsion; more specifically electric propulsion systems but first some general background information is in order. Section 1.1 will introduce so basics of orbital fundamentals which will be used to explain the orbital maneuvers described in Section 1.2. In Section 1.3, the fundamentals for rocket propulsion will be explained. Building on the previous section, Section 1.4 will introduce electric-propulsion as a way to more efficiently perform appropriate missions. Section 1.5, will briefly examine the Hall-effect electric propulsion thruster

and Section 1.6 will report on the current state-of-the-art Hall thrusters. The introductory material will conclude in Section 1.7 where the contribution of research and a roadmap of this dissertation will be presented

## ***1.1 Orbital Fundamentals***

We're stuck on Earth, bound by the relentless yet invisible force of gravity and no amount of jumping or climbing seems to alleviate the situation. The gravitational field created by the enormous mass of the Earth will always pull you back to the surface. How then do all the gadgets we've sent into orbit remain there? Therein lays the trick: they are in orbit – they have not escaped Earth's gravity either. Their kinetic energy and the relative lack of retarding effects allow our satellites to remain above the surface with no active propulsion, seemingly in open defiance of gravity. The mathematical reality of the situation is actually a bit different. The gravitational potential energy,  $U_g$ , is given by

$$U_g = -\frac{GMm}{r} \quad (1.1)$$

where  $G$  is the universal gravitational constant,  $M$  is the mass of the Earth,  $m$  is the mass of some object and  $r$  is the distance between them.

An object moving has a kinetic energy, which is proportional to its mass and the square of its velocity. Equation (1.1) can be combined with the kinetic energy term to yield Equation (1.2) which is an expression relating the change in kinetic energy with the change in gravitational potential energy where  $v$  is the velocity of the object of mass  $m$ .

$$\left(\frac{1}{2}mv^2 - \frac{GMm}{r}\right)_{initial} = \left(\frac{1}{2}mv^2 - \frac{GMm}{r}\right)_{final} \quad (1.2)$$

One of the most elementary applications of Equation (1.2) is to calculate the velocity required to completely overcome the gravitational potential energy, the aptly named “escape velocity”,  $v_e$ .

When calculating the escape velocity, it is important to note that the final velocity is zero (indicating an escape) as is the gravitational potential energy since the gravitational field is assumed to be zero at  $r$  equal infinity. Equation (1.3) is an expression for the escape velocity.

$$v_e = \sqrt{\frac{2GM}{r}} \quad (1.3)$$

Plugging in the typical numbers for Earth, a velocity of 11.2 km/sec from the surface is required to completely escape the Earth’s gravitation field.

. Once in a high enough orbit though, the effects of atmospheric drag are drastically reduced allowing one to coast for an extended amount of time without significant loss in velocity and therefore orbit altitude. If we assume that we’re are in a circular orbit, the specific mechanical energy of the orbit,  $\epsilon$ , is

$$\epsilon = \frac{v^2}{2} - \frac{\mu}{r} = \frac{-\mu}{2a} \quad (1.4)$$

where,  $\mathbf{v}$  and  $\mathbf{r}$  are the orbital and velocity position vectors relative to the central body and  $a$  is the semi-major axis length. This equation is also known as the energy equation as it relates the gravitational potential energy to the kinetic energy of the orbiting body. For a circular orbit

though, the semi-major axis length is equal to the radius of the Earth so the velocity of a given orbit radius  $r$  can be expressed by

$$v = \sqrt{\frac{\mu}{r}} . \quad (1.5)$$

This velocity-altitude relationship is very useful in ascertaining how much total energy is required to change from one circular orbit to a different circular orbit.

## ***1.2 Orbital Maneuvers***

Typically, a launch vehicle will inject a spacecraft into a 180-300 km low earth orbit called a parking orbit which is usually not the final destination. A craft may remain in a parking orbit for varying lengths of time depending on if there are any maneuvering window requirements – for example waiting for right time to start moving to a rendezvous point. Additional thrust must be provided to change the orbit velocity and therefore orbit altitude to place the spacecraft in the appropriate place. For instance, most communication satellites must be raised to geosynchronous orbit whereas weather satellites will probably require an inclination change. In addition to changing orbits, it is also often necessary to correct for orbit perturbations and atmospheric drag. However, this section will focus only on simple orbit raising maneuvers.

The most rudimentary orbit transfer consists of raising or lowering of a co-planar circular orbit. This is the typical transfer for a geosynchronous satellite but is also used to raise and lower satellites in lower orbits. There are a variety of ways to accomplish this and the decision which to use is a function of many constraints. The most popular and fuel-efficient way to do a planar orbit transfer is using a Hohmann Transfer. In a Hohmann Transfer, the propulsion system is fired twice: the first burn places the spacecraft into an elliptical transfer orbit and the second burn

returns the craft to a circular orbit. The elliptical transfer orbit is tangential to both the initial and final orbit. Although the Hohmann orbit transfer is quick, requiring only a half orbit to complete, the *one-tangent burn* can achieve a transfer faster by sacrificing propellant for time. In this case the initial burn is tangent to the initial orbit but the elliptical transfer orbit is not tangential to the final orbit and thus requires the second burn to occur at given angle which is dependent on the semi-major axis of the transfer orbit. However, in both the Hohmann Transfer and the one-tangent burn transfer, the burns must be impulsive. That is, the change in velocity must occur over a time period that is very short compared to the orbital period. For reasons detailed shortly the requirement of impulsive burn will limit the propulsion devices capable of making such transfers.

The final common co-planar circular orbit transfer is the *spiral transfer*. In this transfer, a low level of thrust is continually applied and over a period of many orbits, the spacecraft eventually obtains the velocity of the final orbit. This sort of orbit transfer will be examined as for reasons to be explained later, it is the only transfer that is reasonably possible with electric propulsion devices.

In a spiral orbit transfer, the craft will orbit the Earth many times so the orbit can be approximated to be a constantly increasing circular orbit. Returning to the equation relating orbital velocities and altitude, it is a trivial matter to calculate the required change in velocity for the orbit transfer. For example, a 300 km low earth orbit to a 42,200 km geosynchronous orbit would require

$$\Delta v = |v_{geo} - v_{park}| = \sqrt{\frac{\mu}{44,164}} - \sqrt{\frac{\mu}{6678}} = 4.65 \text{ km / sec} \quad (1.6)$$

Note that the radius of the Earth is included in both orbits. For comparison, a similar Hohmann transfer would require a  $\Delta v$  of 3.9 km/sec and a one tangent burn would require 4.7 km/sec.

### ***1.3 Introduction to Rocket Propulsion***

When broken down to the simplest terms, rockets and other space propulsion systems rely on Newton's Second and Third Laws of motion: the force generated is the mass times acceleration (the familiar  $F=ma$ ), and for every action, there is an equal and opposite reaction[1]. Likely the most familiar and applicable example of this reaction is a typical rocket launch. When the engines roar to life, Equation (1.7) governs the propulsive situation with  $T$  being the thrust developed,  $v$  being the exhaust velocity of the particular propellant and  $dm/dt$  being the time rate of mass change of the rocket. Simply put, this equation states that the rocket is generating thrust by accelerating and expelling its own mass in accordance with Newton's Third Law.

$$T = v \frac{dm}{dt} \tag{1.7}$$

Engine performance alone is not sufficient to guarantee that the craft achieves sufficient velocity to remain in orbit rather than crash back down to earth and also says nothing about how much of the original craft was not exhausted and is therefore useable when the destination is reached. To analyze the feasibility of mission requirements, the ideal rocket equation, also known as Tsiolkovsky's rocket equation is used. The rocket equation is given in Equation (1.8) where  $\Delta v$  is the change in velocity required to reach the destination,  $v_e$  is the velocity of the exhausted mass,  $m_i$  is the initial mass and  $m_f$  is the final mass.

$$\frac{m_i}{m_f} = e^{\frac{\Delta v}{v_e}} \quad (1.8)$$

In propulsion, it is often useful to examine the impulse received by expelling a given amount of weight (not mass). This gives rise to the concept of specific impulse,  $I_{sp}$ , which is defined as:

$$I_{sp} = \int F \frac{dt}{g_0 dm} = \frac{\bar{v}_e}{g_0} \quad (1.9)$$

where  $g_0$  is the gravitational acceleration on Earth at sea level,  $9.8 \text{ m/s}^2$ , so the units of specific impulse are in seconds. The other advantage of using specific impulse instead of exhaust velocity is that it can more accurately describe the exhaust situation. That is, it is very unlikely that all of the exhausted propellant is moving at the same velocity so it is more useful to look at the impulse gained from the expelled propellant then use that figure to determine an average exhaust velocity. Using Equation (1.9) the rocket equation can now be written as:

$$\frac{m_i}{m_f} = e^{\frac{\Delta v}{g I_{sp}}} \quad (1.10)$$

As an example, assume that a spacecraft is performing a LEO to GEO Hohmann Transfer which requires a  $\Delta v$  of 3.9 km/sec. The propulsion system used for the transfer is a conventional bi-propellant chemical thruster with a 325 second specific impulse. Using Equation (1.10), 71% of the spacecraft's mass would have to be propellant to complete the transfer.

The most obvious way to improve this seemingly unreasonable propellant burden is to increase the exhaust velocity and therefore specific impulse of the rocket engine. However, there

is a fundamental limit for any rocket engine that requires the breaking of chemical bonds to provide energy: there simply is only so much energy available in the bonds. Ideally all of the stored energy would go towards increasing the kinetic energy of propellant so it could pass through a nozzle and produce thrust. But as any chemistry or thermodynamics text book says – much of that energy will be soaked up by rotational and vibrational states of the propellant. To reduce the effects of this, propellants with simple combustion products are used but even then a practical limit is quickly reached. This effectively limits the practical specific impulse one could expect to about 450 seconds.

### ***1.4 Introduction to Electric Propulsion***

The only way to achieve a higher specific impulse is to not rely on chemical means but rather by accelerating the propellant directly ensuring only kinetic energy is imparted to the reaction mass. Enter electric propulsion. In electric propulsion, electromagnetic body forces are used to direct and accelerate matter rather than combustion. There are three distinct classes of propulsive devices: electrothermal, electromagnetic, and electrostatic. Each class will be briefly covered but a much more thorough explanation of each is available in Refs [2-5].

Electrothermal devices are the simplest and most flown electric propulsion class. These devices rely on imparting thermal energy to the propellant via resistive heating elements or an electrical discharge then exhausting the super-heated propellant through a nozzle. Typical electrothermal propellants are hydrazine, ammonia and hydrogen. There are two main electrothermal devices: resistojets and arcjets. Both devices are similar in that a propellant is heated to temperatures in excess of 3,000 K and the expanded gas is directed through a nozzle producing thrust. In a resistojet, the propellant is passed through a resistively heated manifold or series of tubes where the propellant gains thermal energy. In an arcjet, the thermal energy is

imparted to the propellant via an arc discharge between an anode and a cathode. There are many modifications and enhancements that have been added to improve the efficiency of electrothermal thrusters which have created a reliable propulsion platform. However, material constraints limit the amount of thermal energy which may be imparted to the propellant though these issues may be avoided if the propellant is directly accelerated as is the case with electrostatic and electromagnetic devices.

Electrostatic electric propulsion devices rely on an electric potential gradient to accelerate ions. Take the case of a single atom floating in free space. If an electron can be stripped from the atom, the newly formed ion can be accelerated by an applied electric field. In fact, relativity aside, the only theoretical limit on the final velocity of the ion is whatever the limit is on the electric potential gradient. The most familiar type of electrostatic thruster would have to be the gridded ion engine. In a gridded ion engine, propellant is injected and ionized in a magnetically confined discharge chamber. The ions then diffuse through a positively biased grid. On the other side of the positively biased grid, there is a second, negatively biased grid and the potential gradient between them accelerates the ions.

Electromagnetic electric propulsion devices rely on both electric and magnetic fields to accelerate ions. A more detailed explanation of a specific electromagnetic device, the Hall-effect thruster, is contained in the next section.

The current state-of-the-art chemical and electric propulsion systems are listed in Table 1 along with the average specific impulse.

<b>Table 1: Summary of in-space chemical and electric propulsion devices[6]</b>				
	<b>Isp (typ)</b>	<b>Efficiency</b>	<b>Thrust</b>	<b>Propellant</b>
Solid Rocket	242 sec	N/A	>>1000N	APCP
Chemical bi-propellant	328 sec	N / A	400N	N <sub>2</sub> H <sub>4</sub> /N <sub>2</sub> O <sub>4</sub>
Arcjet	600 sec	32%	0.270N	N <sub>2</sub> H <sub>4</sub>
Hall Thruster	1600 sec	50%	0.085N	Xenon
Ion Engine	2800 sec	65%	0.100N	Xenon

### ***1.5 Hall-Effect Thruster Overview***

The physics of Hall-effect thruster operation is a complicated subject which has been extensively documented in many sources[2, 3, 5, 6]. A summary is provided here. Figure 1 is a schematic of a typical Hall-effect thruster. An external thermionic emitting cathode provides electrons which are attracted to the positively biased (300 Volts nominal) anode. The anode is contained within an annular shaped insulating ceramic typically made of boron-nitride. The anode also serves as a neutral gas distributor. A radial magnetic field is generated by external electromagnets and is carried around the boron-nitride / anode via high permeability iron. The magnetic field then traverses the gap above the anode, ideally creating a uniform magnetic field in that region on the order of 100's of Gauss. The circuit is completed by a center magnetic pole that optionally has an additional electromagnet. The magnetic circuit is used to intercept and trap electrons that were emitted by the cathode. These trapped electrons move perpendicular to both the applied electric and magnetic field giving rise to an azimuthal drift called the Hall current.

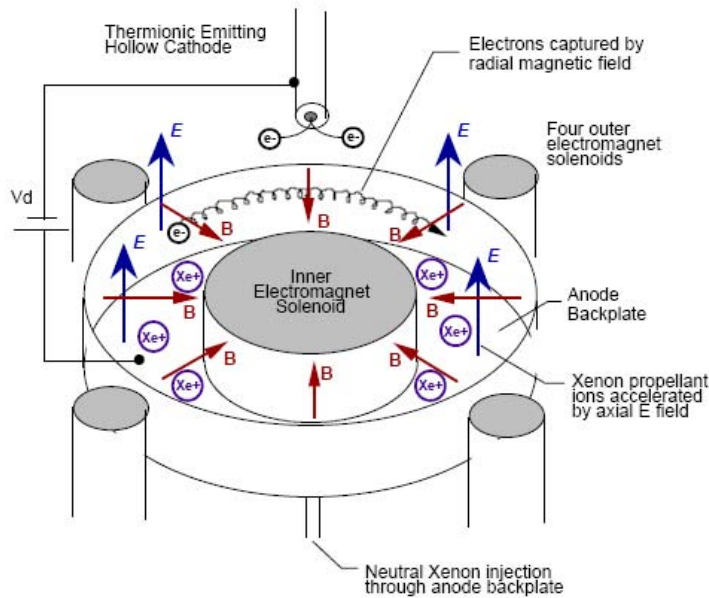


**Figure 1: Schematic of a Hall-effect thruster as shown in Ref [7]. Reprinted with permission.**

**Permission letter can be found in Appendix D.**

Neutral gas, usually xenon or krypton is injected through a combination gas distributor and anode. The neutral gas atoms will experience no net force from the applied electric and magnetic fields and will simply diffuse away from the anode. Eventually the neutral atoms will encounter the swarm of electrons trapped in the Hall current. Impact ionization will remove an electron from each neutral atom creating an ion and an additional free electron. The newly “born” ion will suddenly experience the repulsive potential of the local electric field and be accelerated away, thus generating thrust. The ions are far too heavy to become trapped on the relatively weak magnetic field lines. To prevent charging of the thruster, the cathode not only provides electrons for ionization, but also electrons for neutralization of the accelerated ion beam.

## ***1.6 Current State of the Art Hall Thrusters and Associated Limits***

Fifty years of research on gas-fed xenon and krypton Hall thrusters has created a well established and mature technology. The first Hall thruster in space was on the Soviets' *Meteor* spacecraft which was commenced operation during February of 1972[8]. Although the Soviets have since integrated and launched over 100 satellites with Hall thrusters, the first US use of a Hall-effect thruster did not occur until December 16<sup>th</sup> 2006 when the Air Force Research Laboratory's TacSat-2 with a Busek BHT-200, 200 Watt xenon Hall thruster. This lower power thruster has a 1390-second specific impulse and generates 12.8mN at 43.5% efficiency[9].

Smaller Hall thrusters (sub-20 kW), are typically tasked with several different missions. Orbit raising and lowering can be done with a Hall-effect propulsion system but the low thrust nature of the EP devices make such transfers take an extended amount of time. To reduce the amount of time for the transfer, a mix of chemical and EP can strike a favorable balance between trip time and delivered payload. Hall thrusters are also used for what is known as station keeping. In this application, the thruster is used to compensate for atmospheric drag and other orbit perturbations. Higher power Hall-effect thrusters have an evolving niche for extended duration missions requiring large  $\Delta v$ 's. The NASA 457M is a 50 kW thruster platform aimed at providing propulsion for interplanetary robotic missions.

While gas fed xenon Hall thrusters represent a mature technology they require the use of expensive cryogenic pumps with recurring liquid nitrogen costs. High power xenon Hall thruster development certainly continues, but there are very few facilities with the necessary pumping infrastructure required to keep the facility testing pressure below the accepted limit of  $5 \times 10^{-5}$  Torr. Depending on mass flow rate, a 50 kW thruster would require approximately 2,000,000 l/sec of pumping speed on air. Cryopump speed costs approximately \$1 per-l/s translating to an

initial cost of \$2,000,000 just to enable the thruster to be turned on. This price does not include the cost of the large vacuum facility required fit all of the cryopumps inside. Currently NASA Glenn's Tank 5 is one of the fastest xenon pumping vacuum system in the world with a 3,500,000 l/sec of pumping capacity[10, 11].

### ***1.7 Contribution of Research and Document Roadmap***

Simply put, the primary aim of this research was to develop a bismuth fed Hall thruster. While not a new concept, previous bismuth thrusters required extensive amounts of auxiliary heating to provide bismuth vapor. As the research effort evolved, it was clear that there were several problems which needed to be addressed. To that end, the following research aims needed to be satisfied:

- Development of a mass flow system which did not rely on gas phase bismuth delivery
- Minimize the amount of auxiliary heat required for continuous operation
- Ensure thermal stability of all parts
- Retain the ability to control and measure the bismuth supply rate
- Establish that when operating on bismuth, the thruster was indeed acting as a plasma accelerator

To meet those aims, this dissertation will detail the development process of the Direct Evaporation Bismuth Thruster. As this research has many varied facets, the following roadmap will help understand the organization. In Chapter 2 the reader will find background information on bismuth including some mission analysis which will serve as an additional motivation for considering bismuth as a propellant. Also in Chapter 2 the previous bismuth efforts and limitations will be examined. In Chapter 3, the Direct Evaporation concept is introduced to

address the issues that arose in the previous chapter. The evaporation kinetics of bismuth will be examined and in conjunction with some interfacial engineering concepts will provide the foundation of the development of the porous vaporizer which is the centerpiece of this particular thruster. Chapter 4 is an exhaustive narrative on the actual experimental development which served to direct the direction of the research. The chapter begins with some thermal modeling which is later validated by testing with xenon. As the thruster matured, operation makes the transition from xenon to bismuth. Along the way though, materials limitations and interactions force the eventual conclusion that stainless steel is not thermally stable enough to be used as a vaporizer material. To address the stainless steel limitations Chapter 5 takes a substantial departure through the field of refractory powder metallurgy. To enhance thermal stability of the vaporizer a process for fabricating and bonding porous molybdenum is developed. Since a bismuth thruster does not operate similar to a xenon thruster, Chapter 6 is dedicated to some of the operational differences. While not all the operational mechanisms are understood, several are examined including ignition transients and slow-scale discharge oscillations. Chapter 7 contains the conclusions of this dissertation. Appendix A contains the phase diagrams for bismuth and several commonly used metals and is included only for reference. Appendix B is a step by step explanation of how the porous vaporizer is fabricated and bonding. Appendix C is essentially the operating manual for the thruster covering aspects ranging to heating system rebuilds to operational methodology. Appendix D is the copyright authorization which is included to keep the lawyers happy.

## 2. Introduction to Bismuth

This chapter will begin by taking a brief look at some of the physical, electrical and practical aspects of bismuth. In Section 2.2, the advantages of using bismuth as a propellant are examined in some amount of detail. Section 2.3 contains the liabilities that come with using bismuth as a propellant. Since using bismuth as a Hall thruster propellant is not without precedent, other bismuth Hall thrusters will be examined in Section 2.4

### *2.1 Physical Attributes of Bismuth*

Bismuth, Bi, is the heaviest non-radioactive element. It is a non-malleable, non-toxic metal whose early uses can be traced back to the 1450's though it was not until 1753 that it was discovered that bismuth is actually different than lead. With an atomic number of 83 it falls next to lead in the metals range of the periodic table. It has a melting point of 271.4°C and a boiling point of 1564°C. In appearance, it is shiny silver with clearly defined crystals in fractured areas. Figure 2 is a photo of bismuth as received from a vendor and Table 2 lists some detailed physical properties of bismuth.

Chemical Symbol	Bi
Atomic Number	83
Atomic Mass	208.9804 AMU
Melting Point	271.40°C
Boiling Point	1564°C
Density: 298 K (solid)	9747 kg/m <sup>3</sup>

544 K (liquid)	10500 kg/m <sup>3</sup>
Ionization Energy: 1st 2nd 3rd	7.2855 eV 16.703 eV 25.5 eV
Heat of Fusion	11.30 kJ/mol
Heat of Vaporization	151 kJ/mol
Heat Capacity (300 K)	25.52 J/mol K
Lattice Structure	Hexagonal close-pack (HCP)
Thermal Conductivity (298K)	7.87 W/m K
Electrical Conductivity	9.36x10 <sup>5</sup> /Ω m
Abundance	0.048 ppm
Electronic Configuration	[Xe]4f <sup>14</sup> 5d <sup>10</sup> 6s <sup>2</sup> 6p <sup>3</sup>
Valence States	+5, +3
Pauling Electronegativity	2.02
Atomic Radius	150 pm
Isotopes	<sup>209</sup> Bi, 100%, stable
Thermal Neutron Cross-section	54.(4) barns



**Figure 2: Solid bismuth**

Common uses and practical properties of bismuth are outlined from the following excerpt from the 2006 USGS Minerals Yearbook (Ref [13]):

*“The USGS surveys domestic bismuth consumption annually. The amount used by non-respondents is estimated based on reports from prior years or on information from other sources. Accordingly, estimated bismuth consumption was about 2,050 t in 2006, a 13% decline from that of 2005.*

*Consumption of bismuth in chemical uses (chemicals, cosmetics, and pharmaceuticals) in 2006 increased by 2% compared with use in 2005. The leading use, metallurgical additives, experienced a 20% decrease in consumption in 2006 compared with that in 2005. The alloys category of use registered a 14% decline in tonnage compared with that of 2005.*

*Although it has the crystal structure of a semimetal, bismuth is often considered a metal. This crystal structure, along with several other salient properties, makes it an ideal*

*substitute for lead in extreme-pressure additives. These unique properties include expansion on solidification, the widest range between melting and boiling points among all metals, and the lowest thermal and heat conductivity. Bismuth is the most diamagnetic of all metals, the least toxic, and has the lowest absorption for neutrons; bismuth is also characterized as “soft” like lead.*

*Bismuth pharmaceuticals include the well-known bismuth salicylate (the active ingredient in the over-the-counter stomach remedies) and other bismuth medicinal compounds used to treat burns, intestinal disorders, and stomach ulcers in humans and animals. Bismuth nitrate is the initial material used for the production of most bismuth compounds. Other applications of bismuth chemicals and compounds include uses in superconductors and pearlescent pigments for cosmetics and paints.*

*Bismuth metal is used primarily as a major constituent of various alloys and as a metallurgical additive. One class of bismuth alloys consists of fusible (low-melting-point, as low as 20° C) alloys—combinations of bismuth with other metals, such as antimony, cadmium, gallium, indium, lead, and tin. Applications for those alloys include fuel tank safety plugs, holders for optical lens grinding, and other articles for machining or grinding, solders, and fire sprinkler triggering mechanisms.*

*In addition to lead-free solder noted above, bismuth has been a substitute for the lead added to certain steel products to provide greater machinability. A major domestic steel producer began to use a bismuth-containing substitute for the leaded alloy about 1982. Although bismuth has been successfully used in replacing lead in various applications, it has been challenged as a lead substitute by tin and tungsten. Bismuth is also added in small amounts to aluminum (along with lead) and copper alloys to improve*

*machinability. It is also added to malleable iron graphite flakes. These uses constitute the traditional metallurgical additives category.”*

Aside from the more pedestrian uses listed above, bismuth also found a niche in the nuclear industry. Since the 1950's the Soviet Union as well as the United States were developing nuclear power plants using metallic coolants in the primary cooling loops. US efforts were directed more towards sodium and other salts but the Soviets chose to use a 44%/56% lead-bismuth alloy. From 1974 to 1983, the Soviet navy constructed seven lead-bismuth cooled nuclear powered submarines (Alfa class)[14]. The lead-bismuth alloy provided several intrinsic advantages over sodium. The most important advantage from a nuclear power plant / core design standpoint is that there is no explosion hazard should any lead-bismuth coolant come in contact with water. Designing a reactor containment vessel and supporting hardware to ensure sodium isolation is very costly. A lead bismuth-alloy also has better neutron reflection properties which enhance efficiency and economy of the reactor. The lower vapor pressure at elevated temperatures of a lead-bismuth alloy potentially allows for higher coolant temperatures creating higher thermodynamic efficiencies. Safety is also enhanced as in the event of reactor coolant failure, it would be essentially impossible to boil away or even over pressurize the primary stage lead-bismuth coolant which is certainly not the case for a pressurized water cooling system or even for a sodium system[15]. If preventative measures are not taken, the hot lead-bismuth alloy can destroy most metals via a mass dissolution attack but it is certainly not as corrosive as sodium. Appropriate use of refractory metals and reasonable temperatures minimize potential material incompatibilities[16-21]. Although there are no production reactors with a lead-bismuth coolant loop currently in operation, there have been no insurmountable engineering barriers that would preclude its use again in the future [22].

A lead-bismuth alloy may also find use in the recycling of spent nuclear fuel via a process known as “actinide burning”. Actinide burning is the process by which the heavy, radioactive elements in the actinide row of the periodic table are deliberately processed in a nuclear reactor core yielding fissile products with reduced radioactivity[23]. This process creates electricity as well, though not as economically as a simple nuclear reactor. A lead-bismuth alloy is favorable for this due to the ability to introduce additional fertile and non-fertile fissile material during reactor operation[24]. Although there are currently no reactors in operation for actinide burning, development is underway[25].

## ***2.2 Advantages of Bismuth as a Propellant***

While xenon and krypton have adequately served the needs of ion propulsion devices since inception, there is always room for improvement. Before looking into the energy advantages of bismuth, the economic advantages of using bismuth are also of significant interest. For instance, bismuth retails for about \$11/kg[13] as opposed to current market price of \$7,700/kg for xenon which translates to a huge savings in propellant cost. A 50 kW thruster would run at an estimated 150 mg /sec of propellant so for a single continuous day of testing, 12.96 kg of propellant would be required. This translates to negligible \$143-per-day to operate a 50-kW bismuth thruster compared with \$99,792-per-day for an equivalent xenon device (without xenon reclamation). A 10,000 hour wear test would cost \$41.5 million for xenon but only \$59,400 for bismuth.

Perhaps more importantly though, as mentioned before, the development of larger xenon thrusters has been hampered by the enormous ground testing costs involved in purchasing, integrating and operating huge cryogenic pumps. It is in ground testing that bismuth offers a critical advantage over xenon: it is a solid at room temperature. This means that any exhausted

bismuth will hit the tank wall and solidify, turning the entire vacuum chamber into an effective pumping surface. With that in mind, operating a bismuth Hall thruster would require only enough pumping speed to keep up with the cathode mass flow (assuming a xenon cathode). Since flight thrusters are operated in a similar fashion as they were ground tested, the off time required to regenerate the xenon cryopumps has implication on flight missions. A bismuth thruster could run continuously with no need to ever suspend high vacuum conditions.

Economics aside, there are several kinetic advantages that bismuth holds over xenon and krypton. On the most basic level, the overall efficiency of a Hall thruster is the ratio of the kinetic energy imparted and the total input power.

$$\eta_T = \left( \frac{P_{kinetic}}{P_{total}} \right) \quad (1.11)$$

However, it is worthwhile to examine some of the loss mechanisms that limit the kinetic power.

Overall thruster efficiency is given by the product

$$\eta_T = \eta_c \eta_m \eta_a \quad (1.12)$$

where  $\eta_c$  is the neutralizing cathode efficiency,  $\eta_m$  is the electromagnetic circuit efficiency and  $\eta_a$  is the anode efficiency. *Since the research goal of this document was not to ascertain overall thruster performance, all performance numbers reported will be anode efficiencies unless otherwise noted.* Anode efficiency can be further broken down to

$$\eta_a = \frac{T^2}{2\dot{m}P} = \eta_b \eta_p \eta_q \eta_v \quad (1.13)$$

where  $T$  is the measured thrust,  $\dot{m}$  is the anode mass flow rate,  $P$  is the anode discharge power[26-30]. In the efficiency product,  $\eta_b$  is current utilization efficiency relating the amount of ion current in the beam to the discharge current measured by the power system,  $\eta_p$  is the propellant utilization efficiency which is a measure of how much of the injected neutral propellant is being ionized,  $\eta_q$  is charge utilization efficiency which accounts for the loss from multiply charged ions and  $\eta_v$  is the voltage utilization efficiency which indicates how much of the discharge voltage is actually being used to accelerate the ions in the axial direction and accounts for beam divergence losses as well as ionization costs. Given this breakdown of efficiency it is possible to estimate the performance increases one might expect by switching from xenon to bismuth.

To examine some of the efficiency changes, it is useful to first take a look at the energy required to create the ions. The first ionization energy of bismuth is 7.3 eV compared to xenon's 12.1 eV and krypton's 14.0 eV. Since the gas must be ionized to generate thrust, it is reasonable to examine the power requirements of ionization. If the reasonable simplifying assumption[29] that every ion that is created is only singly ionized then the power required to ionize the entire propellant flow is

$$P_{ion} = \dot{m}E_{ion} \quad (1.14)$$

where  $E_{ion}$  is the ionization energy of a given propellant expressed in units of J/kg rather than the more traditional eV/atom and  $\dot{m}$  is the mass flow rate. The kinetic power of the accelerated beam can be written as:

$$P_{kin} = \frac{1}{2}\dot{m}v_e^2 = \frac{\dot{m}g^2 I_{sp}^2}{2} \quad (1.15)$$

If we take the ratio of the ionization cost to the kinetic energy derived from ion acceleration, the resulting equation can be used to calculate maximum theoretical voltage efficiency given in Equation (2.6). It is called the maximum theoretical voltage efficiency because it assumes that the required ionization energy is the only thing preventing the ion from being accelerated by the entire magnitude of the applied electric potential (discharge voltage). Figure 3 is a plot of the maximum theoretical voltage efficiency for xenon, krypton and bismuth as a function of specific impulse.

$$\eta_{\max} = \frac{P_{kin}}{P_{kin} + P_{ion}} = \frac{g^2 I_{sp}^2}{g^2 I_{sp}^2 + 2E_{ion}} = \frac{1}{1 + \frac{2E_{ion}}{g^2 I_{sp}^2}} \quad (1.16)$$

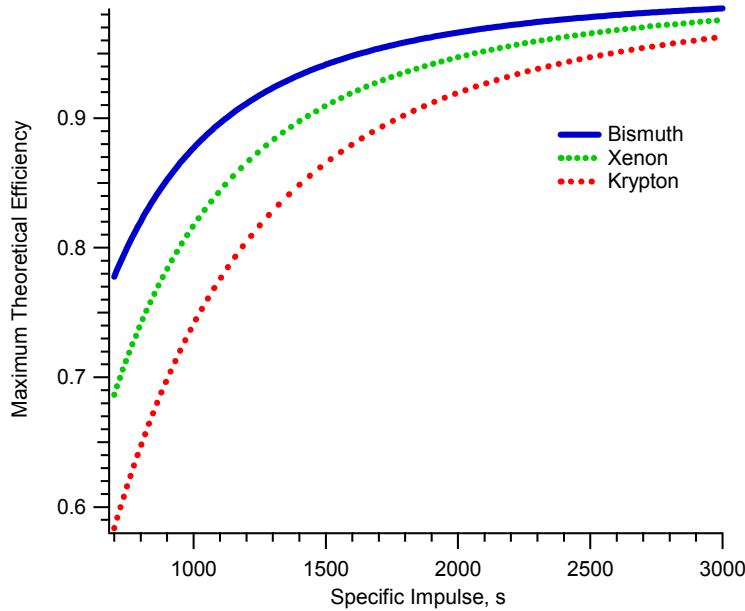


**Figure 3: Maximum theoretical voltage efficiency as a function of specific impulse**

At higher specific impulses, the percent of power required for ionization becomes an almost negligible fraction of the total power deposited into the high-velocity beam and the choice

of propellant species is not critical. However, as the specific impulse is reduced, substantial differences arise. At 800 seconds specific impulse the percent of thruster power required for the ionization of bismuth, xenon and krypton limits the maximum theoretical efficiency to 82%, 74% and 65%. As the data suggests, using krypton at low specific impulse would be very inefficient and xenon performance will critically suffer as well.

Examining ionization power fractions alone does not give the entire picture of the lower specific impulse advantages of bismuth. As the discharge voltage is decreased, the electrons, which are critical in the ionization process, suffer a reduction in available impact-ionization energy. Figure 4 is a plot of the first, second and third ionization cross-sections for bismuth which are readily available in literature[31]. In a nominally functioning xenon thruster with a 300-Volt anode potential, the electrons are expected to have a Maxwellian temperature distribution centered around 20 eV[32] which almost linearly decreases with discharge voltage. Figure 5 is a plot comparing the first electron-impact ionization cross-section of bismuth and xenon.

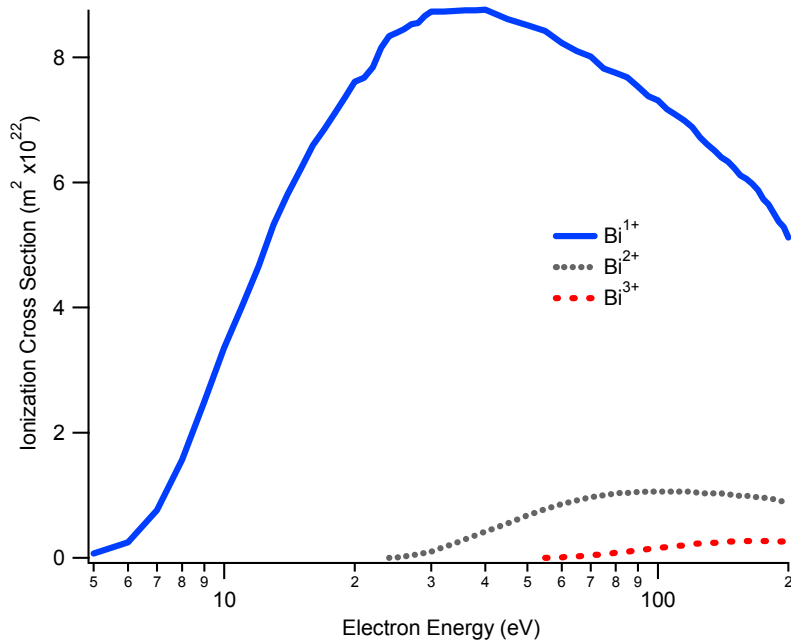


Figure 4: Electron impact ionization cross sections for Bi<sup>1+</sup>, Bi<sup>2+</sup> and Bi<sup>3+</sup>

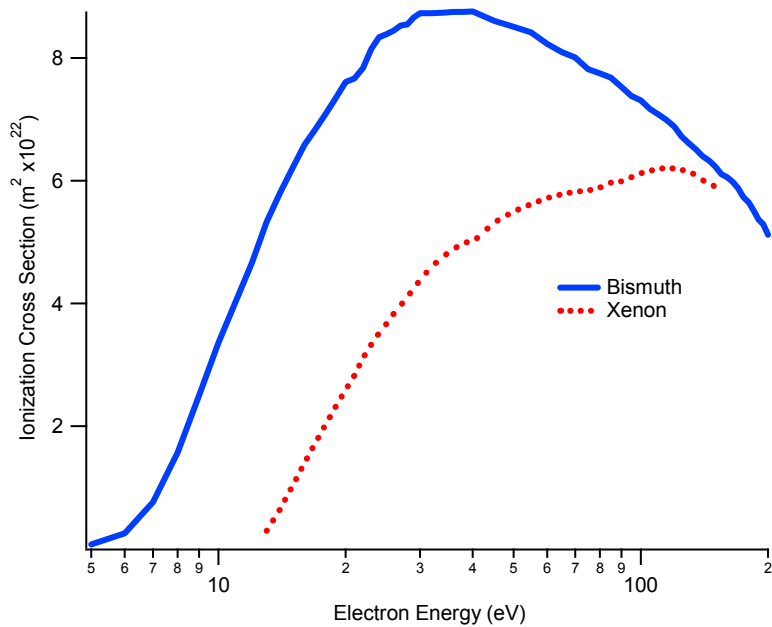


Figure 5: First electron-impact ionization cross-sections of bismuth and xenon

From this graph one can conclude that for the same discharge voltage, bismuth will have a significantly greater electron-impact ionization cross-section than xenon. This has important implications especially in the lower operating voltages. In Hall thrusters, lower specific impulse is obtained by decreasing the anode discharge voltage and is proportional to the following expression

$$I_{sp} \propto \frac{\sqrt{\frac{2qV_{dis}}{m}}}{g} \quad (1.17)$$

At nominal (meaning greater than about 250 V) discharge voltages, xenon Hall thrusters are reported to have a propellant utilization efficiency of 90% or greater[7, 26]. This means that 90% of the neutral flux injected into the discharge chamber is converted into an ion flux. However, at 150 volts, it was reported that xenon propellant utilization was estimated to be 81% while at 100 volts propellant utilization had dropped to 61%[33]. The cause in the decreased propellant utilization is a direct effect of the less-energetic electrons interacting with a diminishing xenon electron-impact ionization cross-section. Without comprehensive bismuth performance data, it is difficult to say exactly what low-voltage mass utilization efficiency would be for bismuth but there is likely that it would be significantly higher compared to xenon.

Obviously thruster efficiency is important or there would be little reason to work so hard to try and increase it. Why the efficiency is important has to do with the mass cost of dragging along a power supply. With that in mind, the power supply requirements,  $P_s$ , are given by Equation (2.8) which serves as the first practical implication of thruster efficiency on spacecraft integration. It states that for a given kinetic power output, thruster efficiency will dictate how much total supply power is required.

$$P_s = \frac{\frac{1}{2} \dot{m} v_e^2}{\eta_T} \quad (1.18)$$

If it were possible to generate unlimited power on a spacecraft without a mass penalty, thruster performance would have little impact on design constraints. Of course that is not possible as every Watt generated carries with it an inherent mass liability. When the spacecraft arrives at its final destination, it carries with it not only the payload and remaining propellant, but also the power supply system. Certainly there will be other power hungry devices on the spacecraft but more than likely the power electronics for the propulsion system will not be exceptionally useful for the payload. This gives rise to the concept of the inert mass – mass that must accompany the spacecraft to the destination but has no use once there. The mass of the power system tends to scale linearly with power output and can therefore be expressed by

$$m_{inert} = \beta P_s \quad (1.19)$$

where  $\beta$  is the specific mass of the propulsion system in kg/kW. Although  $\beta$  is very dependent on applied technology and application, it typically ranges from 2-20 kg/kW[2, 3, 6]. With the dependency of power system inert mass on supplied power established, Equations (1.8) (2.8) and (2.9) can be combined to yield

$$\frac{m_{payload}}{m_{initial}} = e^{\frac{-\Delta v}{g I_{SP}}} - \left( 1 - e^{\frac{-\Delta v}{g I_{SP}}} \right) \frac{\beta (g I_{SP})^2}{2 \eta_T \tau} \quad (1.20)$$

where  $\tau$  is the burn time of the thruster[3]. Although it may not be immediately evident from looking at Equation (2.10), there is an optimum specific impulse which balances the specific impulse induced power system mass penalty and the trip time. The inert mass of the power plant

will reduce the delivered payload if the transfer is performed with too high or too low of a specific impulse. Equation (2.11) is an expression for the optimum specific impulse which is dependent only on efficiency, power system specific mass and desired trip time[5].

$$I_{sp(optimal)} = \frac{1}{g_0} \sqrt{2\eta\tau\beta} \quad (1.21)$$

The need to raise or lower the specific impulse for a given propulsion system (where efficiency and power system specific mass are specified) then is governed solely by the trip time. Figure 6 is a graph showing the optimum specific impulse as a function of trip time and efficiency assuming a propulsion system specific mass of 10 kg/kW.

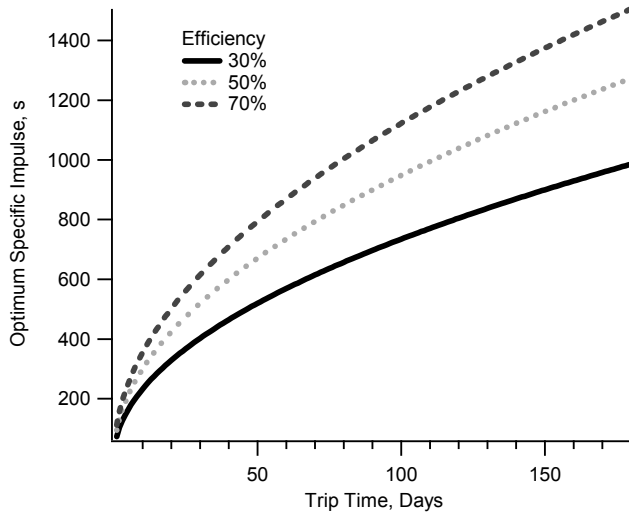


**Figure 6: Optimum specific impulse for 30%, 50% and 70% efficiencies and a specific mass of 10 kg/kW.**

Using Figure 6 as a guide, if the desire is to perform an orbital maneuver quickly, a lower specific impulse will provide more optimum results. As always, there is a caveat to this: most propulsion devices do not perform well, if at all, outside of a narrow window of specific impulse.

As mentioned above, any given maneuver will have an optimal specific impulse. When the spacecraft mass and desired trip time are taken into consideration, the average required thrust can be easily calculated keeping in mind that amount of available power on the space craft is fixed. With these numbers, one can obtain the required thrust-to-power ratio which is denoted in Equation (2.12).

$$\frac{T}{P} = \frac{2\eta}{gI_{sp}} \quad (1.22)$$

The implication of the thrust-to-power ratio means that to shorten the trip time, a higher thrust-to-power ratio propulsion device must be used but at the expense of propellant. However, as illustrated in Figure 7 electric propulsion devices can have a range of thrust-to-power ratios which is determined by the operational characteristics of the device. This allows for some amount of flexibility in which propulsion platform is most appropriate for the mission. For example, if most of the prescribed orbital maneuvers are time sensitive (short trip time) then it would not make much sense to use an ion engine when an arcjet would be more appropriate. Placed in the context of this dissertation, here is a significant gap between the arcjets and the xenon Hall thrusters which a bismuth Hall thruster would fill.

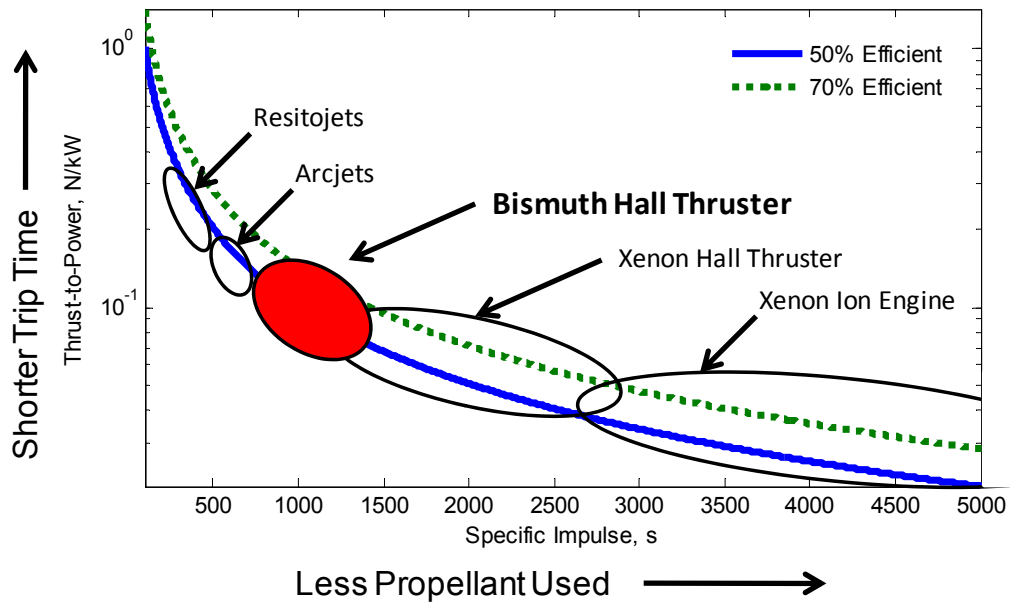


**Figure 7: Thrust-to-power ratio as a function of specific impulse illustrating the niche for bismuth.**

The question arises then, why can a xenon Hall thruster not perform at lower specific impulses? Why must a different propellant be used? As previously mentioned in Section 1.4, in Hall thrusters, specific impulse is governed by the accelerating (discharge) voltage and the mass of the propellant being accelerated. While in theory this is true, in practice the situation is much different. Table 3 lists some of the performance characteristics of the NASA-457 Hall thruster over a range of discharge voltages[33, 34] as well as what the equivalent  $I_{sp}$  would be if the thruster were to run on bismuth (which it certainly has not). The equivalent bismuth  $I_{sp}$  is what the specific impulse would be if all other parameters remain unchanged but the mass of the propellant. The bismuth  $I_{sp}$  is related to xenon specific impulse by:

$$I_{sp(Bi)} = \sqrt{\frac{131}{209}} I_{sp(Xe)} . \quad (1.23)$$

Discharge Voltage (V)	Xenon mass flow (mg/sec)	Discharge Power (W)	Anode efficiency	$I_{sp}$ (s)	Equivalent Bismuth $I_{sp}$ (s)
100	35.2	2008	0.32	581	460
130	35.2	3731	0.44	770	610
150	35.2	6036	0.49	1176	931
300	35.2	10,287	0.53	1790	1417
400	84.6	39,697	0.6	2031	1896
500	84.6	50,120	0.62	2314	2160
600	92.7	64,915	0.64	3055	2419

These data indicate that though it is possible to reduce specific impulse by decreasing the discharge voltage, much below 150 Volts there is a severe performance penalty. Instead of lowering discharge voltage to decrease specific impulse, the mass of the propellant could be increased by using bismuth instead of xenon.

The effects of changing propellant mass on the delivered payload can be clearly quantified by examining a LEO to GEO transfer of a 5,000-kg satellite in 12 days which falls in the range of the optimum specific impulse considering efficiency and power system specific mass. Longer trip times are avoided to reduce damage to spacecraft components while lingering in the VanAllen radiation belts between LEO and GEO. Using the NASA-457 performance numbers from Table 3 and the simplifying assumption that only propellant mass is changing, the payload gains bismuth would have over xenon can be calculated. To calculate the estimated efficiency the thruster would have running on bismuth, the discharge voltage required to maintain

the same specific impulse is first calculated. It is then assumed that the thruster, operating on bismuth, would have the same efficiency as the xenon thruster at an identical discharge voltage. Because this voltage falls between the discrete data points from the NASA-457 test, the efficiency is quadratically interpolated between points using data from Table 3. Table 4 is a summary for several different specific impulses.

Table 4: Payload gains achieved by switching propellants from xenon to bismuth										
Specific Impulse, s	Xenon					Bismuth				
	Discharge Voltage	Power, W	$\eta$	Inert Mass, kg	Payload Mass, kg	Discharge Voltage for same Isp	Interpolated $\eta$	Inert Mass, kg	Payload Mass, kg	% Payload Increase
581	100	2008	0.32	1363	845	160	0.482	905	1304	54%
1176	150	6036	0.49	2170	1169	240	0.502	2119	1221	4%
1790	300	10287	0.53	3260	574	480	0.616	2805	1030	79%

Since the trip time of 12 days favors lower specific impulses, a bismuth thruster can deliver significantly more payload. Recalling earlier in this section, bismuth also has a lower ionization energy than xenon that would only serve to further increase anode efficiency. A crude approximation can be made to estimate the effect of the lower ionization energy by examining the maximum theoretical voltage efficiency from Equation (2.6). Since ionization energy directly impacts that term, it should be possible to estimate what effect a change in ionization energy has on the anode efficiency. In this case, it is assumed that any difference in the maximum theoretical efficiency will manifest itself as an increase or decrease in the voltage utilization efficiency; all other conditions held constant. Equation (2.14) is an expression for the calculations and the results are listed in Table 5.

$$\eta_{ion-cor} = \eta_{interpolated} \frac{\eta_{v-bi-max}}{\eta_{v-xe-max}} \quad (1.24)$$

Discharge Voltage	Interpolated $\eta$	Maximum Theoretical $\eta$	Ionization Corrected $\eta$	Payload Mass, kg	Payload Gain, kg
160	0.482	0.707	0.567	1439	523
240	0.502	0.901	0.531	1336	167
480	0.616	0.958	0.631	1097	523

Another likely anode efficiency gain that bismuth will have over xenon concerns bismuth's inherently higher electron impact-ionization cross-section at lower electron energies (corresponding to lower discharge voltages). Figure 5 indicates that bismuth is always more likely to be ionized than xenon especially at lower electron energies. This gain is harder to quantify without comprehensive bismuth performance data but suffice it to say, efficiency will improve.

From the analysis above, bismuth can hold significant advantages over other propellants for appropriate missions. By using a lower specific impulse propellant bismuth can perform certain missions requiring high thrust to power ratios either fast or more efficiently. This is not to say however that bismuth would be appropriate for all missions. For interplanetary or other very long duration missions, a high specific impulse is more advantageous.

### ***2.3 Disadvantages of Bismuth as a Propellant***

Bismuth has several disadvantages associated with it which make it challenging to use as a propellant. First and foremost is the fact that it is a solid at room temperature. Hall-effect

thrusters have no discernable way of directly using a solid phase propellant implying that the bismuth must be vaporized and with a 1564°C boiling point that is a non-trivial task – one which will consume much of the discussion contained within this dissertation. Aside from the problems required by the high-temperature handling of bismuth, when allowed to cool bismuth also expands 3.3% upon freezing. This liability creates serious concerns about the cracking of various thruster components when the thruster is turned off.

In a twist of irony, the ability of bismuth to condense on vacuum chamber walls and self pump is a huge liability for spacecraft. When it comes to deployment of such a thruster, bismuth could certainly condense on solar panels and decrease their ability to generate electricity. The exhausted bismuth could also contaminate other sensitive equipment on the satellite causing electrical shorts or other problems. However, many of these condensation difficulties can be mitigated with the judicious placement of the thrusters and / or plume shields on the spacecraft.

As a low-melting-point metal, bismuth readily makes alloys with other metals. This ability can create some serious corrosion issues when molten bismuth is placed in contact with an incompatible material. Great care must be taken to ensure that any part that is in contact with bismuth does not have the propensity to form any low-temperature alloys. Section 4.4 has a more detailed discussion of the implications of bismuth material compatibility.

More subtly, bismuth will see no benefits from an entire aerospace industry that is dedicated to xenon and other gaseous flow systems. There are certainly no flight qualified bismuth flow systems. In fact, measurement of bismuth mass flow rates represents a very significant challenge. A challenge which has been addressed in various schemes which are listed below.

## ***2.4 Other Bismuth Hall Thruster Efforts***

In the 1960-1970's research groups in both the United States as well as the Soviet Union were using a variety of different low- melting- temperature metals such as cesium, thallium, cadmium, lead, mercury, lithium and of course bismuth in EP thrusters.. Over the span of two decades an amazing array of different devices were developed to process and accelerate these elements but the toxicity or hazardous nature of most of these propellants eventually halted subsequent development; bismuth notwithstanding[35, 36].

The early efforts in using bismuth as a propellant were concentrated solely in the Soviet Union during the 1970's and early 1980's. From the mid 1980's until 2002 no subsequent research was underway anywhere in the world. Beginning in 2002, bismuth again became of interest for deep space missions and several projects funded by NASA as well as the United States Air Force resurrected some of the previous thrusters as well as created some new thrusters with the hope of improving the technology. What follows is a brief chronological description of each of the major efforts concerning the use of bismuth as a propellant.

### **2.4.1 TsNIIMASH D-160 and D-200**

The first attempts to use bismuth in a Hall thruster can be tracked back to the 1970's when the Russian government research organization TsNIIMASH (Central Scientific Research Machine Building Institute) created a very large and powerful Hall thruster designed to work with condensable metals such as bismuth, lead, thallium, mercury and cesium. Bismuth was ultimately chosen since it is the least toxic. Although the eventual application of the research was to create a thruster, other applications such as thermonuclear injectors and depositing thin films for semiconductor doping were also explored[35].

After several years of development, the first thruster to be tested on bismuth was the liquid-cooled, two-stage D-160 (160 is the average anode diameter in mm). The first stage, called the ionization stage, contains the gas-distributing anode and uses the second stage anode as a cathode. 150-250 volts is applied between the anodes in order to initiate a Paschen breakdown thereby creating a plasma. This plasma is then accelerated by the second stage anode (first stage cathode) by a 3-9kV potential. The reason for using multiple stages is to attempt to increase both lifetime and the efficiency at higher specific impulses. The D-200 very similar to D-160 except it has a larger 200 mm average anode diameter and has a radiatively cooled magnetic circuit.

Although there is not a wealth of data available on the performance of the D-160 and D-200, the D-160 reportedly ran at power levels from 20kW to 140kW with a specific impulse ranging from 4000-8000s and a reported anode efficiency (neglecting electromagnet supplies, heaters and cathode) of 70%. The D-200 ran in the 10kW-34kW range with a specific impulse ranging from 2000-5200s and anode efficiencies greater than 70%[37].

The laboratory mass flow system of both thrusters was designed to use gas-phase bismuth. Figure 8 illustrates the mass flow system. Bismuth is evaporated from a reservoir (1) by passing a very large amount of current through the reservoir (2) and the molybdenum propellant line (3). The molybdenum reservoir “dip tube” has very thin walls which causes a drastic resistance and will vaporize the bismuth in the dip tube if there is sufficient current flow. To prevent bismuth condensation, the propellant line is maintained at approximately 1200°C via the Ohmic heating caused by the large current going to the vaporizer. The evaporated gas was subsequently passed through the body of the thruster and into a 1000+°C preheated anode gas distributor. The high temperatures are required to prevent the bismuth gas from re-condensing at any point past the vaporizer. Mass flow rates were empirically derived by running extended

duration flow tests at a fixed vaporizer current and then calculating the change in mass of the bismuth reservoir.

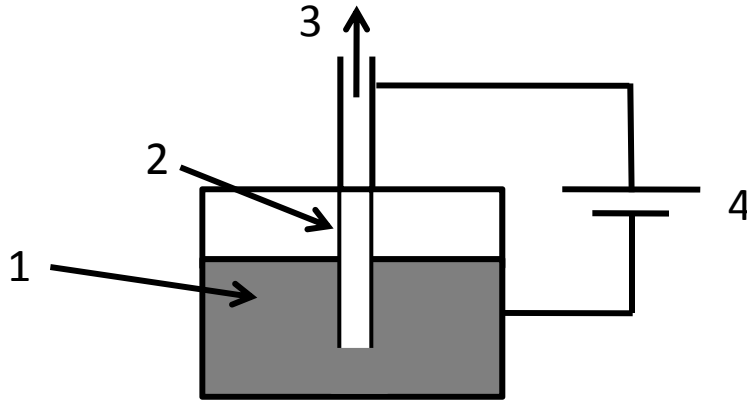


**Figure 8: Schematic of the TsNIIMASH feed system: 1) bismuth reservoir, 2) vaporizer, 3) molybdenum propellant tube, 4) electrical connection for the vaporizer.**

### **2.4.2 Very High Specific Impulse Thruster Anode Layer - 160 (VHITAL)**

In 2003, NASA officially established Project Prometheus with the goal to develop nuclear power in space for use on long-duration missions. High-specific-impulse electric propulsion systems were a natural fit for this environment since getting more thrust would be as simple as adding additional thruster modules. Although the United States had large xenon thrusters[34, 38], ground testing of the thrusters at high mass flow rates was beginning to reach the 3,500,000 l/sec nitrogen pumping speed of NASA Glenn’s Tank 5 - the fastest xenon pumping vacuum system in the world[10, 11]. This liability opened the door for the VHITAL program whose goal was to resume research on condensable propellants – namely bismuth. The VHITAL program was a joint effort between the Jet Propulsion Lab, Stanford University,

University of Michigan, Colorado State University and the Russian company TsNIIMASH Export with the goal of resurrecting and improving the old TsNIIMASH D-160[39].

One of the first improvements made was to remove the need to liquid-cool the magnetic circuit. This, however, limited the overall power level to 36kW, but that was not perceived to be a huge liability. Throughout the thermal analysis it was also determined that some of the waste heat generated by the back-streaming electrons could be used to maintain the anodes above a temperature where bismuth would condense upon them – in effect recycling heat that would otherwise have been shunted away. It was estimated that between 5-10% of total discharge power would be available for such use[40].

The mass flow system was also scheduled to be improved to a more flight-like system with the capability to measure flow rates in real time. Figure 9 is a rough schematic of the flow control system. Liquid bismuth enters on the left and is pressurized by argon gas to force the liquid into the pumping system. The pumping system is a DC electromagnetic pump which uses the Lorentz  $\mathbf{j} \times \mathbf{B}$  body force to move the conductive bismuth through a small channel[41].

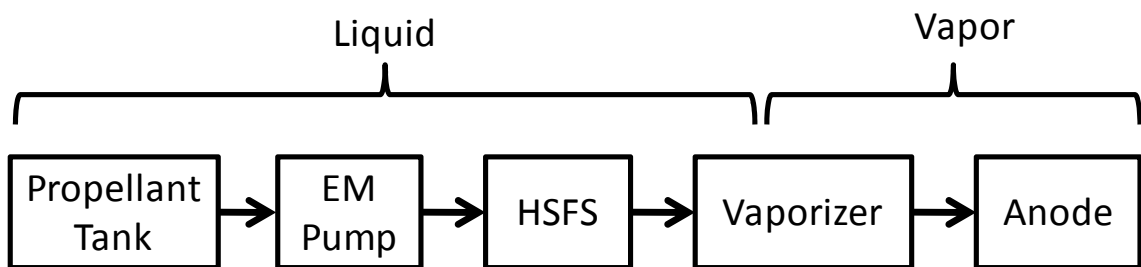


**Figure 9: Block diagram of the flight-like bismuth feed system assembly for VHITAL.**

After passing through the EM pump, the bismuth stream passes through a thermal tagging system called the Hotspot Liquid Flow Sensor (HSFS). The HSFS was designed to be an accurate way to measure the flow rate of bismuth in real time. This is done by constricting the

flow channel down to a very narrow passage. A 100-Amp, 1-ms pulse is applied to the poorly electrically conductive bismuth which creates a thermal spike due to Ohmic heating. A thermocouple downstream is used to measure the time it takes for the thermal spike to traverse the distance which can be used to calculate the flow rate of the bismuth[42].

The final stage of the improved mass flow system is the vaporizer and is illustrated in Figure: 10. Liquid from the EM pump enters on the left and passes through a stainless-steel to boron-nitride adapter. It then passes to a glassy carbon porous plug that has been radially perforated by a laser. Since bismuth is non-wetting on the carbon, only vapors can pass through the holes leaving the un-evaporated liquid behind (see Section 3.1 for a more detailed description of the concept). The heat for vaporization comes from an external carbon tube that the which is resistively heated to the approximately 1200°C required[43].

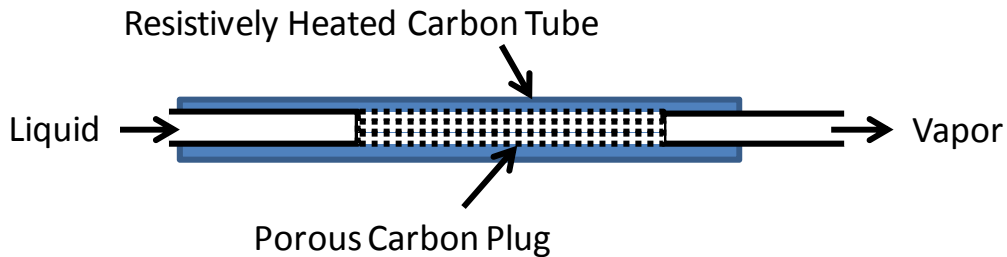


**Figure: 10 VHITAL bismuth vaporizer.**

Unfortunately, funding was terminated before all the constituent mass flow components could be integrated and tested as a system. However, VHITAL 160 was successfully test fired at TsNIIMASH in 2006 using the old gravity fed system from a D-160[44].

### **2.4.3 Busek Bismuth Hall Thruster**

Busek Co. has also been developing a bismuth Hall thruster under government contract. Due to ITAR restrictions, no technical details of the thruster can be included in this dissertation. The reader is referred to Ref [45] for a complete description.

## ***2.5 Summary***

In this chapter, bismuth was presented as a non-toxic, heavy metal that is used in a variety of every-day applications. Bismuth is also very well suited the use in Hall thrusters for low specific impulse missions and some rudimentary mission analysis was presented. The disadvantages of bismuth, namely the high boiling point and potential spacecraft contamination were also discussed. Finally, a literature review of previous bismuth thrusters was presented. The extreme temperatures these thrusters were operated at represent a significant issue. The following chapters will detail a potential solution to that problem.

### **3. Direct Evaporation of Bismuth**

While previous thrusters utilizing bismuth as a propellant have been successfully operated, the energetics associated with the vaporization and flow control of the bismuth vapors are quite unfavorable. The VHITAL / D-160 thrusters require 2000 Watts for external bismuth vaporization and an additional 3600 Watts of additional heat to ensure no condensation on any of the anodes. With a reported operating power of 25kW the absolute maximum efficiency possible would be 82% before the thruster is even turned on[39]. In 2007, VHITAL reported an anode efficiency of 56% using the D-160 style feed system, which quickly drops to below 46% when the heaters and the vaporizer are included[46]; a feat that is already possible with current xenon thrusters but without all the additional engineering headaches associated with high-temperature handling. The Busek efforts suffer from a similar energetic fate[45].

This chapter will focus on the underlying theory behind the direct evaporation concept which serves to eliminate efficiency problems just listed. Section 3.1 contains some basic evaporation gas kinetic theory which will be used to justify some estimations as to the bismuth evaporation rate as a function of temperature. In Section 3.2, bismuth evaporation will be examined in a more practical application in which the favorable energetics of using direct evaporations will be established. Section 3.3 will introduce the porous vaporizer as the device by which liquid bismuth will be separated from bismuth vapors. Finally, in Section 3.4 will examine the possibility of controlling the bismuth evaporation rate via segmented electrodes in the discharge chamber.

### 3.1 Evaporation Kinetics

Most people do not deal with the evaporation of metals on a daily basis but the same physical laws that cause the all the water in a neglected coffee maker to evaporate, also hold true when applied to less common applications. This section will examine some evaporation kinetics, which will set the stage for how bismuth is brought from a liquid to a gas without boiling.

Evaporation will take place if the temperature- dependant vapor pressure is greater than the ambient partial pressure for that gas species. Determining the exact evaporation rate though requires some kinetic analysis. Take the case of a pool of liquid bismuth sitting in a hot anode control volume inside of a discharge chamber as illustrated in Figure 11. In this case, bismuth is evaporating from a free surface but only atoms whose velocity is in the positive  $z$  direction will exit the anode (the dashed line) and leave the discharge chamber.

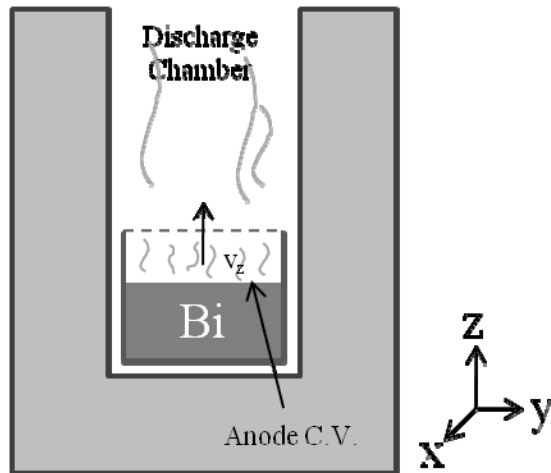


**Figure 11: A illustration of an open pool of bismuth evaporating in a discharge chamber. The dashed line represents the boundary where if gas molecules pass, it is assumed they will not return.**

The evaporation rate of bismuth from this surface can be calculated if it is assumed that the metal vapor in the immediate area of the liquid bismuth is isothermal and at the corresponding

equilibrium vapor pressure for that temperature and that the escaping gas has a mean free path greater than the length scale of the discharge chamber. If this is the case, the kinetic effusion analysis described in Ref [47] may be used. It can be assumed that the velocity of the atoms in the vapor phase follow the Maxwell-Boltzmann distribution function of

$$F_{esc} = \begin{cases} n \left( \frac{m}{2\pi kT} \right)^{\frac{3}{2}} e^{\frac{-m}{2kT}(v_x^2 + v_y^2 + v_z^2)} & \text{if } v_z > 0 \\ 0 & \text{if } v_z \leq 0 \end{cases} \quad (2.1)$$

where  $n$  is the number density in the local vicinity given by

$$n = \frac{P}{kT} \quad (2.2)$$

The parametric restriction on  $v_z$  is made because only atoms with a positive velocity in the  $z$ -direction will be in a position to leave discharge chamber.

$$j_{esc} = n \left( \frac{m}{2\pi kT} \right)^{\frac{3}{2}} \int_{-\infty}^{\infty} dv_x \int_{-\infty}^{\infty} dv_y \int_0^{\infty} dv_z e^{\frac{-m}{2kT}(v_x^2 + v_y^2 + v_z^2)} = n \sqrt{\frac{kT}{2\pi m}} = \frac{nv_{th}}{4} \quad (2.3)$$

where

$$v_{th} = \sqrt{\frac{8kT}{\pi m}} \quad (2.4)$$

With the assumptions from above,

$$n = \frac{P_v(T_{anode})}{kT_{anode}} \quad (2.5)$$

At this point, Equation (3.3), the flux rate, can be combined with Equation (3.5), the number density, to yield an expression for vapor escape rate per unit area as a function of anode temperature.

$$\frac{\dot{m}}{A} = \frac{mP_v(T_{anode})}{kT_{anode}} \sqrt{\frac{kT_{anode}}{2\pi m}} = \frac{P_v(T_{anode})}{\sqrt{\frac{2\pi kT_{anode}}{m}}} \quad (2.6)$$

### ***3.2 Evaporation of Bismuth***

The bismuth thrusters detailed in Section 2.4 all used gas-phase bismuth that was plumbed into the anode for use as a propellant. However, in each case there was a high temperature vaporizer that elevated the bismuth to a temperature such that sufficient evaporation occurred. While TsNIIMASH, NASA and Busek all proved it is certainly possible to use gas-phase bismuth in a traditional xenon style anode the extra power required to maintain bismuth as a gas and prevent it from re-condensing take a critical toll on overall efficiency. Energetics aside, it also creates a host of other material difficulties associated with high temperature isolators, valves and flow control devices.

Figure 12 is a functional diagram illustrating some of the temperatures required for a gas-fed bismuth thruster. Bismuth must first be brought to the liquid phase and then passed through some sort of liquid flow measurement system. As stated Section 2.4, various approaches of liquid

metering have been attempted ranging from simple sight glass measurements to more elaborate electromagnetic pumps with a thermal “tagging” system. Regardless of the approach used, the conductive nature of the propellant forces the mass flow control system to be at the same potential as the anode and introduces a very significant chance of arcing to surrounding structures. Once flow has been established or measured, the liquid bismuth must then move to the vaporizer to be boiled off into a gas. From there, the bismuth must traverse the distance from the vaporizer to the anode where it will finally get used as a propellant. All of the constituent propellant lines must be maintained at temperatures in excess of  $1000^{\circ}\text{C}$  to prevent the bismuth from re-condensing. The same holds true for the anode / gas distributor.

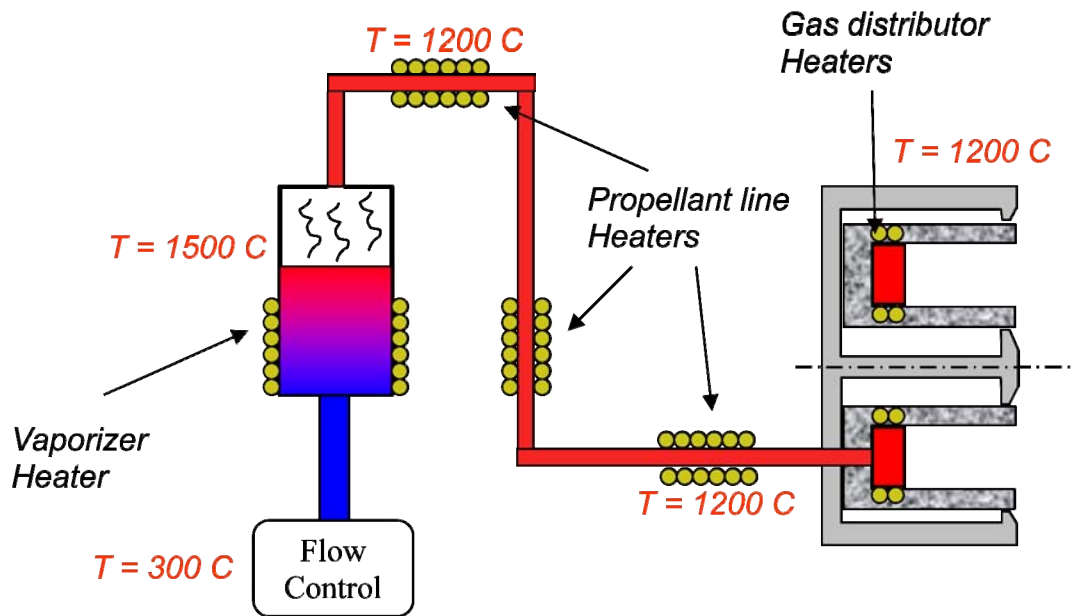


**Figure 12: Functional diagram of a gas phase bismuth Hall thruster showing the various heaters and approximate temperatures required**

When broken down to the simplest of terms, a Hall thruster somehow needs to have a gas injected into the discharge chamber to function. This begs the question: if it is so difficult to maintain a bismuth gas over any distance, why not just generate the gas at the point of delivery –

directly in the anode? The vaporizers used in all of the previous bismuth thrusters were very small in area to minimize the amount of mass that had to be at high temperatures. Returning to Equation (3.6), the expression for the per-unit-area evaporation rate as a function of temperature, if the evaporation surface area is increased, the temperature required for the same total evaporation rate will decrease. To apply some quantitative numbers to this situation, Equation (3.7) is the equilibrium vapor pressure in Pascals as a function of temperature in Celsius. For bismuth,  $A=13.317$ ,  $B=-10,114$  and  $C=-0.86$ [12].

$$P_v = \log^{-1} \left[ A + \frac{B}{T} + C \log T \right] \quad (2.7)$$

Figure 13 is a plot of the equilibrium vapor pressure and bismuth evaporation rate in milligrams per square millimeter per second from Equations (3.7) and (3.6) respectively.

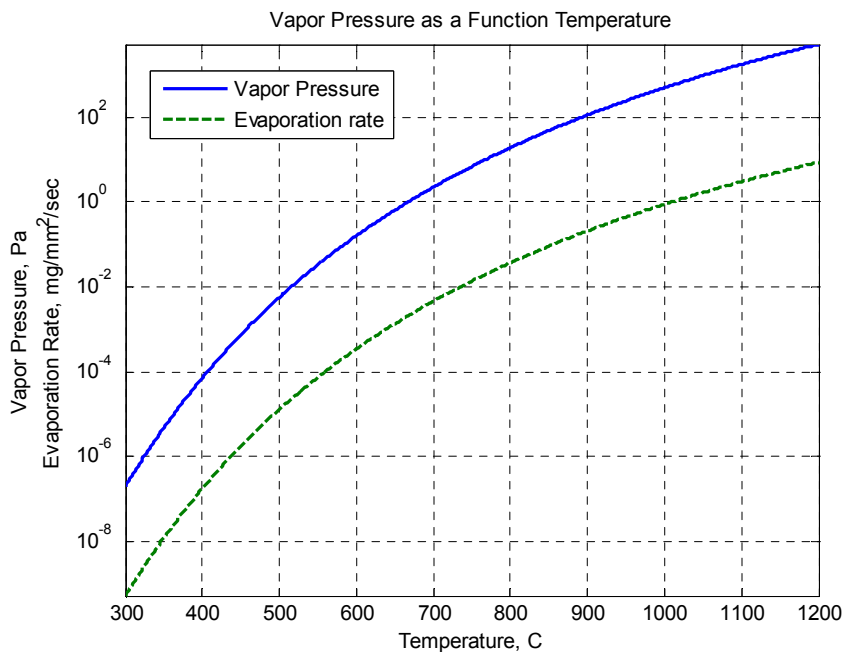


**Figure 13: Vapor pressure vs temperature and evaporation rate vs temperature for bismuth**

The original D-160 vaporizer has a relatively small surface area, although the exact number is not available, the dip tube has an estimated diameter of 5 mm meaning the total bismuth free surface evaporative area is about  $19 \text{ mm}^2$ . For D-160 to achieve the 9 mg/s flow rate, the vaporizer must be at approximately  $1000^\circ\text{C}$ . However, evaporation can only take place when the vapor pressure is greater than the ambient pressure and when there is a comparatively large evaporation rate, the local bismuth pressure may become significant thus forcing even higher temperatures. In any case though, this gas must not be allowed to re-condense so the propellant lines and the entire anode must be maintained at very high temperatures. All of the additional power required to keep various thruster parts at high temperatures is non-propulsive in nature and is not included in anode efficiencies but does reduce total efficiency.

Instead of using high temperatures to achieve mass flow rates, if the point of evaporation is moved to the much larger anode, larger surface areas can reduce the thermal requirements. For example, the design set-point for the direct evaporation bismuth Hall thruster developed in this dissertation calls for a mass flow rate of approximately 5 mg/s on an anode that has a surface area of approximately  $2600 \text{ mm}^2$ . Returning to Figure 13 the 5mg/s evaporation rate could be obtained at a temperature of only  $712^\circ\text{C}$ .

With much more modest thermal requirements, it would now seem that resistive heaters may be able to bring the anode to required temperature without nearly the power required in the previous vaporization schemes. While this is true, there is a better, more elegant solution. Hall-effect thrusters typically deposit between 10-20% of their total discharge power into the anode due to back streaming electrons eventually impacting the anode[48]. This is one of the primary efficiency losses and although great efforts have been made to minimize electron back streaming loss mechanism it still deposits a significant amount of thermal energy into the receiving anode.

Traditional xenon Hall thrusters would then seek to shunt the heat away from the anode to prevent any potential thermal damage. However, why not use the inherently deposited heat to drive the bismuth evaporation rather than external resistive heaters?

Figure 14 illustrates this concept. Liquid phase is maintained throughout the entire system except at the very last instant inside of the anode, a situation that will be explained in great detail in the next section. In this case, now the only external resistive power required is the modest 25-50 Watts necessary to keep the external bismuth reservoir above 271°C rather than the 1000's of Watts required for a gas-phase thruster.

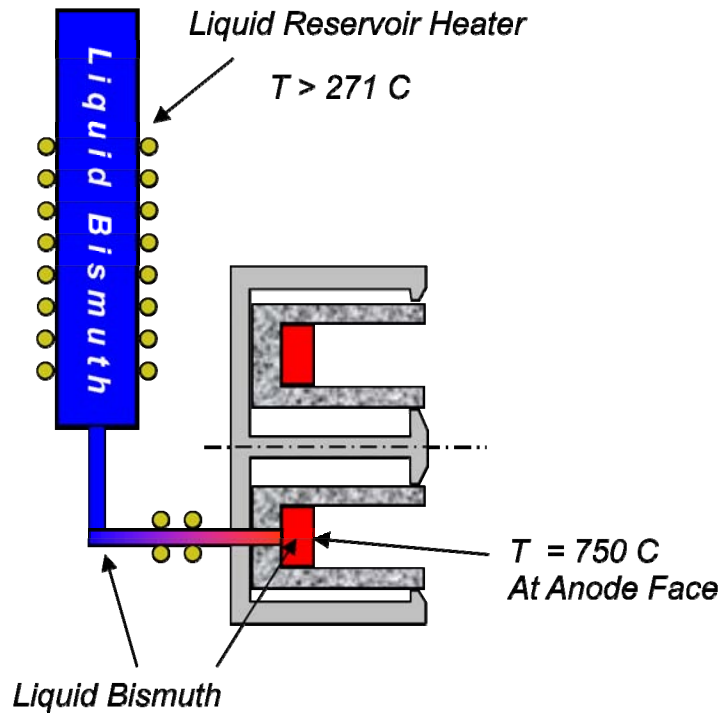


**Figure 14: Functional diagram of a liquid fed bismuth hall thruster utilizing direct evaporation**

Figure 14 also brings up an important design issue: what is keeping the pool of bismuth in the anode from just dumping out onto the vacuum chamber floor? A part called the porous vaporizer

will serve to restrain the liquid bismuth in the anode and yet allow vapors to pass through into the discharge chamber.

### ***3.3 The Porous Vaporizer***

As previously mentioned, evaporation from a free surface of bismuth provides a predictable and elegant way of efficiently obtaining bismuth vapors. However, expecting a pool of bismuth to stay put inside of a Hall thruster is clearly an unrealistic situation. To that end, the porous vaporizer came into existence. On a basic level, the vaporizer is simply a device to separate the phases of the bismuth; liquid on one side, gas on the other. Previous research efforts[45, 49] have used porous discs for similar phase discrimination, but then introduced some additional gas handling hardware to conduct the vapors to their final destination. The direct evaporation concept seeks to remove that burden by using a porous vaporizer to retain the liquid in the anode while allowing vapor to flow through.

To understand how the porous vaporizer works, interfacial engineering concepts must be brought in to bear on the situation. If a liquid placed on a given solid substrate in an environment with gravity, the surface tension forces involved will seek to minimize the total interface energy by increasing or decreasing the interface contact area. A liquid is defined as non-wetting if the angle  $\theta$  between the solid and the liquid is greater than  $90^\circ$  indicating that liquid is attempting to reduce the interface contact area. Figure 15 illustrates wetting and non-wetting contact angles.

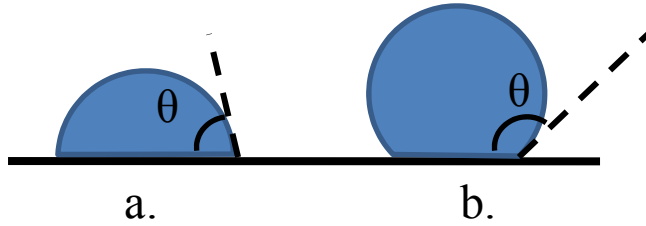


**Figure 15: Illustration of contact angles: a) wetting b) non-wetting.**

The liquid-bismuth porous vaporizer interactions are governed by very simple interfacial engineering principals. Figure 16 illustrates the governing forces in the case of a non-wetting liquid impinging on a capillary. If a non-wetting liquid is placed in contact with a capillary the intrinsic surface tension force  $F_{ST}$ , works to counteract the applied pressure force  $F_p$  to retard the liquid from entering the capillary. A trivial derivation reveals that the surface tension pressure can be expressed as

$$P_{ST} = \frac{2\gamma}{r} \cos \theta \quad (2.8)$$

where  $\gamma$  is the surface tension of the liquid,  $r$  is the radius of the capillary and  $\theta$  is the contact angle of the liquid on the solid. As long as  $F_{ST}$  is greater than the applied pressure force  $F_p$  the liquid will not flow through the capillary.

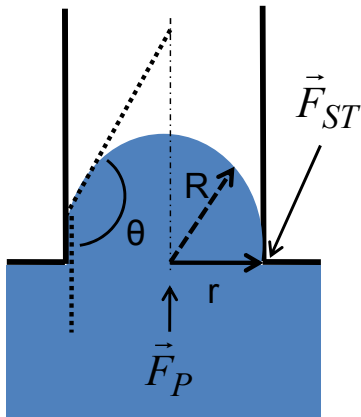


**Figure 16: Schematic of interfacial forces in response to a non-wetting fluid impinging on a capillary**

To extend this relation to a porous vaporizer we make a simplifying assumption that each pore behaves like a capillary of similar size. At the liquid/porous surface interface, the liquid bismuth is now pinned to one side of the vaporizer and prevented from passing through the pores if they are sufficiently small. A subtle yet critical aspect of the surface tension pinning back the liquid is that a bismuth “free surface” is created allowing evaporation to commence at sufficiently high temperatures.

As suggested before, the inherent impact of the back-streaming electrons into the anode deposits a significant amount of thermal energy. This heat can then be *directly* used to evaporate the bismuth and if designed properly, can eliminate the need for additional heaters. Figure 17 illustrates the combined concept.

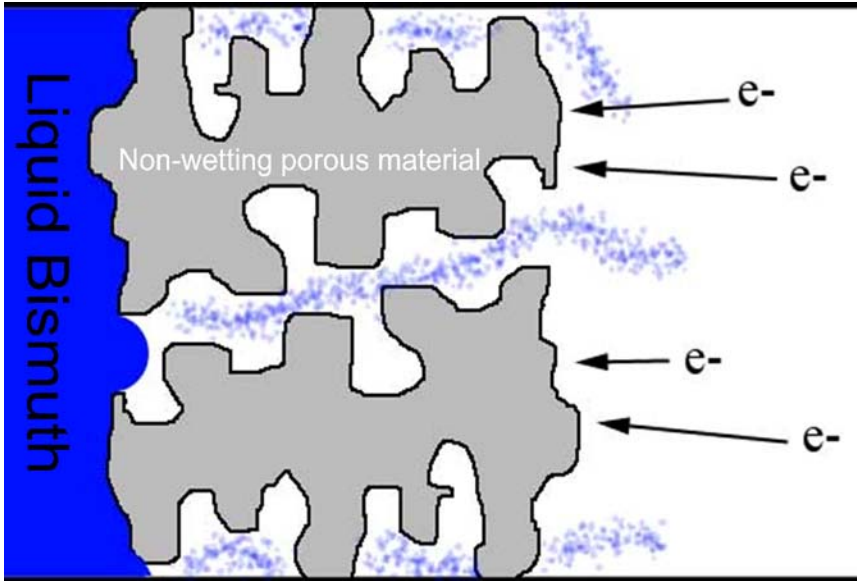


**Figure 17: Evaporation schematic showing bismuth evaporating from the free surface created by the porous plates and the electrons depositing heat to drive the evaporation.**

However, what if the back streaming electrons are depositing too much heat? Based upon the arguments above, the evaporation rate would increase and the system could potentially run out of control. To prevent an uncontrolled evaporation runaway, a method was developed to control exactly how much thermal energy was being deposited into the anode.

### ***3.4 Thermal Control with Segmented Anodes***

Designing a thruster that dissipates exactly the right amount of power into the porous vaporizer to emit the precise propellant flow rate required for the thruster represents a potentially unstable open-loop control system: as temperature increases, mass flow will increase, which increases discharge power which will increase temperature and so on. To alleviate that potential problem a segmented-anode design was adopted to achieve closed-loop control of the porous vaporizer temperature. The design utilizes three separate electrodes: the traditional main anode where the bismuth evaporation will occur and two inert “shim” anodes - one inner and one outer

–electrically and thermally isolated from the main anode. Figure 18 shows a cross section of the segmented-anode thruster.

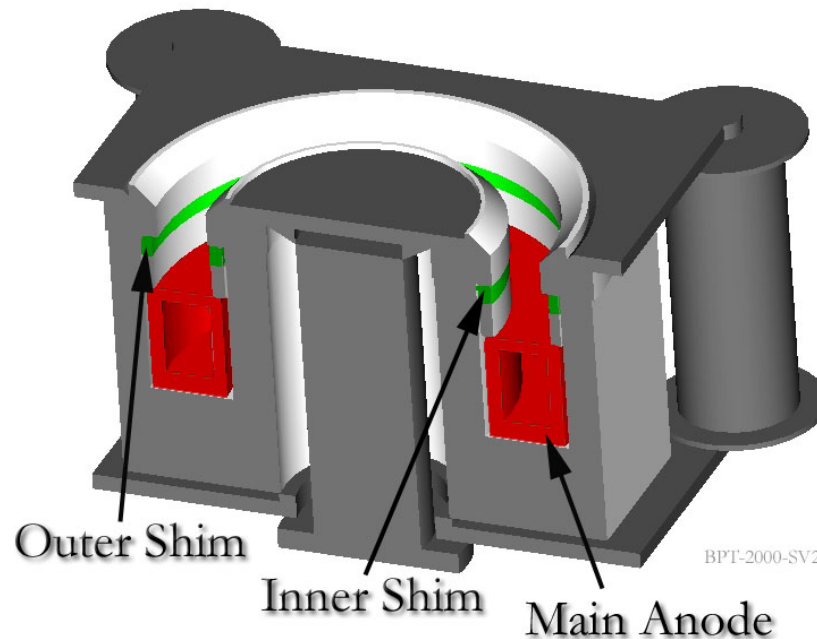


**Figure 18 Segmented anode thruster**

The main anode temperature is controlled by sharing the plasma discharge current with a set of electrically isolated shim anodes on the inner and outer wall. The shim anodes are inert (stainless steel or molybdenum) and are not bismuth vapor sources. By varying the shim voltage with respect to the main anode, the plasma current and, hence, electron heating can be shared between the shims and main, thus controlling the porous vaporizer temperature and the evaporation rate. The mass flow rate is then bounded above by the equilibrium main anode temperature obtained when 100% of the discharge current is attached to the main, and bounded below by the temperature achieved when 100% of the current is attached to the shims. Figure 19 is an illustration of this concept.

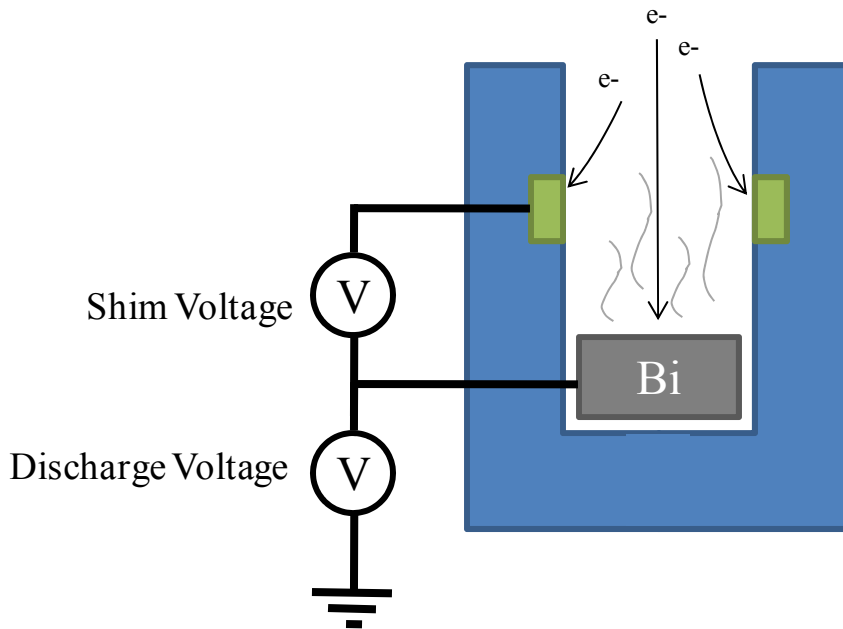


**Figure 19: Electrons impacting and depositing heat to drive direct evaporation**

### ***3.5 Summary***

In this chapter the basic underlying mechanism for the direct evaporation scheme was presented. By utilizing evaporation kinetics and surface tension forces, bismuth can evaporate at rate suitable for use in a Hall thruster without the maintain gas phase throughout the entire propellant supply system. Bismuth will evaporate from the free surface created inside of the porous vaporizer which is heated by back streaming electrons inherent in the discharge thus removing the need for auxiliary heaters. Finally, since precise temperature control of the porous vaporizer is critical for constant evaporation rates, inert “shim” anodes demonstrated that by shifting around current attachment points in the discharge chamber, the main anode temperature could be significantly varied.

## 4. Experimental Development of the Bismuth Hall Thruster

The development of the direct evaporation bismuth Hall thruster has been far from a linear progression of events though two distinct paths were simultaneously taken. The first was to explore what effects the segmented anodes had upon the performance and general operation of a Hall thruster. By using xenon as a propellant in these evaluations, it was vastly easier to study and understand the segmented anode without the added complication of maintaining a steady evaporation of bismuth. The second path taken was concerned with the technical details of handling a high temperature conductive metal and more importantly how to properly and efficiently integrate a propellant distribution system into a Hall thruster. This chapter is essentially a step-by-step look at how development proceeded and examines some of the practical aspects of the research as well as introduce some experimental results which were used to guide the final bismuth thruster design whose operation and performance is explored in Chapter 6.

This chapter will begin by introducing some thermal modeling in Section 4.1 where the thermal dependency of anode power fractions are briefly explored. Section 4.2 describes the experimental facilities used to perform both the xenon and bismuth tests. In Section 4.3, the thruster is tested on xenon and thermal control via segmented electrodes is successfully demonstrated and found to have a negligible impact on thruster performance. Section 4.4 introduces the first experimental work with bismuth. Practical issues relating to material bismuth compatibility are addressed. In Section 4.5 the first tests of the porous vaporizer are performed to attempt and relate liquid extrusion pressures to average pore size. With a better understanding of liquid bismuth extrusion, Section 4.6 introduces the first bismuth-xenon mixed-mode operation. In this case, the thruster is warmed up on xenon, before transferring over to bismuth only operations. Mixed-mode operation, while successful, did create some problems with respect to

shim anode survivability so Section 4.7 covers the integration of molybdenum anodes.

Unfortunately, molybdenum shim anodes introduced a still unresolved poisoning of the discharge plasma. Section 4.8 then covers successful bismuth operation without any shim anodes.

Although thruster operation was becoming rather easy, Section 4.9 explores the problem of vaporizer pore growth and the implication it has on lifetime. To alleviate some of the overheating problems, a new resistive heater is designed in Section 4.10 which removed the need to preheat the thruster on xenon. Finally, Section 4.11 details the flow of liquid bismuth throughout the thruster.

### ***4.1 Thermal Modeling***

A significant amount of thermal modeling was performed early in the development process to investigate the feasibility of the direct evaporation idea. There were several concerns to be addressed. First was ensuring that the heat deposited by the back streaming electrons would be sufficient to maintain a suitable temperature for bismuth evaporation. Second was to investigate the feasibility of using the shim anodes to control the temperature of the porous vaporizer. Finally, it was important to ensure that any thermal design did not allow any part of the magnetic circuit to exceed the Curie point.

In 2004, Aerojet donated a laboratory BPT-2000 xenon Hall thruster to the MTU Isp Lab pictured in Figure 20. The BPT-2000 is a 2-kW-class Hall thruster with a 1200-2700 Watt operational power range, 250-400 Volt discharge and a facility-corrected efficiency of 48%[50]. Eventually the thruster would be modified, but subsequently fabricated parts were designed to match the original BPT-2000 dimensions as close as possible.



**Figure 20: Original unmodified Aerojet BPT-200 mounted on a thrust stand**

The principle mechanical design constraint for this project was maintenance of the magnetic circuit geometry. This desire to retain magnetic circuit compatibility constrained the dimensions of the supporting boron-nitride body and/or more specifically the volume allotted for the discharge chamber.

To investigate the thermal properties of the segmented Hall thruster, a fully three-dimensional thermal model was created in IDEAS-NX and a variety of simulations were conducted. Of principle interest was the potential throttleability of the thruster – that is how much of a temperature swing could the main anode achieve as current is shifted between the electrodes. Figure 21 is a representative solid model with labeled parts used for the thermal modeling.

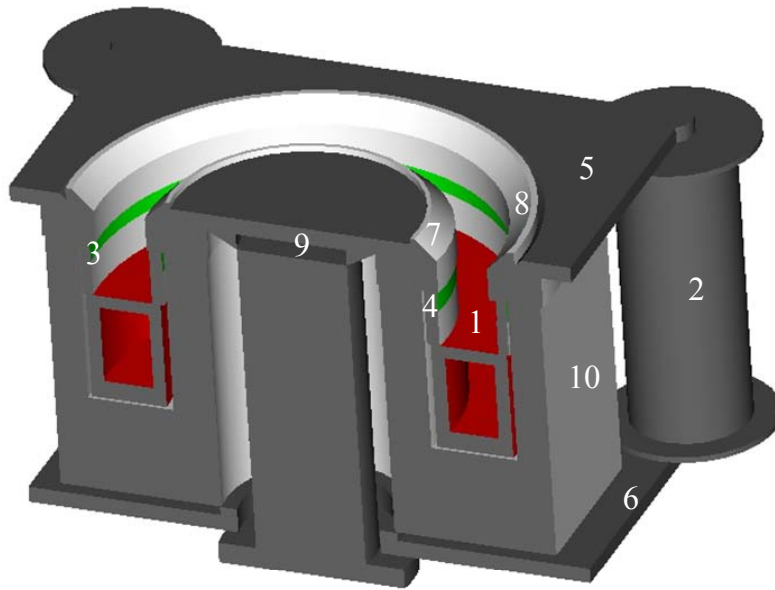


**Figure 21: Solid model showing the parts used during thermal modeling: 1) anode face, 2) electromagnets, 3) outer shim anode, 4) inner shim anode, 5) front plate, 6) back plate, 7) inner BN guard ring, 8) outer BN guard ring, 9) center magnetic pole and 10) BN body.**

Table 6 lists the typical boundary conditions that were applied to the various thruster elements. Thermal contact resistance was also included and the interface values used are listed in Table 7. Modeling previously performed by Aerojet on this particular class thruster provided guidelines as to how much power is being deposited in various areas of the thruster during operation. The emissivity's and contact resistances used in the models were later validated and enhanced to better match actual experimental results (see Section 4.3).

<b>Table 6: Typical boundary conditions used for thermal modeling</b>		
<b>Boundary</b>	<b>Type</b>	<b>Value</b>
Main Anode Face	Heat Deposition	0-15% Pdis
Inner Shim Anode	Heat Deposition	0-15% Pdis
Outer Shim Anode	Heat Deposition	0-15% Pdis
Electromagnets	Heat Deposition	59 Watts total
Inner BN Guard Ring	Heat Deposition	6% Pdis
Outer BN Guard Ring	Heat Deposition	4% Pdis
BN Body	Radiation	$\epsilon=0.7$
Inner BN Guard Ring	Radiation	$\epsilon=0.7$
Outer BN Guard Ring	Radiation	$\epsilon=0.7$
Main Anode Radiation	Radiation	$\epsilon=0.4$
Front Plate Radiation	Radiation	$\epsilon=0.6$
Back Plate Radiation	Radiation	$\epsilon=0.6$
Mounting Plate	Heat Sink	20°C

<b>Table 7: Typical thermal conductivities between thruster elements for thermal modeling</b>	
<b>Interface</b>	<b>Applied Thermal Conductivity (W/m K)</b>
BN Body-Back Plate	20
Electromagnets – Back Magnetic Plate	40
Electromagnets – Front Magnetic Plate	40
Outer BN Guard Ring – Front Magnetic Plate	20
Outer BN Guard Ring – BN Body	20
Inner BN Guard Ring – BN Body	20
Inner BN Guard Ring – Center Magnetic Pole	20
Outer Shim Anode – BN Body	10
Outer Shim Anode – Outer BN Guard Ring	10
Inner Shim Anode – BN Body	10
Inner Shim Anode – Outer BN Guard Ring	10
Main Anode (all coincident surfaces) – BN Body	10
Center Magnetic Pole – Back Magnetic Plate	40

Figure 22 is an example of a 1.35 kW modeling run. In the upper case, 202.5 W (15% of 1.35 kW) is deposited into the main anode with no power applied to the shim anodes. In this particular case, the maximum temperature of the main anode was near 535°C with the shim anodes reaching a similar temperature. In the lower case, the entire 202.5 W was shifted from the main anode to the inner shim anode. No power was applied to the outer shim anode as it was experimentally determined that current will almost exclusively attach to the inner shim anode. In this case, the main anode cooled off to 480°C while the inner shim anode heated up to 630°C.

The outer shim did not stray far from 425°C in either case. The observed 55°C temperature change in the main anode would provide nearly an order of magnitude change in bismuth flow. However, the maximum anode temperature did not exceed 535°C which is far below the 700°C+ required for the desired evaporation rate. The implication of this was that the anode face area would have to decrease to increase the power density therefore driving the temperatures higher. The thermal modeling performed also suggested that the magnetic circuit would not exceed the Curie temperature. These models were also experimentally explored which is documented in Section 4.6.

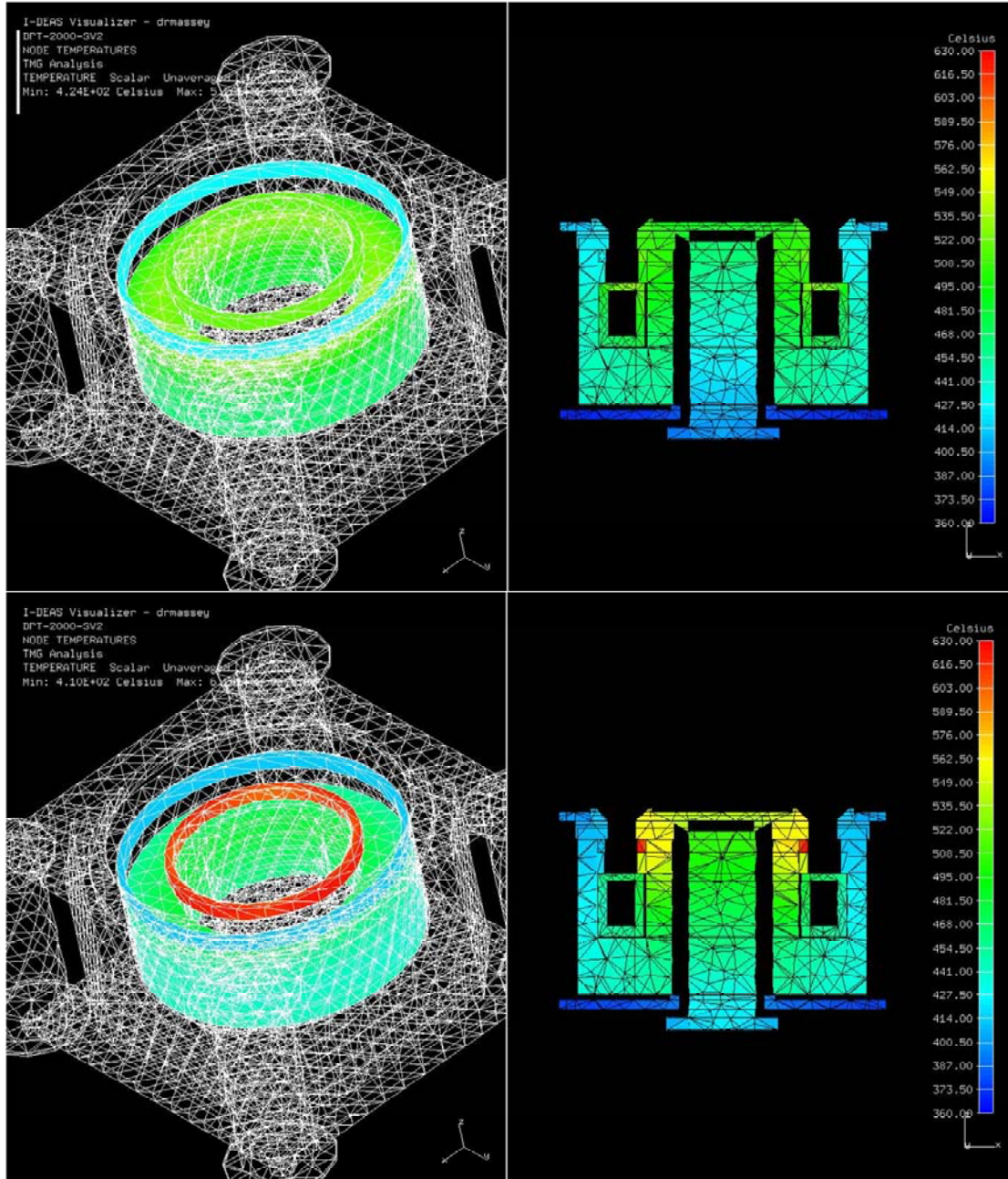


Figure 22: Selected IDEAS thermal models with different loads on the anodes.

## ***4.2 Testing Facilities and Instrumentation***

All xenon tests were performed in the Isp Lab's Xenon Test Facility on the campus of Michigan Technological University. The facility is comprised of a 2-m-diameter by 4-m-long vacuum tank. Rough pumping is accomplished by a two-stage rotary oil-sealed vacuum pump with a Roots blower, capable of pumping at 400 cubic-feet-per-minute. High vacuum is achieved through two 48-inch-diameter cryopumps, capable of pumping 120,000 liters-per-second on nitrogen. The background pressure was maintained below  $2.6 \times 10^{-5}$  Torr (corrected for xenon) during all tests. Anode and cathode xenon flow into the tank was controlled via 200 and 20 SCCM MKS mass flow controllers, respectively. A xenon-fed laboratory  $\text{LaB}_6$  cathode was used to sustain the plasma discharge. Figure 23 is a photo of the Xenon Test Facility.



**Figure 23: Xenon Test Facility**

All bismuth tests were also performed in the Isp Lab's Condensable Propellant Facility on the campus of Michigan Technological University. The bismuth test facility is comprised of a 2-m-diameter by 4-m-long vacuum tank. Rough pumping is accomplished by a two-stage rotary oil-sealed vacuum pump with a Roots blower, capable of pumping at 400 cubic-feet-per-minute.

High vacuum is achieved using three 28,000-RPM magnetically levitated turbomolecular pumps capable of pumping 2,000 l/sec each providing a robust, oil-free vacuum with a base pressure below  $1 \times 10^{-6}$  Torr. Anode and cathode xenon flow into the tank was controlled via 200 and 20 SCCM MKS mass flow controllers, respectively. A xenon or krypton-fed laboratory  $\text{LaB}_6$  cathode was used to sustain plasma discharge. Figure 24 is a photo of the Condensable Propellant Facility.



**Figure 24: Condensable Propellant Facility**

Thrust measurements were taken using a NASA-Glenn-style inverted pendulum thrust stand and recorded via a computer-controlled data acquisition system[51]. Thrust measurements have an estimated experimental uncertainty of  $\pm 5\%$ . Thermal measurements of the thruster were taken using K-type thermocouples that were directly welded to the shim anodes and were welded or press fit against the back face of the main anode. However, since certain thermocouples were at anode potential, temperatures were taken recorded manually through the use of electrically isolated thermocouple monitors. The thermocouple monitors have an uncertainty of  $\pm 1\%$  of full scale. When possible, voltage and current measurements were taken

by a computer-controlled data acquisition system. While operating on solely bismuth, facility pressure was below  $5.5 \times 10^{-5}$  Torr corrected for xenon. There is no bismuth gas correction factor available.

### ***4.3 Segmented Anode Xenon Performance***

As previously mentioned, it was important to establish the validity of using segmented electrodes for thermal control as well as examining any impact such a configuration has on thruster performance. Other research groups have looked at using segmented electrodes before, but in a configuration not explicitly applicable to this case as most segmented efforts were directed at reducing plume divergence[52-54].

The Hall thruster employed for the preliminary segmented anode tests uses the magnetic circuit from an Aerojet BPT-2000, and a boron-nitride body which has been retrofitted with segmented anodes as described in Section 3.4, the necessary power connections, and instrumentation for temperature measurements. As shown in Figure 25, adjustment of the current sharing properties of the anodes is accomplished by varying the voltage on either the shim anodes or the main anode. Electrical connections to the shim anodes were made through the use of high temperature wire welded directly to the anode and passed through the boron-nitride thruster body. Thermocouples were connected similarly.

Performance measurements were taken at anode voltages of 300 and 400 Volts and at xenon mass flows of 4, 5, 6 mg/s to ascertain performance trends. At each operating point, the magnetic field was adjusted to minimize the total discharge current when the shim and main anode voltages were equal. This value of electromagnet coil current was then sustained as discharge current was shifted from the shim anode to the main anode. When the shim and main anodes were at the same potential, the majority of current would attach to the shims. The shift in

current was obtained by leaving the main anode potential fixed and lowering the shim anode potential. In all cases, the shims never needed to be lowered more than 40 Volts below the main anode for complete main anode current attachment.

Figure 25 illustrates a typical case. In this figure, the main anode is held at 400 volts and the flow rate is 6 mg/s of xenon. The efficiency reported is anode efficiency. As can be seen,  $I_{sp}$  and efficiency all decrease slightly as current is shifted from the shim anodes to the main anode while the total discharge current and power remains largely unchanged. The changes in  $I_{sp}$  and efficiency at all operating points examined are illustrated in Figure 26.

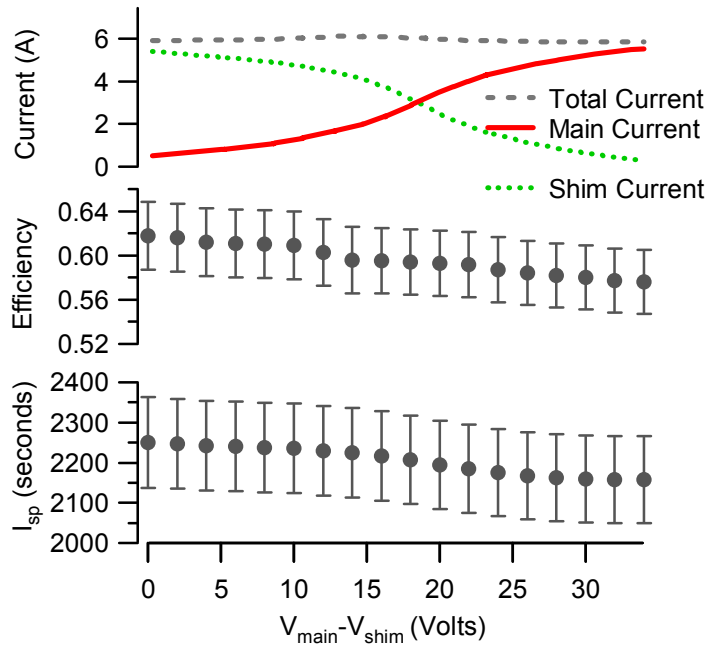


**Figure 25 - Results from a typical operating point. Main anode voltage is  $V_{main} = 400$  volts and flow is 6 mg/s of xenon. Experimental error for efficiency and  $I_{sp}$  is +/- 5% of the value.**

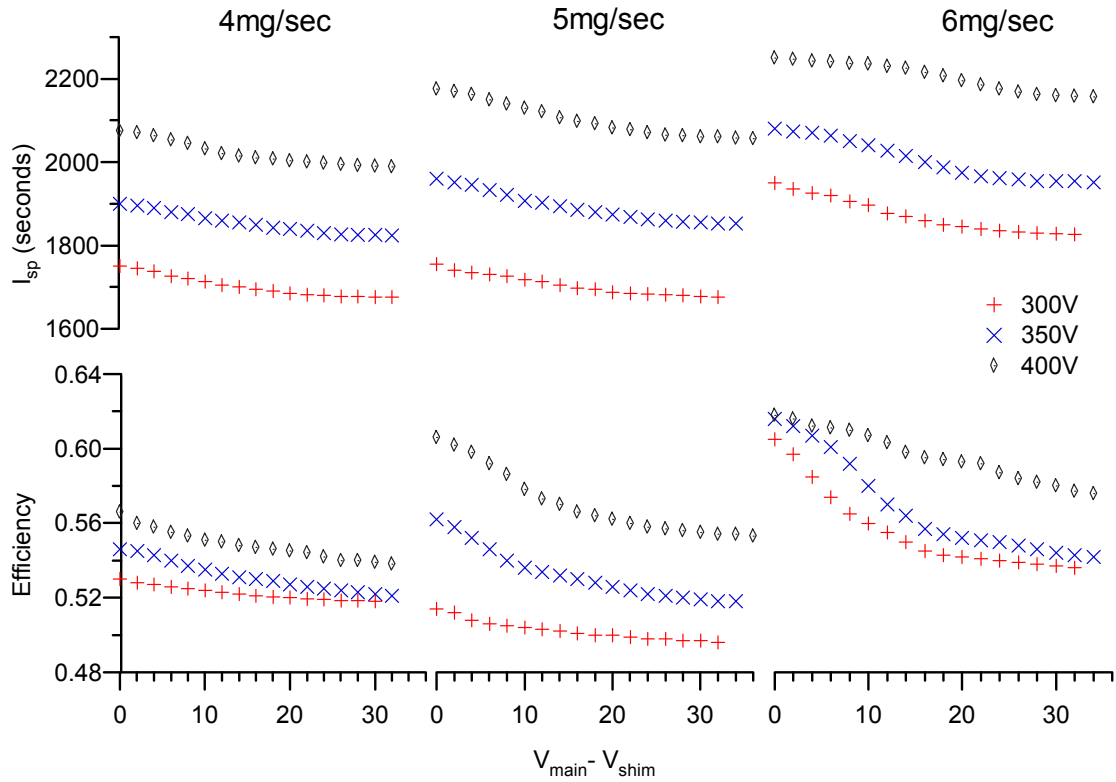


**Figure 26 - Thruster performance results showing the variation in anode efficiency and specific impulse as the discharge current is shifted between main anode and shims. Experimental error for efficiency and  $I_{sp}$  is +/- 5% of the value.**

After completion of performance testing, the variation in anode/shim temperature as a function of current attachment was investigated. To establish the range over which the temperatures could be controlled, the thruster was allowed to come to thermal equilibrium with the current completely attached to each anode. Figure 27 shows how the thruster responds to both current shifting and mass flow increases with the main anode voltage fixed at 400 Volts. At each operating point, thermal equilibrium was achieved in about 40 minutes.

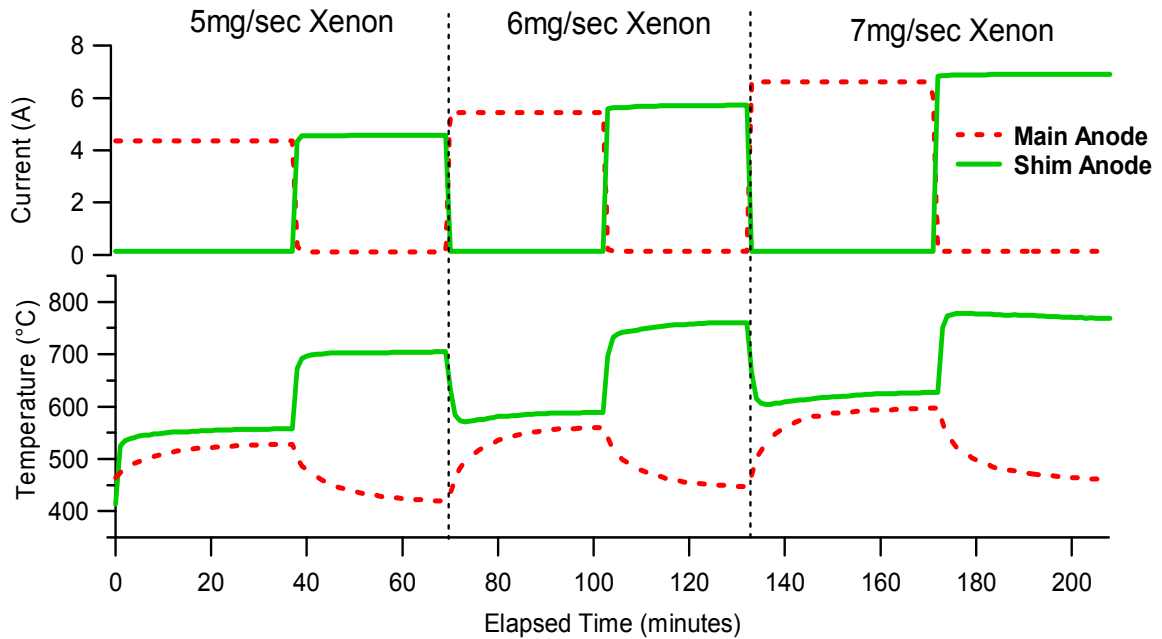


**Figure 27 - Thruster thermal variation due to varying current attachment. Main anode voltage was held constant at 400 Volts**

Performance testing demonstrated that operating with segmented anodes does not significantly alter thruster performance. Shifting current attachment from shims to main anode neither affects stability nor requires significant modifications to the magnetic field. Varying the current attachment causes less than a 10% change in shim voltage and 5% change in specific impulse. During testing no effort was made to optimize the magnetic field as the current attachment point was moved for a fixed main anode voltage. It may be possible to recover the slight efficiency loss seen as the shim voltage was reduced by adjusting the magnetic field at each value of current sharing fraction.

It is interesting to note that there is evidence that the ionization region is upstream of the shims. The required reduction in shim voltage and subsequent reduction in  $I_{sp}$  is consistent with the ion velocity loss one would expect by lowering the accelerating voltage. At 400 volts and

6mg/s of xenon flow with all the anodes at the same potential the specific impulse was 2,250 seconds corresponding to an effective accelerating voltage of 332 volts. When the shim voltage was lowered to 366 volts (to shift current to the main anode) the specific impulse decreased by 93 seconds to 2,157 seconds corresponding to an effective accelerating voltage of 305 volts. So by reducing the shim voltage by 34 volts the effective accelerating voltage was reduced by 27 volts which is well within the realm of experimental uncertainty.

In this application, the goal of using segmented anodes is to enable thermal control of the main anode for use in eventual bismuth evaporation. In each of the cases presented in Figure 4, a 50+ degree variation in temperature can be obtained in a matter of minutes for the main anode, and seconds for the shim anode. This temperature swing would cause a 63% change in the bismuth evaporation rate, providing a wide range of throttleability. Moreover, at the tested power levels the anodes are both thermally stable and well within the working temperature of the constituent materials. From these results, it is clear that using segmented anodes for thermal control is a valid approach.

Although thermal testing showed the ability to substantially vary the anode temperature, the maximum temperature achieved was well below that required for sufficient bismuth evaporation for self-sustaining operation. It was previously determined that an anode temperature of 750°C was required but even running at 2.4kW the main anode temperature reached a maximum 597°C. To gain the additional 150 degrees, thruster power could be further increased at the expense of thruster lifetime. A better option was deemed to be a reduction in anode face area thereby increasing the power density as well as improved thermal insulation. During xenon testing a power density of 0.5 W/mm<sup>2</sup> of anode face area achieved 597°C. Thermal modeling suggested that a power density of 1W/mm<sup>2</sup> would be sufficient to achieve the goal of 750°C.

Subsequently, a new anode with approximately half the face area was fabricated to meet the estimated power density requirements. The smaller anode left significant physical gaps in the discharge chamber, which could potentially affect thruster performance. In order to quantify the effects of the change, thruster performance was again evaluated. Figure 28 is plot of a typical case. The changes in efficiency and specific impulse were within the realm of experimental error and were therefore deemed as inconsequential.

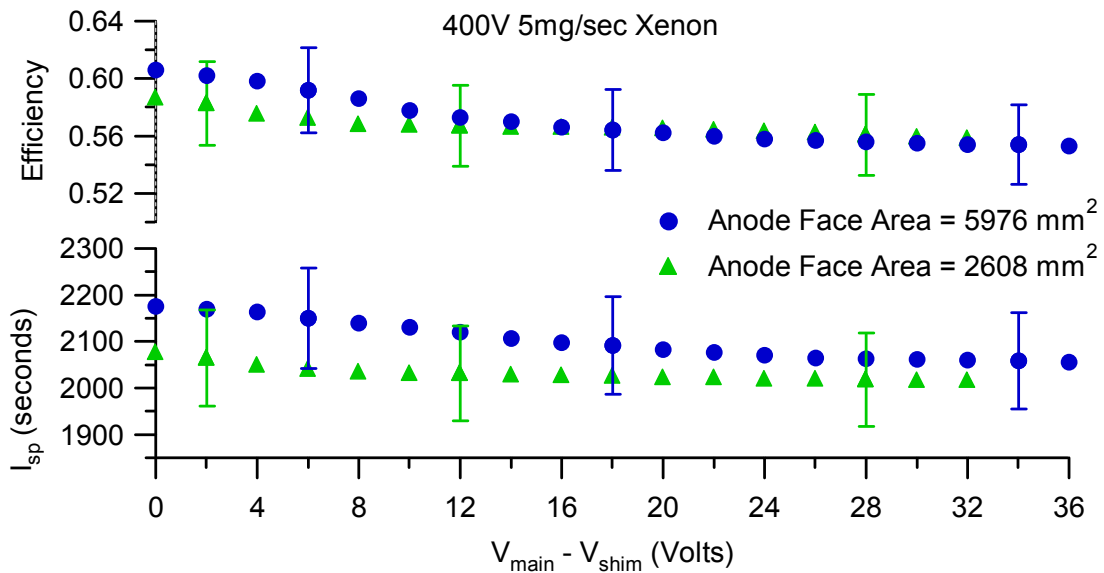


**Figure 28 - Typical operating performance**

A much more detailed study of the effect of segmented anodes on the performance, ion populations, ion acceleration characteristics and plume divergence was conducted by Kieckhafer in 2007. The following final conclusions were that shifting current attachment from the main anode to the shim anode had no statistically significant impact on performance; multiply charged ion populations also remained unchanged; the most probable ion energy was strongly dependent on the shim anode voltage and that plume divergence decreased by approximately 10% when the current was attached entirely to the shims[55].

#### ***4.4 Bismuth as an Engineering Material***

Using bismuth in a high-temperature engineering environment is a significant challenge. This section presents some of the practical aspects and pitfalls of using bismuth as a propellant in a Hall thruster. While there were iterations too numerous to mention throughout the development of the bismuth Hall thruster, the experiments included here highlight some of significant findings which directed subsequent efforts.

The method of direct evaporation of bismuth relies on the principal that if a pool of molten bismuth is sufficiently hot, significant evaporation will occur. To that end, the first steps in the bismuth handling realm of this research project were concerned with verifying bismuth evaporation and therefore developing a working knowledge of high temperature materials. Since the end goal was to create an anode that could be directly integrated into an existing Hall thruster, the high temperature developmental apparatuses always resembled a traditional anode but were referred to as “bismuth boilers”.

The first series of testing demonstrated any anode heating method must make exception for the necessity of a self contained volume of bismuth – that is only metal to metal seals can be used where there is to be liquid bismuth. Liquid bismuth has a viscosity similar to water and should be treated as such. The solution to this problem is illustrated in Figure 29. In this model, the bismuth is contained in a separate hollow anode annulus and is heated from below. The heater for this application was a commercially available 1200°C rated tantalum wire sheathed by MgO and contained within an additional tantalum sheath. The addition of the MgO between tantalum layers allows the inner wire to be electrically isolated from the outer sheath and therefore isolated from the anode. This was deemed an important asset because it would remove

the necessity to float a heater power supply if this was the design selected for integration into a Hall thruster.

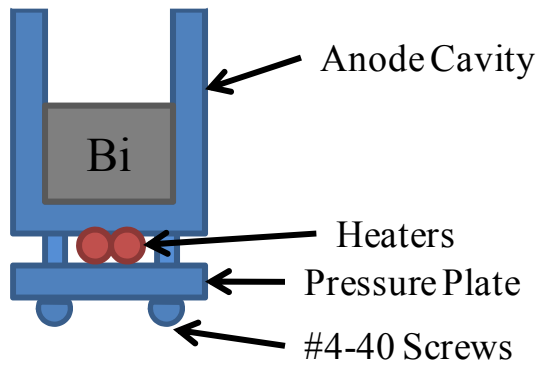


**Figure 29: Cross-section of a bismuth boiler with a heater isolated from liquid bismuth**

The first few runs with this design demonstrated vast improvements in high temperature performance but the bismuth spattering around the assembly indicated that the bismuth was locally boiling inside of the cavity most likely at the heater interface despite not reaching temperatures above 900°C on the exterior of the anode. To eliminate the spattering, two stainless steel diffuser plates with numerous 1/16” holes drilled through them were fitted into the anode cavity. Figure 30 is a photograph of this implementation before it was used.

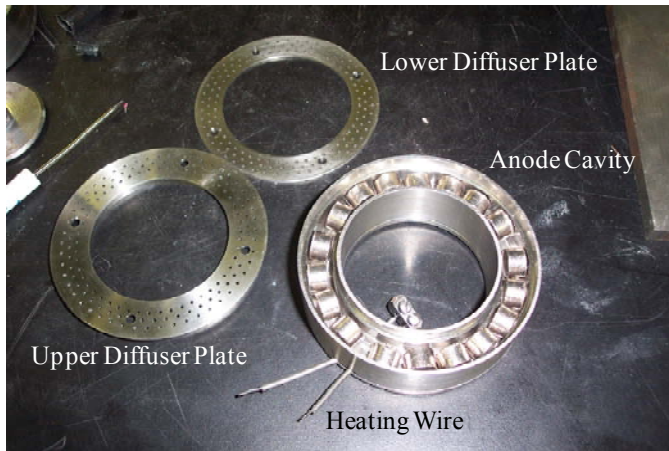


**Figure 30: Bismuth boiler with additional stainless steel diffuser plates**

The diffuser plates were successful in containing the bismuth sputtering but as testing continued it was becoming clear that this heating scheme had an unfortunate liability: although the system was quite robust, it was not very efficient and unevenly conducted heat. As an example, during one test, with a power input of 380 Watts the bottom heater pressure plate had a temperature of 1086°C whereas the top vaporizer plate was only at 713°C.

To solve this heat conduction problem, an identical anode cavity was fabricated out of pure copper which has a vastly higher thermal conductivity than stainless steel (385W/m-K vs 16.7W/m-K); the diffuser plates remained stainless steel. When heated with 490 Watts, the bottom heater pressure plate had a temperature of 1039°C while the top diffuser plate achieved 779°C. Although the temperature of the stainless steel heater pressure plate was near the melting point of copper, the anode itself remained essentially isothermal and about 400°C below the 1082°C melting point. The thermal performance of the copper anode was significantly better than the stainless steel but it was demonstrated that copper is not compatible with high temperature bismuth as the anode was fatally damaged on the first run. Figure 31 is a photo illustrating the damage.

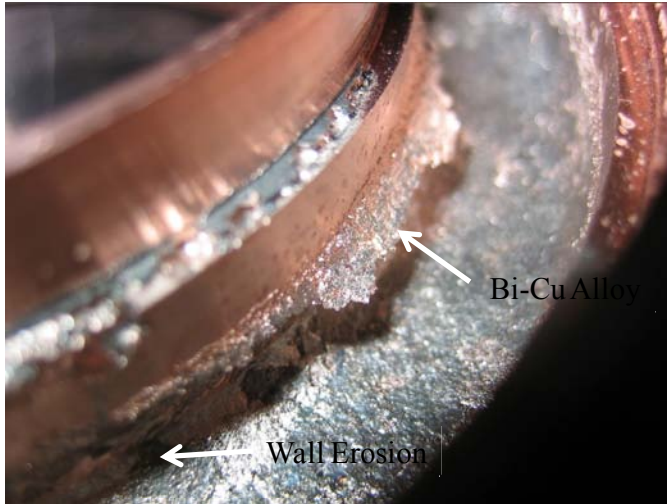
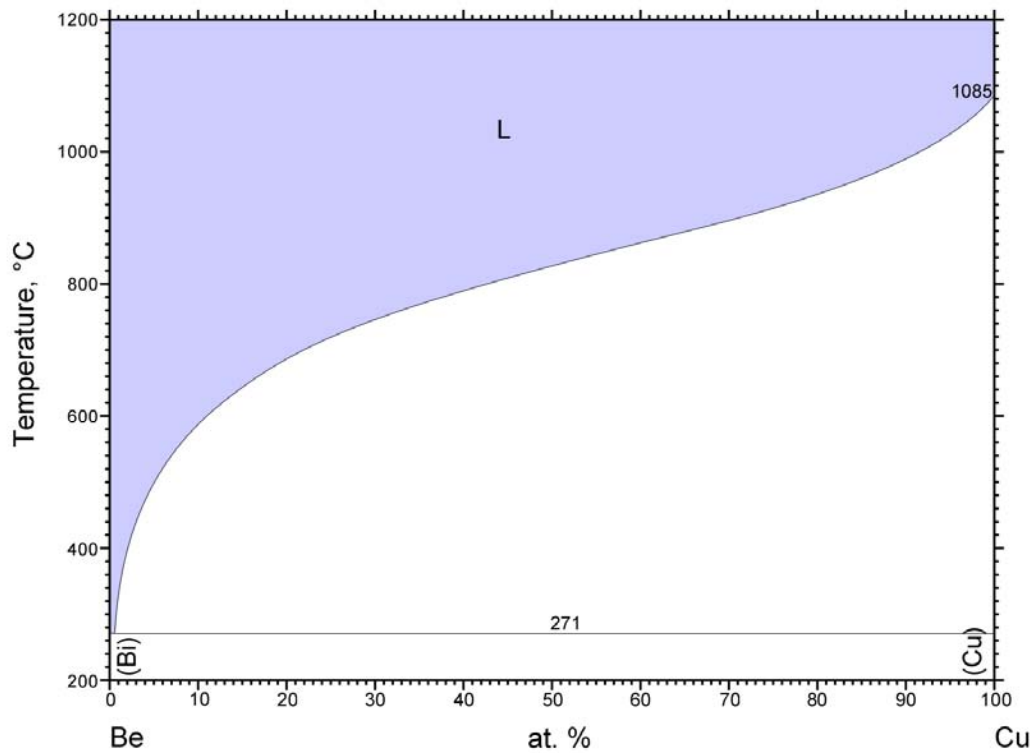


**Figure 31: Copper anode damaged by high temperature bismuth**

The side walls of the anode where the bismuth fill level was are clearly visible as is the shiny silvery overhang. Below that level, the copper was somehow eroded upwards of 1/16" leaving no trace as to where it went. What is not apparent in the photo or the initial inspection was how the bismuth actually flowed out of a hole which developed in the anode cavity which effectively ended the test. The solution to this problem turned out to be bismuth's ability to make alloys with other materials. Figure 32 is the bismuth-copper binary phase diagram. Phase diagrams of several other common engineering materials are included in Appendix A.



© ASM International 2006. Diagram No. 900432

**Figure 32: Bismuth-Copper phase diagram from Ref. [56]. According to the phase diagram, a copper substrate should not be expected to withstand molten bismuth. Reprinted with permission of ASM International®. All rights reserved. Permission letter can be found in Appendix D.**

A binary phase diagram is a graphical representation of what sort of phase (solid, liquid or gas) is to be expected in a solution of two elements whose relative concentration varies on the x-axis and temperature varies on the y-axis. On the left hand side of the plot is pure solid bismuth; a situation similar to the copper-bismuth boiler before heat was applied. As the temperature increases beyond the melting point of bismuth, a curve sloping upwards to the right indicates how much copper could be mixed with the bismuth and still have the solution remain a liquid. This has a very important implication, though, because it means that at any given copper-

bismuth interface, the bismuth can draw some of the pure copper into a solution. At this point, concentration gradients develop which seek to evenly distribute the copper in the bismuth solution and effectively remove the copper from the boiler walls. At the recorded anode temperature of 779°C an 80%/20% by mass bismuth and copper mix could certainly be present. In short, the bismuth was able to get a sufficient amount of copper in solution so as to create a hole in the bottom of the anode thus allowing the mixture to flow out of the test setup. From this point forward, before any material that was destined to be in direct contact with molten bismuth was used, its material compatibility was first verified on a binary phase diagram. As chance would have it, bismuth is rather incompatible with nearly every metal except refractory metals.

#### ***4.5 Porous Vaporizer Design and Extrusion Testing***

In Section 3.3, it was explained how in order for a porous vaporizer to function appropriately, bismuth must have a non-wetting contact angle on that vaporizer material otherwise liquid bismuth would pass through largely unaffected. Since contact angles are a synthesis of the properties of each of the constitute materials involved in the interface each configuration must be determined experimentally. To determine the contact angle of materials, a small piece of bismuth was placed on a substrate of the material under test. The substrate was heated resistively in a vacuum chamber and the results were photographed. Figure 33 is a composite image illustrating bismuth non-wetting contact angles on stainless steel, molybdenum and tungsten substrates. The wettability of a liquid on a substrate does have a temperature dependence so it was imperative to verify that bismuth remained non-wetting on each substrate throughout the expected operating regime.

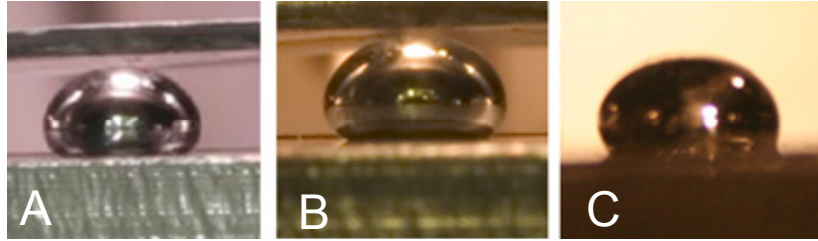


**Figure 33: Bismuth wetting tests on stainless steel (A), molybdenum (B) and tungsten (C) substrates.**

**In all cases the contact angle exceeds  $90^\circ$  therefore bismuth is non-wetting on these materials**

The wetting tests performed above demonstrated that stainless steel, molybdenum and tungsten were viable candidates for a porous vaporizer. However, stainless steel was initially chosen because it was commercially available and could be attached to the rest of the anode via conventional welding techniques.

To verify the assumption that a piece of porous material with a given average pore size behaves like a similarly configured array of capillaries a simple test was devised and is illustrated in Figure 34.

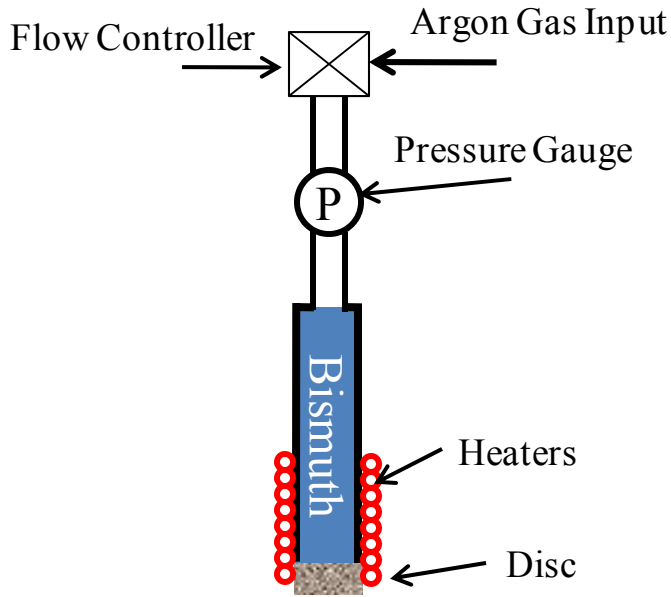


**Figure 34: Apparatus for testing bismuth extrusion pressures**

A stainless-steel porous disc was hermetically welded onto the bottom of a tube which served as the bismuth reservoir. Resistive heaters were wrapped around the tube so the temperature of the tube could be varied. To control the pressure with which the liquid bismuth was impinging upon the porous plate an argon gas feed line was connected to the top of the tube. The applied gas pressure was then increased until liquid bismuth was observed to be flowing through the porous plate. The results of testing two different pore sizes are shown in Table 8. Although not included in the table, the temperature of the porous plate was varied from 300°C to 1000°C with no conclusive trend in measured extrusion pressures indicating thermal effects do not appear to be a significant factor.

Table 8: Pressures estimated and required for bismuth extrusion through a porous plate			
Manufacturer Specified Pore Size	Estimated Extrusion Pressure	Actual Extrusion Pressure	Effective Pore Size
0.5 $\mu\text{m}$	1,006 kPa	254 kPa	1.98 $\mu\text{m}$
10 $\mu\text{m}$	50.3	23 kPa	22 $\mu\text{m}$

From these results several conclusions can be made. First, bismuth extrusion will initiate at the largest pore in the interface. A scanning electron micrograph of a commercially supplied plate of 10- $\mu\text{m}$  porous stainless steel, which shows the ambiguity of the pore size definition, is shown in Figure 35. Due to the kinetics of sintering, the pore size is a statistical distribution rather than a fixed value, this will be detailed more in Section 5.3.1. Second, results dictate that care must be taken to ensure the hydrostatic pressure of the bismuth does not approach the extrusion threshold pressure as the hydrostatic pressure on the bottom of the anode face will increase by 0.96 kPa for every centimeter of bismuth contained above. Third, the capillary approximation does indeed provide a satisfactory estimate of extrusion pressure with the caveat that the largest pore in the plate will determine when extrusion begins.

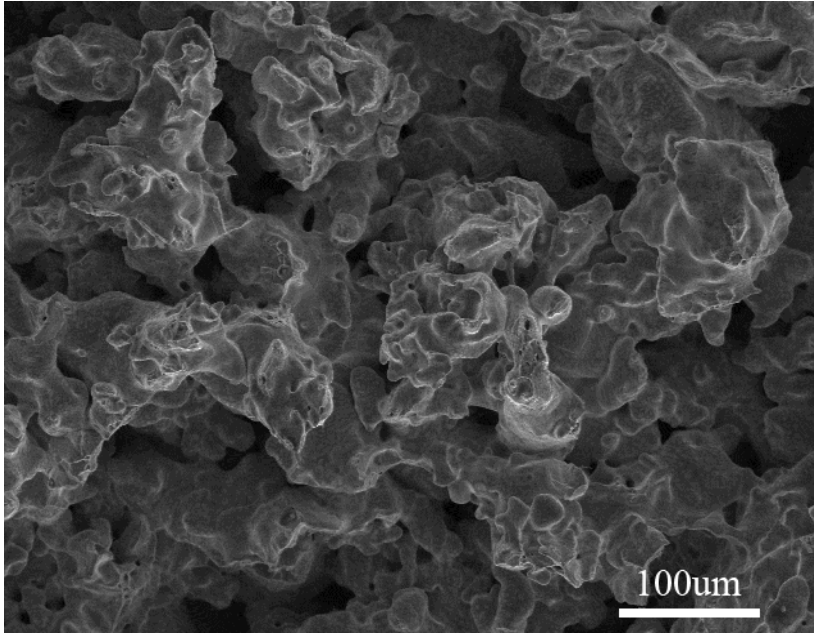


**Figure 35: A high-magnification SEM image of a commercially purchased 10 µm average pore size porous stainless steel plate**

#### ***4.6 Mixed Xenon-Bismuth Operation***

The xenon testing done in Section 4.3 made it clear that using segmented anodes for thermal control is a viable method as it works well and does not negatively impact thruster performance. With the validity of the shim anode thermal control established, and bismuth boiler development done in Section 4.4 verified that evaporation of bismuth was possible at reasonable temperature, the next move was to attempt to demonstrate the direct evaporation concept. This section will discuss how the anode and thruster evolved.

Integrating a resistive heater to provide the initial temperatures required bismuth evaporation would have required substantial modifications to the thruster which were deemed unnecessary at the time. Instead, a unique dual-propellant anode was designed for bismuth development and testing. The anode was designed to accommodate gaseous xenon and liquid

bismuth simultaneously. The ability to run on xenon allows the thruster to achieve the high temperatures required for bismuth evaporation without the need for resistive heating. Figure 36 is an illustration of the anode cross section. Xenon is fed into the lower chamber where it then flows out the gas diffuser holes. Bismuth is contained in a separate chamber and is delivered to the anode via a hydrostatic reservoir external to the thruster.

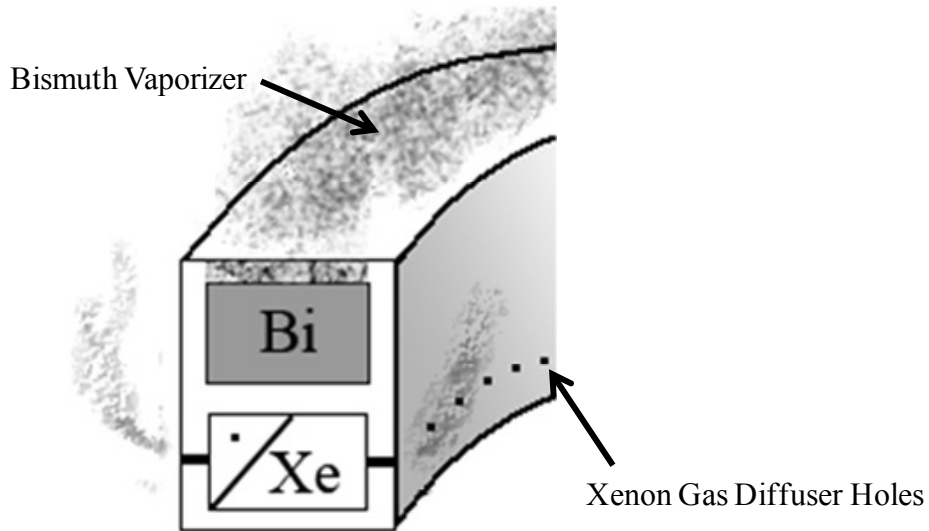


**Figure 36: Dual propellant anode cross-section**

The porous stainless-steel plates for the vaporizer were available from Mott Corp in a variety of thicknesses and average pore sizes. The first functioning thruster ran with a 2.54-mm-thick porous vaporizer with a 10 $\mu$ m average pore size. Figure 37 is an SEM image of the 10 $\mu$ m porous plate. The thickness was selected to match the wall thickness and the 10 $\mu$ m pore size was selected because it gave a good overall balance between the open area fraction (43%) and empirically determined bismuth liquid extrusion pressure.

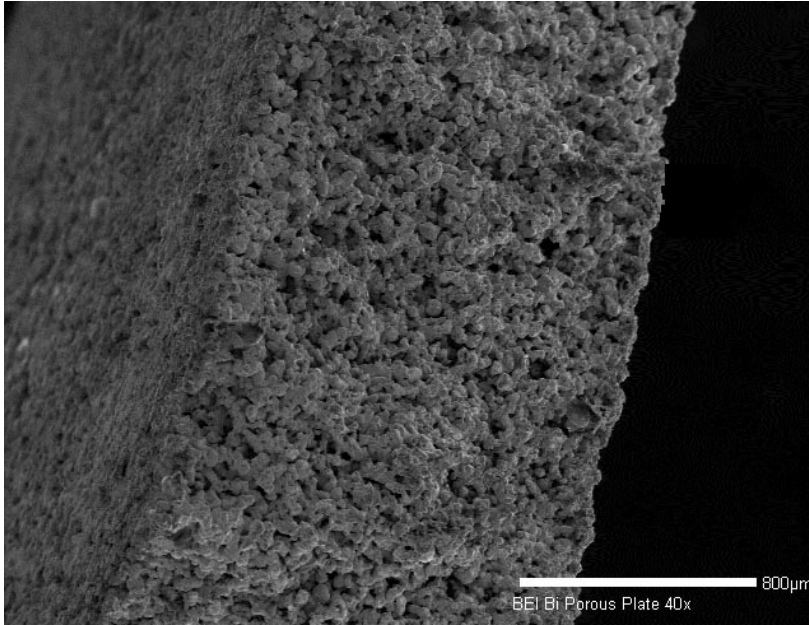


**Figure 37: SEM image of the 2.54 mm thick porous stainless steel plate**

The first successful xenon-jumpstarted bismuth Hall thruster test took place on May 6<sup>th</sup> 2005. The thruster was first run for nearly thirty minutes at 2.2kW on 35 to 50 SCCM of xenon before any evidence of bismuth flow was observed. These observations took the form of an increase in the discharge current, which is indicative of a higher mass flow rate. The xenon flow rate was slowly decreased to compensate for added presence of bismuth but the overall power of the thruster continued to increase. Eventually xenon flow was completely terminated but to sustain the flow of bismuth, the thruster power was increased to 400 V and 16 A (6.4 kW). This power level far exceeded the 2 kW design envelope but nonetheless demonstrated the feasibility of the direct evaporation concept. Figure 38 is a frame taken from a video that was shot during the first direct evaporation bismuth test and since the entire thruster is glowing, it is quite clear that the thruster is running very hot. In this particular case, the thruster was pointed upwards to prevent the minor leaks that had developed in the porous vaporizer from spilling bismuth into the discharge chamber.



**Figure 38: Frame from a video taken during the first direct evaporation bismuth test**

During this initial test, it was verified that the shim anodes could divert discharge current from the main anode but at these power levels, the plasma made quick work of the stainless steel shim anode – more specifically the inner shim anode. Figure 39 is a photo taken after completion of the bismuth test. The inner shim anode actually melted and fell into the main anode while still somewhat liquid, causing it to stick to the porous vaporizer (Figure 39 left). Post-test calculations show that self-sustaining operation required an anode power density approximately  $2.5\text{W}/\text{mm}^2$ . However, this number is quite misleading since the actual area of the functioning porous vaporizer was certainly much smaller due to the very crude TIG weld that attached the porous vaporizer to the anode body (Figure 39 right).



**Figure 39: Dual propellant anode with an inner shim melted to it after testing (left) and a photo of the porous vaporizer after testing showing the crude TIG weld (right)**

The previous anode was intended to be more of a proof-of-concept device rather than one that was reusable. Taking what was learned from the previous xenon-bismuth tests a new and improved anode was fabricated. To further ease the power density requirements, the anode face area was reduced by an additional 10% with the porous vaporizer outer diameter now at 89 mm and the inner diameter at 74 mm. The lower part of the anode, the xenon gas distributor, was forced to remain at the previous larger ID and OD to allow for propellant lines to enter the anode. To alleviate cracking that developed during welding, the anode body and stainless porous plate were sent out to be rotary TIG welded in a vacuum environment, which lead to a vastly superior weld and minimal damage to the vaporizer pore structure. Figure 40 is a photo of the finished result.



**Figure 40: Photo of a dual propellant anode with further reduced face area and a vacuum rotary TIG welded porous plate**

With a new anode installed and the inner shim replaced the thruster was again “jump-started” on xenon. Operation commenced with 40 SCCM of xenon at 400 volts and 4.42 Amps. As the bismuth reservoir heated up, the discharge current once again began to slowly increase – indicating bismuth evaporation. The current was allowed to rise until reaching about 8 Amps. By this time, current was increasing at a rate of approximately 1-2 Amps per minute so xenon mass flow was reduced to keep the current in an 8 to 10 Amp window. Eventually all of the xenon gas flow was removed and the power supplies were reconfigured to run in current-limited mode. If the discharge current began to drop (indicating evaporation was slowing), the supply automatically increased voltage to maintain the current. The increased voltage subsequently increased the power deposition to the main anode, which in turn increased the bismuth evaporation rate. The bismuth thruster ran for approximately 45 minutes in a completely self-sustaining mode before being voluntarily extinguished. When the thruster was running at 4kW and 12 Amps on bismuth (no xenon except cathode flow), the facility pressure was  $8.5 \times 10^{-6}$  Torr. A thermocouple on the back of the anode indicated a reservoir temperature of  $756^{\circ}\text{C}$ . Figure 41 is a photo during bismuth only operation.

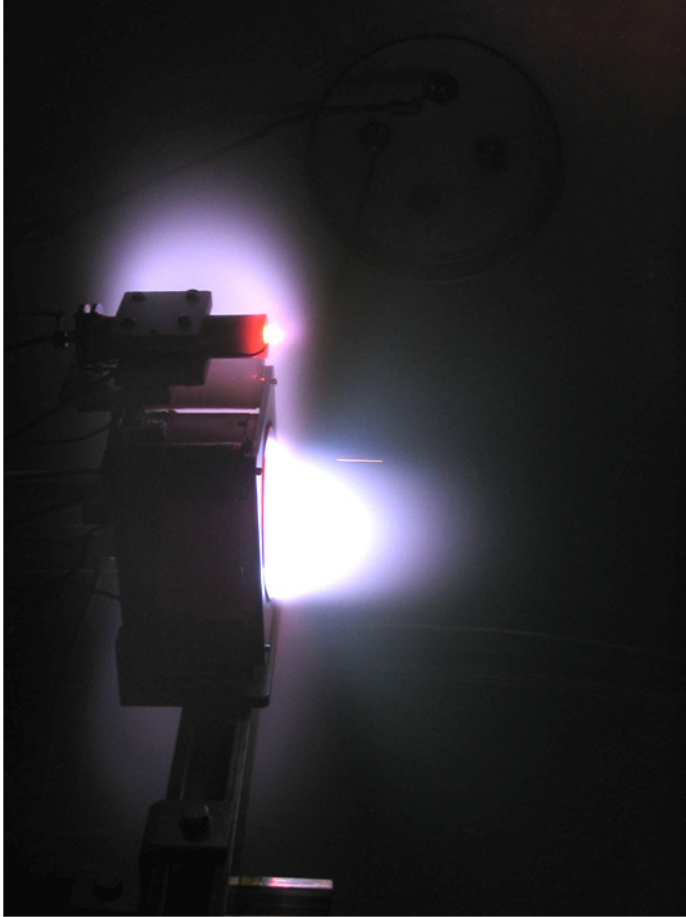


**Figure 41 - Bismuth Hall thruster running at 4kW**

“Jump-starting” the thruster on xenon has proven to be a very effective way of initiating bismuth mass flow. Although the direct evaporation scheme is inherently unstable (high power induces high evaporation which induces even higher power), the slow instability time renders manual control possible. Figure 42 is a plot of a manually controlled transition from xenon to bismuth.

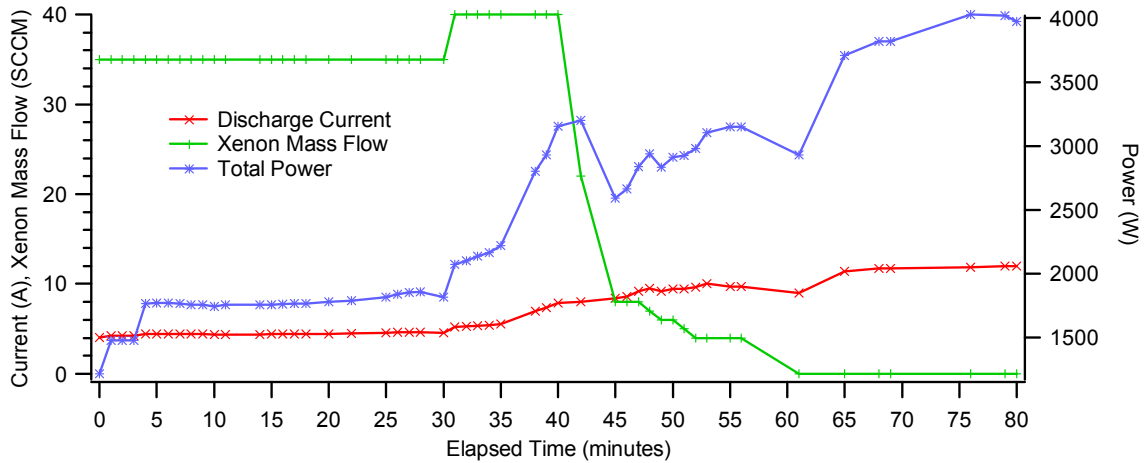


**Figure 42 - Current, power and xenon flow during a transition. Discharge voltage was initially held at 400 volts until xenon flow was removed and the discharge was held at a constant current.**

#### ***4.7 Molybdenum Shim Anodes***

From mixed xenon-bismuth testing experience, the inner shim anode has proven time and time again to be the first part that melts. Logically, since the stainless steel anodes were melting, moving to a refractory metal should solve the problem. The inner and outer shim anodes were fabricated out of 99.95% pure molybdenum and were subsequently used during operation. Figure 6 is an image of a melted stainless steel shim anode (left) and the molybdenum shim anode (right). For several weeks during unrelated lower-power xenon-only performance testing, the

molybdenum anodes behaved exactly as their stainless steel counterparts did. \

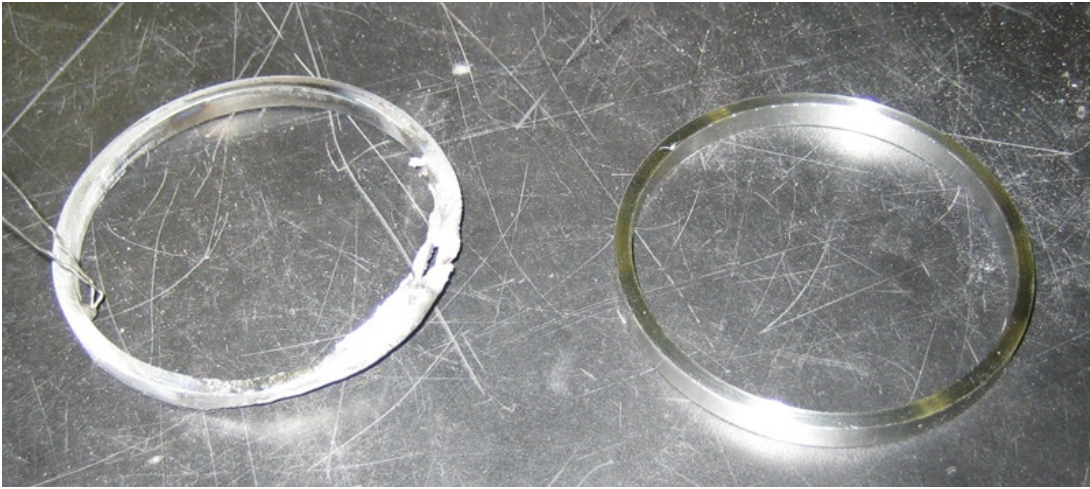


**Figure 43: Photo of a melted stainless steel shim anode (left) and a new molybdenum shim anode (right).**

Once xenon performance testing was complete, the thruster was disassembled to look for any damage that was incurred during testing. No significant erosion or traces of arcing were observed so the bismuth reservoir was loaded and the entire apparatus was moved into the bismuth tank. 32 attempts over a 50-day span were made to achieve self-sustaining bismuth operation using the xenon jump-start method. Thermocouples in various thruster locations revealed that the main anode reservoir was just not getting hot enough to cause significant evaporation. A variety of things too numerous to mention here were attempted to no avail. One thing was becoming clear: the inner shim anode seemed to be getting excessively hot. Unfortunately, the thermocouple that would usually be attached to the inner shim anode was removed citing reasons that it only adds to complexity and the molybdenum should never melt anyway. There was a widely held belief that perhaps power just needed to be further increased. By this time, 5kW operation was becoming quite standard and the inner shim anode would glow extremely bright. The inner shim anode was then electrically isolated which allowed it to float;

an act that should have relegated it to a non-participating part of the thruster. The result was quite the opposite as the inner shim anode now would get so hot and glow with such ferocious intensity, it would optically saturate any camera that was attempting to take a photograph.

At that point, it was clear the inner shim anode was not operating as it should for some unknown reason. All molybdenum was subsequently removed from the discharge chamber (both inner and outer shim anodes). With the anodes physically removed, the next two tests were able to successfully run on bismuth with relative ease.

#### ***4.8 Shim-less Operation***

With the molybdenum shim anodes removed, “jump-starting” the thruster became quite easy and routine again. Removing the shims also removed the ability to actively control anode temperature through electron current sharing – an aspect that was thought to be critical to stable operation. However, a surprising stability mechanism was discovered. When the thruster could maintain a self-sustaining discharge, the anode power supply was configured to supply a constant current while allowing the voltage to rise or fall to satisfy the current requirement. This type of open-loop current control displayed surprising stability, with the discharge voltage remaining constant within +/- 5V. Figure 44 is a representative plot of the voltage regulation.

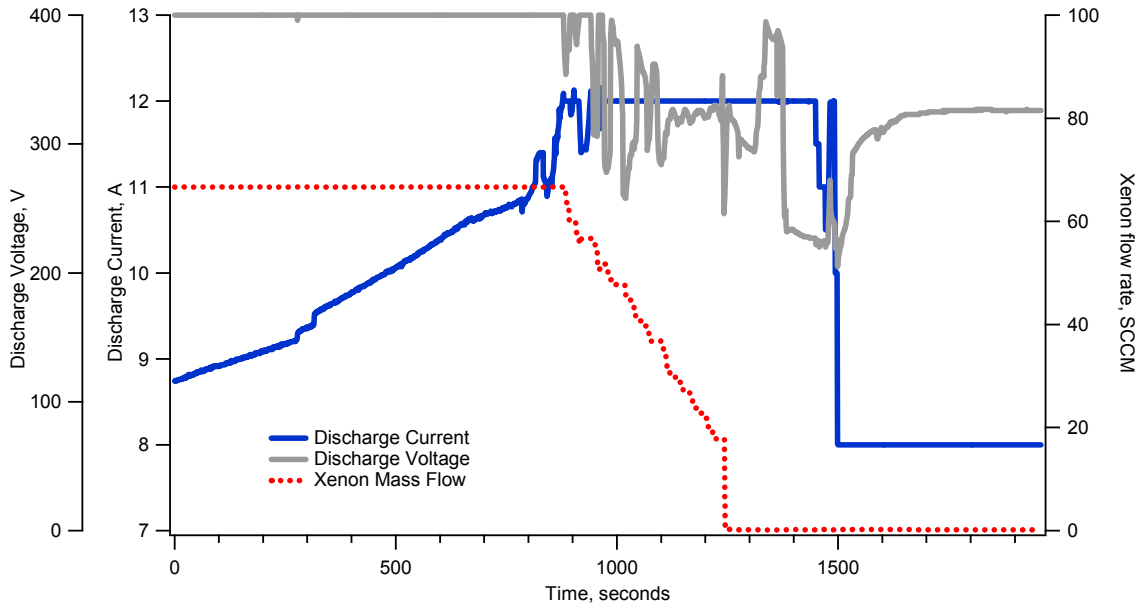


**Figure 44: Representative data showing xenon mass flow rate, discharge voltage and discharge current.**

In Figure 44, the xenon bismuth transition is clearly denoted by the steady rise in discharge current. The xenon flow is subsequently reduced until flow ceases completely. During the transition though, there are significant changes in voltage while current is held constant. After the transients decay, the current is reduced from 12 Amps to 8 Amps. Initially, the voltage decreases, but over the span of several minutes eventually settles to a steady value.

While the details of this unexpected and fortuitous stability are somewhat unknown, the physical mechanism can be understood qualitatively by analyzing the evaporation dynamics coupled with the I-V characteristic of a HET discharge. Consider the representative I-V behavior shown in Figure 45 for two different values of mass flow. For constant-current operation, if the mass flow increases, the discharge voltage necessarily decreases from  $V_2$  to  $V_1$  as the thruster transitions to the higher I-V curve. This decrease in voltage, with current constant, reduces the power deposited into the anode face and, hence, reduces the bismuth evaporation rate back

towards its initial lower value. The same stabilizing effect would happen for a decrease in mass flow – the overall power would increase and would tend to restore the mass flow to its design value. The effect is then to correct thermal excursions away from the thruster “set point,” which is determined through thermal design of the device and the geometry of the vaporizer. These effects are examined in more detail in Chapter 6.

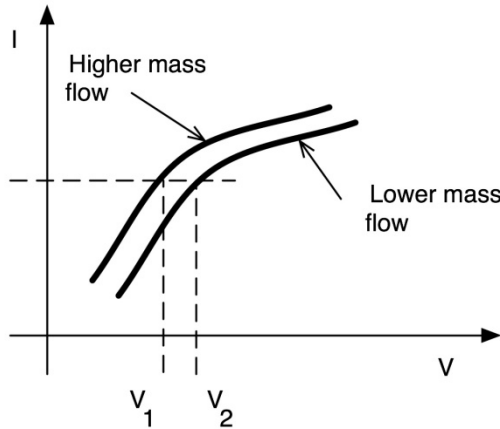


**Figure 45 I-V characteristics for typical HET at different mass flow rates illustrating how discharge voltage compensates for varying mass flows.**

This string of successful shim-less tests was eventually marred by vaporizer thermal problems that limited the repeatability and the duration of testing. The next section describes these thermal failures and what was done to reduce and eliminate them.

#### ***4.9 Vaporizer Thermal Failures***

From the results presented above, the dual propellant anode did indeed work albeit at very high temperatures. In an attempt to reduce the required anode face temperature the porous vaporizer was reduced in thickness to 1.58 mm. The underlying thought was that the 37.5% reduction in thickness would enhance heat transfer to the bismuth reducing the thermal

requirements. Using a simple thermal conduction model, it was estimated that by using a thinner plate, the temperature of the bismuth would increase by 39°C.

Subsequent tests were performed using the 1.58-mm 10- $\mu$ m stainless-steel porous vaporizer. Although the thruster required less initial power input to obtain a self-sustaining discharge, other problems became evident. Estimated mass flow rates were obtained by taking pre and post-test anode masses and early testing indicated that the mass flow rate was substantially lower than the design objective. To increase the mass flow rate, it was necessary to increase the operating power of the thruster to levels above 3.3kW. After the usual warm up period the discharge was initiated with early promising results. However, after only 10-20 minutes of self-sustaining operation bright spots would begin to appear on the vaporizer face. If the thruster was allowed to continue to run with the spots, certain parts of the anode would begin to cool off and the entire discharge would begin to attach to a specific region on the anode, typically the bottom portion. Figure 46 is a composite photo demonstrating normal operation and a vaporizer experiencing failure. On the upper portion of the vaporizer the plasma is so sparse that the glowing anode can be clearly seen whereas the bottom portion is completely obscured by a dense, bright plasma. Post-test inspection of the discharge chamber revealed that at some point during operation or cool-down liquid bismuth had penetrated the vaporizer and accumulated in the bottom of the discharge chamber.



**Figure 46: Views of the bismuth Hall thruster in operation. The left photos were taken looking directly into the discharge chamber and the right photos were taken at an angle to see the plume. Top – Bismuth thruster during normal operation. Bottom – bismuth thruster running with a porous vaporizer in the early stages of failure.**

The initial thought on this problem was that  $10\mu\text{m}$  was the *average* pore size therefore creating the possibility that a single larger pore could be allowing liquid to flow into the discharge chamber - much like in the extrusion pressure testing of Section 4.5. The application for porous stainless steel is usually filtering so after contacting the manufacturer it was reported that the

10 $\mu$ m media stops 99.9% of the 10 $\mu$ m particles. This fact created the distinct possibility that given the sheer number of pores involved there was going to be one pore that was substantially larger than the average.

The logical course of action taken was to obtain new porous material with a smaller pore size. The size selected was 0.5  $\mu$ m, which had an open area fraction of 27% and an extrusion threshold pressure of 1 MPa. The reduction in open area meant that the porous vaporizer would have to run about 50°C hotter than the previous 10  $\mu$ m anodes but since no damage to the anode was visible, it was deemed to not be an issue. Plate thicknesses of 0.0625" and 0.125" were installed on several anodes and tested sequentially. As expected, the measured operating temperature of the porous vaporizer increased from the 750°C range to the 800°C range. The 0.5- $\mu$ m anodes were able to operate substantially longer than the 10  $\mu$ m anodes, on the order of several hours, but eventually would fall victim to the same failure mechanism: a series of bright spots would develop and eventually force the early end of a test.

After the bismuth leakage phenomena occurred several times it was clear that an underlying physical process was changing the structure of the vaporizer since in the configuration tested, it was hydrostatically unlikely for bismuth to leak through a 0.5 $\mu$ m pore. After some amount of investigation it was concluded that the elevated temperatures required for higher mass flow rates were actually causing the vaporizer to continue to sinter which can certainly occur well below the melting point of the bulk material (see Section 5.3.1 for an explanation of sintering). Ordinarily sintering would result in a continued reduction of pore size but the drastically uneven hydrostatic pressure created by the bismuth may have been causing the pore structure to change. Undoubtedly some pores shrunk as expected but others were enlarged which eventually led to the tiny bright spots that, if left unchecked, would grow into a hole. The only recourse to fix this

problem was to move to more thermally durable materials. Section 5.3 details the fabrication of porous molybdenum.

#### ***4.10 Resistive Pre-Heating***

The xenon-bismuth “jump-start” was a very viable method of initiating bismuth evaporation but it carries with it the added complexity of integrating an additional flow control system. The resistive heating knowledge gained from both the bismuth boiler experiments as well as unrelated high temperature cathode development in the Isp Lab, prompted a reexamination of how the bismuth flow was being initiated.

One of the primary concerns with resistive heating was how to have the heater integrated in such a way that it remained electrically isolated and yet thermally connected to the anode. Commercially available tantalum-sheathed, magnesium-oxide insulated wire used in cathodes provided this capability but in practice it was very difficult to implement due to the brittle nature of the wire and bend radius limitations. Other types of ceramic-clad heaters were investigated but were later ruled out for reasons ranging from incompatibly large footprints to excessive expense.

The boron-nitride body that held the anode in place had a significant amount of room behind the anode that was previously used for mechanical attachment of the anode but the mechanical attachment was no longer required in the new design. A custom tungsten wire boron-nitride insulated heater was designed and integrated into the void. A two part boron-nitride insulator was designed to isolate the tungsten heaters from the anode yet still provide good thermal conductivity. Figure 47 is a cross section of the relevant parts of the resistive heating system and Figure 48 is a photo of the upper and lower boron-nitride insulators.

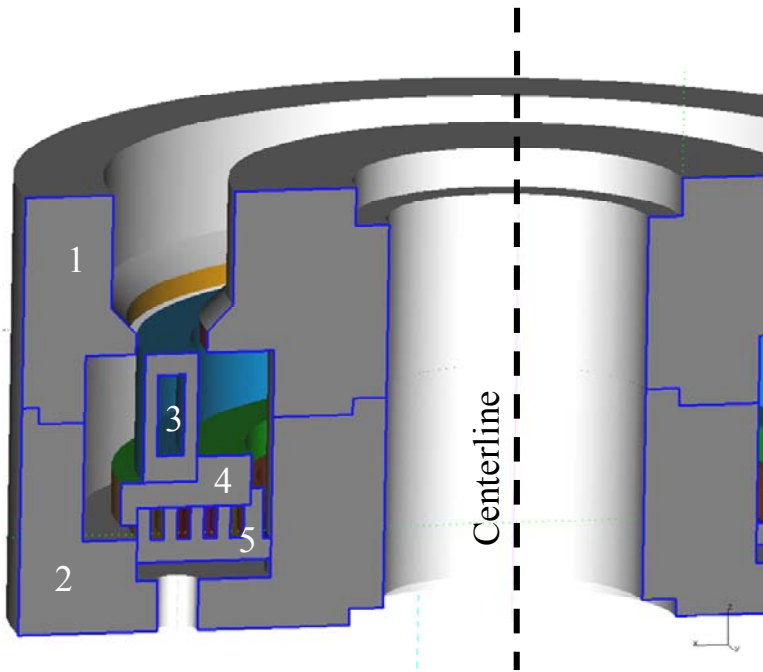


Figure 47: Cross section of the integrated resistive heater with the following parts: 1) upper boron-nitride body part, 2) lower boron-nitride body part, 3) anode, 4) upper boron-nitride insulator and 5) lower boron-nitride insulator with grooves for the rhenium doped tungsten wire.



Figure 48: Photo of the boron-nitride heater insulators. Left is the lower part, right is the upper part.

The boron-nitride insulator for the rhenium-doped tungsten heating wire has proven to be a very reliable system. The anode isolation provided by the boron-nitride allows for an inexpensive AC arc welder to be used as the heater power supply. The heater can run from 23-36 Amps at a voltage of 22-40 Volts (500-1400 Watts) with no degradation in performance. The only liability of the heating system is the eventual embrittlement of the tungsten wire. Although the rhenium doping decreases the loss in ductility of the wire after repeated use, eventually the wire becomes so brittle it breaks under modest stress which requires the wire to be replaced.

In addition to the main anode heater, an additional Nextel insulated tungsten heater can be wrapped around the outside of the boron-nitride body. The aptly named “Body Heater” allows for additional heat to be applied to the thruster body in effect counteracting some of the radiation and conduction losses through the boron-nitride body. When 10 Amps are passed through the body heater, the additional 300 Watts help to increase the anode temperature if the main anode heater cannot achieve the temperature necessary for ignition.

#### ***4.11 Bismuth Propellant Flow***

To accommodate the resistive heater an opportunity to optimize the flow of bismuth in the thruster came about. Gas fed anodes are exclusively fed propellant from the back of the anode. This design allows for mechanical stability as well as minimizes intrusion of parts into the discharge chamber. Figure 49 is a photo of a typical xenon anode showing the propellant lines exiting out of the back of the anode.



**Figure 49: Typical xenon anode with gas being fed from the rear**

One of the many challenging aspects of using bismuth as a propellant is working around the 3.3% expansion upon freezing. To that end, it is important to have a way to load the anode with bismuth as well as empty it when testing is complete. Failure to do so may cause critical damage to the porous vaporizer. To minimize the chances of this happening, the bismuth flows through the anode in a unique way. Initially, the configuration in Figure 50(a) was used and the bismuth anode was designed in a similar way which allowed for the anode to be run on both xenon and bismuth (see Section 4.6 for more details). This design carried with it the liability that after shutdown, the bismuth remained in the anode. To minimize the effects of the freezing expansion, an additional ring of porous stainless steel was placed inside of the anode. The thought was that since the face of the anode is free to radiate into space, it would cool first forming a frozen interface that would work backwards away from the porous vaporizer. As the

solidification continued, the pressure building would eventually exceed the extrusion threshold pressure of that additional porous ring allowing for some liquid to occupy space it ordinarily wouldn't be able to, thereby relieving some of the pressure. This expansion prevention scheme seemed to work sufficiently but the large moment created by hanging the rather heavy bismuth reservoir made anode alignment difficult.

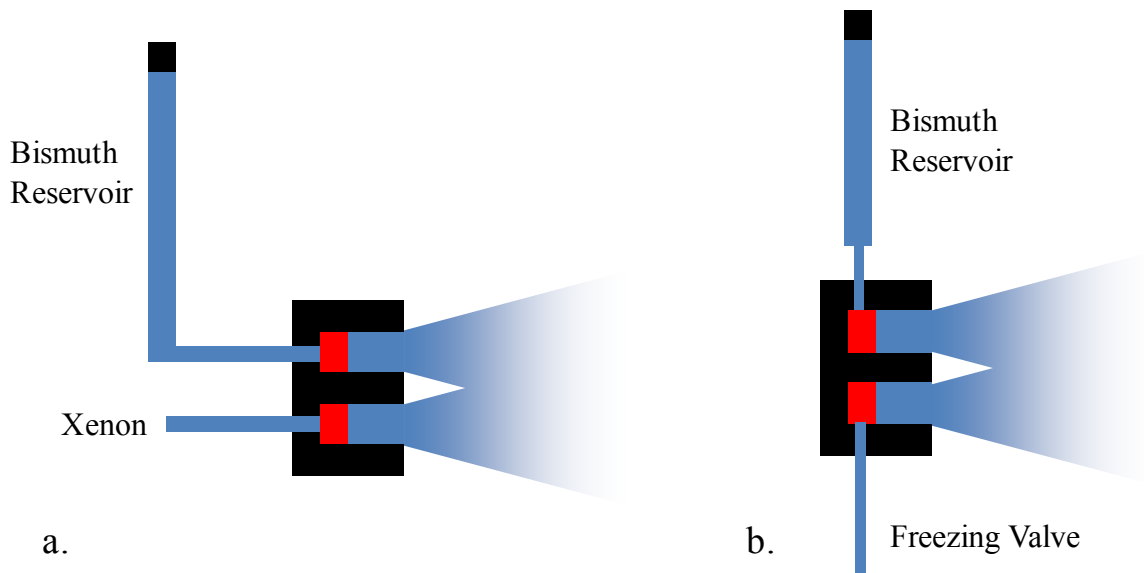


**Figure 50 Bismuth anode configurations: a) traditional rear-fed style and b) vertically fed**

The solution to the problem was to create a novel anode that had the bismuth entering from the top which is illustrated in Figure 50(b). This meant though that the typically monolithic boron-nitride discharge chamber would have to be separable, introducing the additional risk of anode arcing to supporting grounded structures. These risks were reduced by introducing a 2-mm dovetail where the junction occurs. Initially there was only an inlet for bismuth but eventually an additional propellant line was added to the bottom of the anode. The function of the bottom propellant line was to act as a freezing valve which enabled the anode to be drained when testing

was complete. The freezing valve was simply an extension of propellant line that was long enough to be sufficiently cool near the bottom so as to ensure that any bismuth present there was in the solid phase. To drain the anode, external resistive heaters only had to melt the bottom slug of bismuth at which point the contents of the reservoir and anode would empty into a catch-can where it can subsequently be weighed.

#### ***4.12 Summary***

This chapter detailed much of the experimental investigation that went into the development of the direct evaporation bismuth Hall thruster. Initial efforts centered around inexpensive modeling efforts but the complexity and vast number of unknowns in the system necessitated that an extensive experimental aspect of the program rise to fruition. The end result was a mature heating platform that could easily and reliably achieve the temperatures required for bismuth operation. In addition, many practical problems involving propellant flow and heater instrumentation were also addressed. Unfortunately, this chapter also proved that stainless-steel is not an appropriate anode material – a liability which is addressed in detail in Chapter 5.

## **5. Fabrication of the Bismuth Hall Thruster**

Throughout the preceding chapters, the experimental discourse in the development of the bismuth Hall thruster has been documented. This chapter describes some of the unique fabrication techniques that have been attempted or implemented throughout the development process. The chapter begins with Section 5.1 with a closer look at the stainless-steel anodes that were initially used. Section 5.2 is a very brief look at the bismuth hydrostatic reservoir whose simplicity does not warrant much discussion. Section 5.3 though is a very extensive look at how the molybdenum anodes were fabricated beginning with an introduction to power metallurgy and a review of some previous refractory powder metallurgy. The section continues through the iterative process of porous vaporizer development until finally a vacuum hot press is used to produce superior results. Next, the bonding of the porous molybdenum to fully dense molybdenum is addressed and a diffusion bonding process is developed. Finally, electron beam welding of propellant line tube stubs proves to be exceptionally problematic so a monolithic anode is fabricated.

### ***5.1 Stainless-Steel Anodes***

Stainless steel was initially chosen as the material for the anodes owing to relative inexpense, machinability, availability and anode design legacy. It bears repeating that in order for the direct evaporation scheme to work with the porous vaporizer, bismuth must remain non-wetting at all expected temperatures on the porous material. Another important parameter to be considered is the pore thickness and size, which was detailed in Section 4.5.

Depending on the size, the stainless steel anode blanks (anode without a porous vaporizer attached), were fabricated from 3.5" or 4" solid 304 stainless steel rod using a traditional lathe

and a narrow grooving tool. The porous vaporizer was CNC milled. No cooling fluid was used on the porous material due to contamination concerns; a compressed air cooler was used instead.

Attaching the porous material to the anode blank proved to be a very challenging aspect of fabrication. Out of necessity, early efforts relied on a staff professional welder to manually TIG weld the parts together. If very carefully done, manual welding can produce acceptable results in the 0.5- $\mu\text{m}$  pore size, 0.125" thick porous material but the thinner 0.5 $\mu\text{m}$  and all of the 10 $\mu\text{m}$  material yielded sub-optimal and often non-functional results. The difficulty in welding porous stainless steel is that when it is heated with a welder, the pores tend to collapse and shrink away due to the heat. Thus, the striking of the arc can initiate at the wrong place and open up large holes, rendering the part useless.

To enhance the bonding process, the anode blanks and porous plate were sent out to a vendor to be rotary TIG welded. By placing the anode into a rotary fixture, a constant distance from the electrode tip to the porous/anode interface can be maintained. The welding was also done in a controlled atmosphere glove box. The combination of these two improvements yielded welds vastly superior to the manual welds.

As time progressed and anodes were destroyed, rotary TIG welding filled the bonding need until that particular vendor went out of business. Subsequent vendors advised against rotary TIG welding and instead suggested the much more elegant and precise electron beam welding process. As such, several anodes had the porous plate attached via electron beam welding. The very narrow electron beam was found to require two passes around the weld joint to ensure proper localized melting of the porous material to the stainless. Figure 51 is a side-by-side comparison of the two welding techniques.

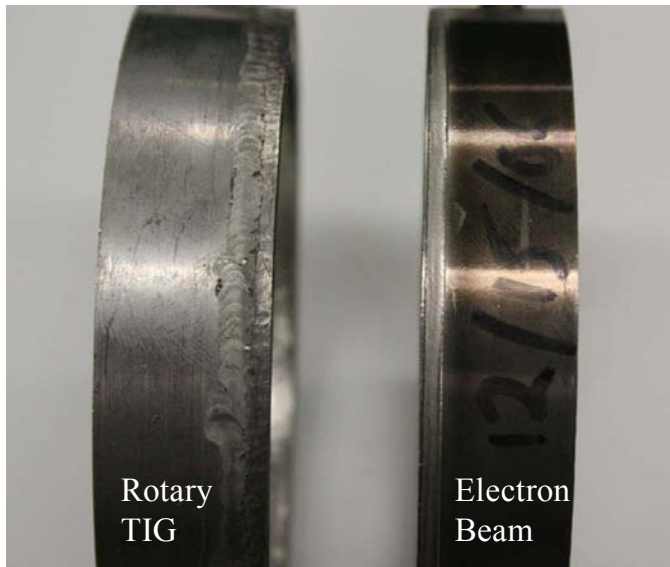


**Figure 51: Welded anodes, rotary TIG welding (left) and electron beam welding (right).**

Although the welding process was perfected, it was unfortunately welding a material that proved to not be thermally robust enough to meet the needs of the direct evaporation of bismuth. The fabrication of the replacement molybdenum anodes is covered in Section 5.3.

## ***5.2 Bismuth Hydrostatic Reservoir***

To ensure long-duration bismuth tests, the anode must be supplied with a constant flow of bismuth. There are many options available for supplying bismuth, but the simplest and most fool-proof way was selected. The reservoir consists of a tube of stainless steel with an inner diameter of 0.43” and an outer diameter of 0.50”. This sizing allows the tube to be welded to a Swagelok fitting and subsequently swaged onto the rest of the anode. With a 0.43” inner diameter, the reservoir can hold 9.18 grams of bismuth or about 30 minutes of run time per centimeter of the reservoir. To keep the hydrostatic forces on the anode to reasonable levels, the reservoir height is limited to 30 cm, which keeps the hydrostatic pressure at the bottom of the anode below 40 kPa.

### ***5.3 Molybdenum Anodes***

Molybdenum was chosen as the stainless-steel vaporizer material replacement. The 2623°C melting point was very attractive and the widespread availability and machinability of the material ensured this was indeed a practical choice. However, one drawback of using a refractory metal as opposed to titanium or an exotic steel alloy was the complete lack of a commercial supplier for the requisite 3.75" porous plate. Outside vendors were also probed to see if there was any interest in fabricating a large refractory porous plate but those inquiries were always met with polite rejection or a quote so impossibly high in price it would not be fiscally responsible to continue. Instead, it turned out MTU had the capabilities to fabricate the entire anode on campus so that was the route chosen.

#### **5.3.1 Introduction to Powder Metallurgy**

Broadly defined, powder metallurgy is creating solid objects out of powders. Powder metallurgy is very commonly used in the aerospace industry for its ability to reliably create complicated parts with controlled microstructures; a feat that metal casting cannot accomplish. Despite its name, powder metallurgy is not explicitly limited to metals as ceramics can certainly be processed in very similar ways.

In a typical powder metallurgy fabrication process the powder goes through several steps: preparation, compaction and sintering. The first step is to obviously prepare the powder. This is where any alloying powder or binders are mechanically blended in. The prepared powder is then moved on to the compaction stage where the powder is compacted via injection molding, extrusion or pressing creating a weak network of cold welds if the material is not malleable. The final stage of the process is sintering. This is where the material will gain strength and other favorable characteristics.

Sintering is the kinetic process by which two or more particles merge under temperature, pressure and time to form a single cohesive particle. Although there are no specific distinctions between the phases of sintering, some established guidelines exist which will indicate how far along in the process the sample is. Figure 52 is a graphical representation of the sintering process. In the first stage of sintering, the powder has simply been compacted. There will be some initial adhesion though the amount depends on compaction pressure and malleability of the material. After heat is applied, the contact points of the powder will begin to neck together. In this early stage, surface area still at least 50% of the initial value, grain sizes are smaller than particle diameters and the ratio of neck diameter to particle diameter is less than 0.3. During the intermediate sintering stage, densification reaches 70-92% and the grains begin to become larger than the original particle size. During the terminal stage, densification exceeds 92% and there is no longer any open porosity. Any pores that do exist are circular and isolated[57].

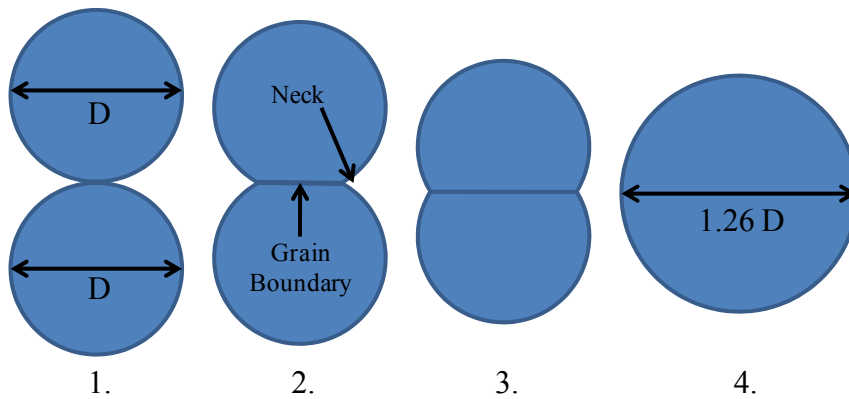


**Figure 52: Illustration of the two particle sintering process. 1) Two particles in contact, 2) during initial short sintering time neck growth has begun and created a grain boundary between the two particles, 3) during intermediate sintering time, neck growth continues and the grain boundary expands and 4) after an infinite amount of time, the terminal condition of two coalesced particles is reached.**

### 5.3.2 Previous Porous Tungsten and Molybdenum Efforts

Suffice it to say, there are very few applications where a porous refractory material is needed. Applications of porous materials typically include filtering and gas diffusion but these applications are almost always satisfied by lower melting point materials such as stainless-steel so there is little reason to have open porosity in a refractory metal. The general lack of porous applications is why refractory powder metallurgy is currently exclusively focused on reducing the porosity of the material to as near as zero as possible. That said, the fabrication of porous refractory discs is certainly not without precedent nor an application.

In the early 1960's NASA was working with liquid metal propellants, namely cesium, for use in ion engines. The thermal requirements of the system dictated that an 1100°C vaporizer operating temperature was to be expected and even higher temperatures would be required for more efficient ionization. Tungsten was chosen as material of choice because the work function of tungsten exceeds the ionization potential of cesium which creates the possibility of contact ionization, further enhancing the efficiency of the ion thruster[49, 58-60].

In the efforts put forth by NASA tungsten powders with average diameters of 1, 10 and 20 microns were isostatically compacted at 58,000 psi and sintered at 2250°F, 2500°F, 2750°F and 2900°F for 20 hours. The relative densities with respect to full densities, subsequently defined as porosity, were calculated for each case. A 2% by mass addition of stearic acid was found to greatly enhance the strength of the green press (un-heated compacted powder) thus reducing the chance the part would break before it was sintered. The net outcome of their efforts showed the most favorable results for a 1µm powder that was cold-compacted at 25,000 psi. This led to the most durable green press which was then heated for 20 hours at an arbitrary 2750°F. In short, beyond a certain temperature and pressure, the results were essentially unchanged, so the

least stressful condition was selected. For all test cases, though, the finished porous tungsten disc was rather fragile[59]; a situation that was not unique to tungsten.

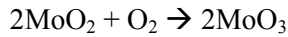
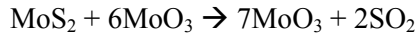
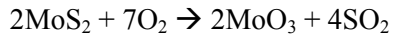
The former Soviet Union was also developing similar techniques around the same time as NASA though the technical details are not surprisingly more difficult to come by. Nonetheless, the Soviet efforts were directed towards a similar goal of developing a high temperature vaporizer for use in space propulsion systems. The Soviets also conducted some additional material analysis which provided some insight into the universal brittleness of sintered refractory metals[61].

### **5.3.3 Initial Porous Vaporizer Fabrication Efforts**

Using the NASA and Soviet refractory powder metallurgy experience from the 1960's and 1970's as guidelines, fabrication of a porous molybdenum vaporizer began. Molybdenum was chosen over tungsten for two reasons: first, the lower melting point of molybdenum implies that it is possible to sinter at substantially lower temperatures than tungsten. Since the designed operating temperature of the thruster is in the sub-1000°C temperature range, there was little justification for tungsten from a thermal durability standpoint. Secondly, at some point the porous vaporizer plate would have to be bonded to the rest of the anode to make a completed part. Molybdenum plate is vastly cheaper and easier to machine than tungsten.

Although all powder used in this document was purchased from commercial suppliers, following is a brief explanation of how molybdenum powder is made. Molybdenum is not found naturally in a pure state but rather in molybdenite,  $\text{MoS}_2$ . Molybdenite is extracted from mines either as a primary objective, as a by-product or a co-product with copper. To obtain pure molybdenum powder, the  $\text{MoS}_2$  is first crushed into a fine powder. The powder is then "roasted"

between 600 and 700°C in large multi-level furnaces to obtain MoO<sub>3</sub> via the chemical reaction listed below.



Once MoO<sub>3</sub> is obtained, it is possible to obtain the pure metal by reducing the MoO<sub>3</sub> with hydrogen and reducing the resultant MoO<sub>2</sub> again with hydrogen[62].

The powder compaction was done in a 3.75” cast iron die whose pressing interfaces were polished on a surface grinder to a mirror finish to ensure uniformity of the pressed plate. An acetone and zinc stearate mix was also applied to the die and ram before the addition of the powder to prevent the green press from sticking to the ram. As suggested in Ref[59], 2% by weight stearic acid was milled for 10 minutes in a Spex mill with the 1-5µm molybdenum powder. This stearic acid addition vastly increased the strength of the green press. In fact, without it the green press was so fragile it was nearly impossible to handle without breaking. The stearic acid harmlessly boils away at 383°C. Due to the very large size of the disc, the maximum pressing pressure that could be applied was 25,000 psi (172MPa) which corresponded to 276,000 lbs (125,000kg) on the ram. At this relatively modest pressure, the essentially non-malleable molybdenum powder will only weakly bond and will not achieve a density much above 60%[63]. However, that is the ideal situation for this particular application so 80 grams of molybdenum was usually pressed for two minutes, leading to a disc that is 3.75” in diameter, 1/16” thick and approximately 60% dense.

The pressing of the powder remained essentially unchanged throughout the development process but the same cannot be said for the method of applying the heat to sinter. The first attempt to sinter the molybdenum disc was performed in a reducing hydrogen atmosphere. The reducing hydrogen environment is ideal for sintering refractory metals for two reasons. First, the hydrogen will instantly react with any remaining oxygen in the furnace which obviously prevents oxidation of the part being sintered. Second, the small hydrogen atoms are able to penetrate into the sample and react with many impurities. Although this application does not require exceptional purity, it does create a very clean finished product[57]. Eight standard liters per minute of hydrogen is introduced to the furnace via controlled bleed valve. This flow creates a slight positive pressure which is maintained by a restrictive exhaust tube that also serves as a burn point for the hydrogen (the exhausted hydrogen is burned to ensure an untenable situation does not develop).

The hydrogen furnace used has an upper service temperature of 950°C which incidentally served as the set point which was maintained for 2 hours. However, the furnace used did not have a well defined hot zone so the sample was quite likely not at 950°C but rather lower. After cooling, the sample was still very brittle and it was apparent not a whole lot of sintering had occurred. To validate that assumption, the sample was taken to a Field Emission Scanning Electron Microscope (FESEM) for analysis. Figure 53 is a representative image of the sample. Several features of the image are relevant: the most obvious aspect is that the powder still has retained almost all of its initial character – still looks like powder. Second, the larger particles' facets can be seen which suggests that the larger particles are taking the brunt of the pressing force and are slightly deforming. This characteristic is very favorable for creating a stable porous material as the stresses induced at those particle interfaces should very readily sinter if the

appropriate temperature is achieved. Finally, there is no apparent oxidation present in the sintered sample (compare to Figure 57)

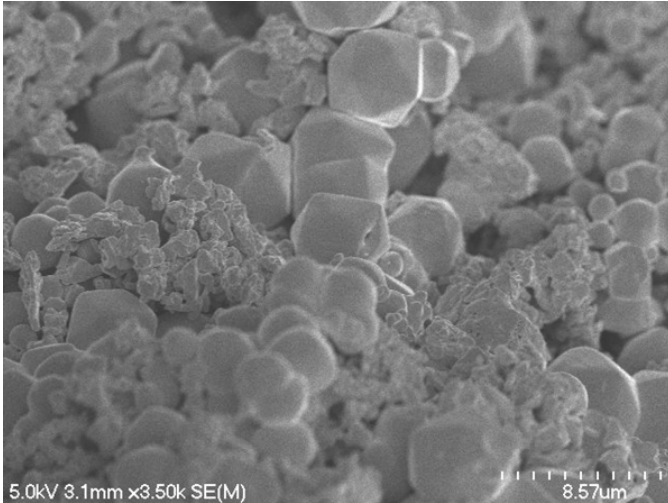


**Figure 53 – Molybdenum powder heated for 2 hours at 950°C in hydrogen environment showing little sintering**

After examining the hydrogen sintering results, it was clear that higher temperatures were required. To investigate what effect the temperature has on the results, several crude experiments were run. Heating up a large sample uniformly is difficult and fortunately unnecessary for these experiments. A small portion of a pressed disc was placed between two pieces of alumina silicate then wrapped with tungsten heating wire and instrumented with a thermocouple. This assembly was placed in a radiatively insulated coffee can which was then placed inside of a vacuum chamber. Once high vacuum was achieved, heat was applied to the system. Many different temperatures were tested and the level of sintering obviously increased with temperature. Figure 54 is an FESEM image of a sample sintered at 1200°C for 30 minutes in vacuum. Clearly this has produced a sample that is actually sintered as there is little individual particle character remaining.

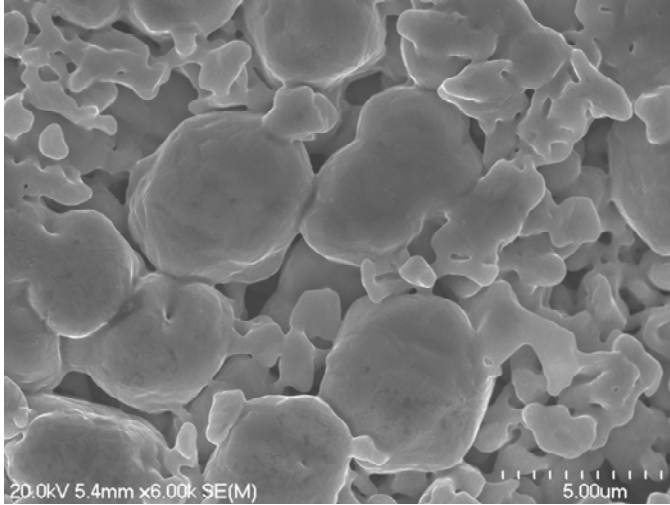


**Figure 54 – Molybdenum powder heated to 1200°C for 30 minutes in vacuum.**

The subsequent two attempts at fabrication are included only to serve as a warning to others. The system tested above worked great for samples under an inch or so in diameter but would not scale to fit the size required no matter how many different ways tungsten heater was wrapped around it and no matter how conventional oven burners were retrofitted and placed around it. So the next heat source used was an industrial heat treating furnace capable of heating samples to 1200°C in a large hot zone at atmospheric-pressure. A new molybdenum disc was placed into the furnace on a piece of alumina to prevent deformation when the stearic acid evaporated as well as to prevent the molybdenum from sticking to the furnace floor. Since 1200°C had exhibited excellent results in the vacuum experiments it was chosen as the set point for this furnace as well. The sample was heated overnight at the set point. When the door was opened the sample was nowhere to be found. Initial reactions of foul play were quickly tempered by a brief literature review: molybdenum forms  $\text{MoO}_2$  and  $\text{MoO}_3$  which are very volatile above 795°C[64, 65]. From this point forward, all sintering was performed under vacuum.

With the vacuum requirement established, the field of available heating methods was drastically reduced. The next idea involved using a vacuum induction furnace usually used for casting titanium or other metals that react with oxygen. A new disc was pressed and placed between two graphite plates which were intended to spread the heat more uniformly and to keep the disc flat. This assembly was placed on a 1/4" copper tube which was bent in a spiraling shape similar to an oven burner. The spiral configuration was chosen as it would give the most appropriate magnetic field for this application [66]. Under vacuum, the inductive heating system was brought to 5kW, which was required due to the low interaction of the small amount of molybdenum and the magnetic field. After 15 minutes of heating, the sample was glowing painfully bright and the disc was beginning to bulge in the center. After 20 minutes the heat had to be removed as there was growing concern the radiation from the molybdenum would melt the Lexan observation window and cause a vacuum breach. The resulting disc was in no condition to be used but did exhibit excellent mechanical strength and some porosity. Figure 55 is an FESEM image of the disc. There remains almost no evidence that the material began the day as a spherical powder. There was some promise though since the cross-hatch pattern does have porosity but the process was appropriately deemed to be far too chaotic to ever yield useable parts.

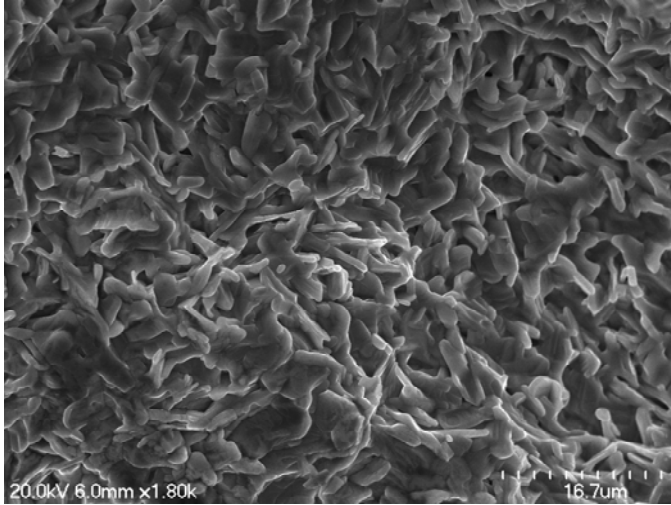


**Figure 55 – Molybdenum powder after 20 minutes in a vacuum induction furnace**

With most other options exhausted, the high temperature heat treating furnace was re-examined. There was some discussion that if an inert gas such as argon could be flowed into the furnace the oxygen would be displaced. Closer inspection of the furnace revealed that it only has four wires and a thermocouple running from the control system to the actual furnace. Since it was not possible to pull a vacuum on the furnace, the entire furnace was placed inside the Isp Lab's Bismuth Test Facility vacuum chamber (see Section 4.2 for details of the facility). The furnace's door safety switch was disabled and the furnace was integrated into the vacuum and electrical system so that the closed loop temperature controller could be kept outside to prevent damage to the electronics and to ease control of the furnace. The integrated furnace is shown in Figure 56 with a molybdenum disc ready to be sintered.



**Figure 56 - Heat treating furnace installed in the vacuum chamber**

Sintering in vacuum with the heat treating furnace proved to yield vastly superior results. The same process to establish the temperature which produced the best sintering results was repeated again. The temperature was not increased beyond 1100°C to prevent potential damage to the furnace. It was found that heating for 20 hours at 1100°C produced the most viable candidates.

Figure 57 is an FESEM image of an indicative sample. The image shows that the powder has all been fused together at some point since it shows little of its former character. The rough looking nature of the sample is actually due to molybdenum oxide forming at the vacuum pressures the heating was done at [67, 68]. There was not enough oxygen to cause damage but it did give a rougher, faceted appearance. Figure 31 shows the resulting porous molybdenum discs after being cut down to size on a 100,000 psi waterjet.

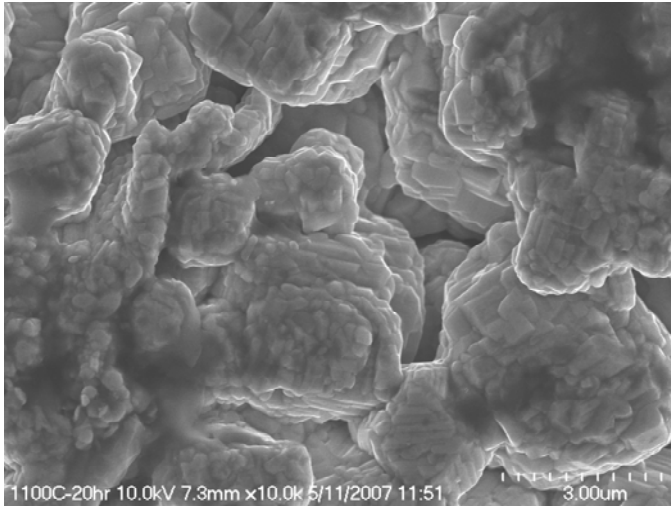


**Figure 57 – Molybdenum sintered for 20 hours at 1100°C under vacuum**



**Figure 58 - Completed porous vaporizer discs**

It should be noted that the finished discs were still very fragile and any clamping force applied would almost certainly break them, which would make any bonding process very unlikely

to succeed with the vaporizer face still intact. To increase the mechanical strength, it was necessary to move to a more advanced process.

### **5.3.4 Porous Mo Sintered in a Vacuum Hot Press**

In powder metallurgy, there are factors driving sintering: temperature, time and pressure. In all of the previous attempts no mechanism was available to apply anything other than a trivial pressure to the disc while heat was applied. However, a vacuum hot press became available in spring 2007 which significantly enhanced fabrication abilities. The hot press is capable of pressing 20,000 lbs onto samples up to 4" in diameter while heating to 1530°C in a vacuum or inert environment.

The ability to press while under high temperatures removed the need to add stearic acid to the molybdenum powder as well as pressing before heating thus stream lining the fabrication process. Since the cast iron die and ram previously used to press the sample wouldn't fit and would have likely melted in the hot press, it was replaced with a solid carbon ram and die. This increase in die diameter subsequently increased the amount molybdenum powder required to 125 grams.

#### **5.3.4.1 Porous Molybdenum-Carbon Bond**

The first attempt at pressing created some interesting results that although do not directly relate to porous vaporizer fabrication it is still an interesting offshoot of the project. Previously, zinc stearate was used to ensure that the molybdenum did not stick to the iron during pressing. Unfortunately zinc stearate melts at 120°C, has a flash point of 277°C and an auto-ignition temperature of 420°C which completely removes it from the list of useful substances to put into a hot press. On a whim, the molybdenum powder was placed in direct contact with the smooth

carbon rams. Due to a manufacturer wiring error, the hot press was running significantly hotter than was being reported. Upon later inspection, the pressing was done near 1334°C for 4 hours under a calibrated compaction pressure of 1,135 psi (7,835 kPa). When the ram and die were removed from the hot press and the disc was attempted to be separated from the carbon it became instantly clear that the molybdenum had very strongly bonded with the carbon. This is indeed what happened but what was fascinating was not only the enormous strength of the bond but also the very short bond length, or interaction area.

After the excess ram was brutally cut off with a reciprocating chop saw, the still intact sample was broken in half with a hammer and vice and a small shard was taken to the electron microscope for analysis. Although the carbon sandwiching effect was readily apparent to naked eye, the true scope of effect was even more apparent under the FESEM. Figure 32 is a low magnification FESEM image of the bond interfaces illustrating the molybdenum and carbon layers. It was a considerable surprise that the interfaces between the layers were perfectly straight and extremely well defined.

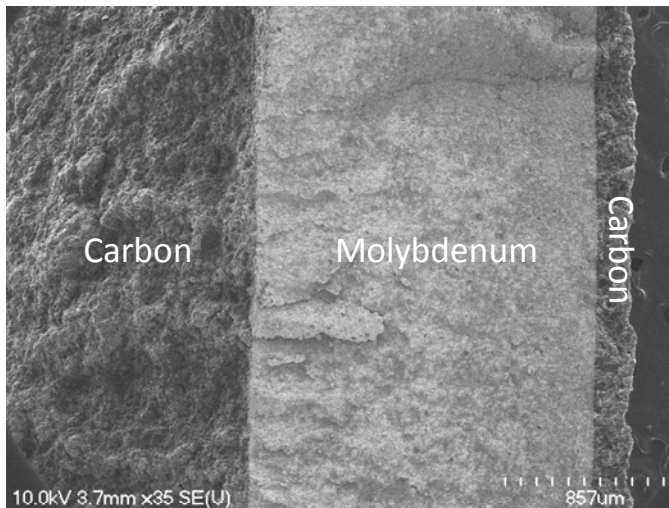


**Figure 59 - FESEM image of porous molybdenum bonded between layers of carbon**

To obtain a better understanding of the bond, the bond interface was subjected to X-ray mapping to identify the elements. X-ray mapping is done by using a scanning electron microscope and an Energy Dispersive X-ray Spectrometer (EDS) which is integrated into the electron microscope. An excellent description of X-ray analysis and EDS detectors may be found in Ref [69].

Figure 60 is a composite image of the porous molybdenum-carbon bond interface. On the left is a moderate magnification which clearly illustrates the porous nature of the molybdenum (top) and the 500-1000nm bond interface with the carbon. To investigate if there was a significant amount of diffusion of carbon or molybdenum across the bond interface, an X-ray map was made of the sample (right). As can be seen, a carbon-molybdenum mix exists on the boundary indicating that this is a diffusion bond.

As stated, the accidental bonding is not directly applicable to this research project but it does introduce the fact that it is quite easy to bond a porous refractory metal to carbon – the applications of which have yet to be determined.

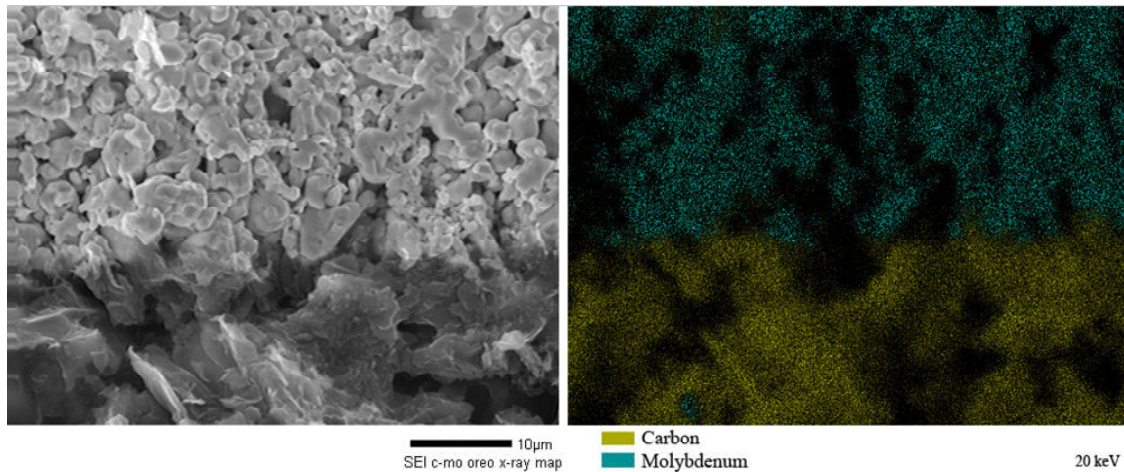


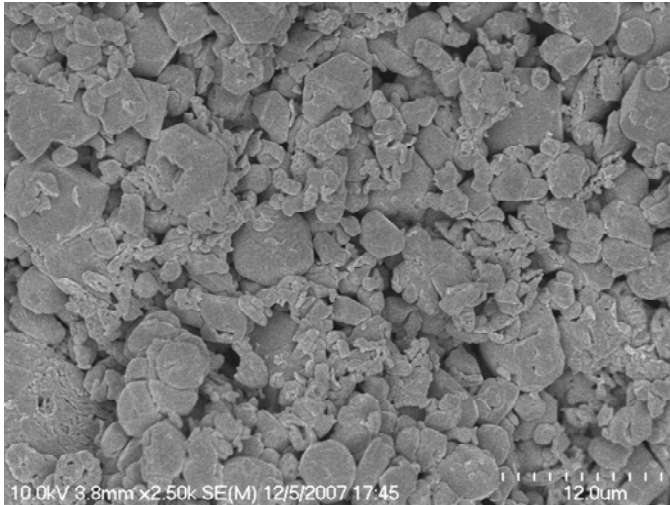
**Figure 60 - SEM image (left) and X-ray element map (right) of the porous molybdenum-carbon interface**

### **5.3.4.2 Final Porous Molybdenum Vaporizer**

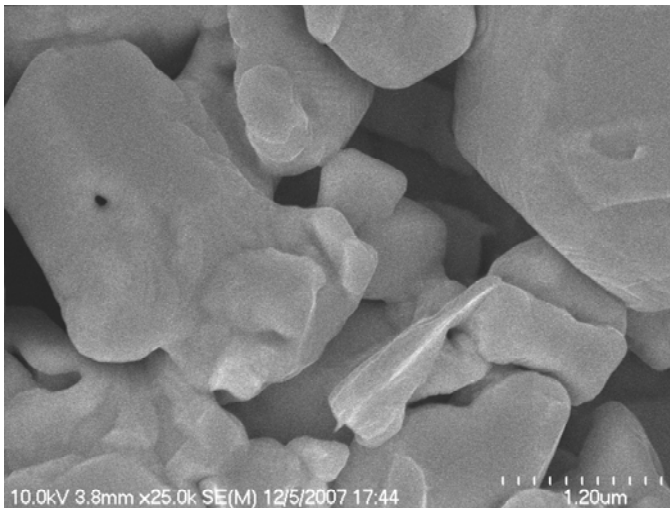
To prevent the rams from sticking to material pressed in a hot press, it is standard practice to coat the powder interface of the rams with an aerosol boron-nitride spray. This boron-nitride coating does stick to the molybdenum but is somewhat easily removed by using acetone in an ultra-sonic cleaner. Making strong porous molybdenum discs became quite easy with the hot press and since the results were adequate for the goal in mind, no attempts were made to further enhance strength or any other aspect. The end result is that 125 grams of molybdenum are pressed with 1000 psi and heated under pressure for 4 hours at 1100°C. The resulting 4” disc has a thickness of 0.1” and a measured density of 55.7%.

Figure 61 is a FESEM image of the porous plate showing some of the bulk features. The image is slightly deceptive looking in that it does not appear that the sample was sintered well. This phenomenon is due to the fact that the area imaged is actually in the bulk of a sample along a mechanically induced fracture which means it is actually an image of broken sinter bonds. Figure

62 clears this up by significantly zooming in on a region which then reveals a very mature sintered structure.



**Figure 61 - Low magnification FESEM image of a hot pressed porous molybdenum disc**



**Figure 62 - High magnification FESEM image of a hot pressed molybdenum disc showing favorable sintering**

### **5.3.5 Bonding the Porous Vaporizer to a Solid Mo Body**

Attaching the finished porous vaporizer face to the rest of the anode has always been a tricky and precise matter. Since electron beam welding worked quite well for attaching porous stainless to an anode blank it was prudent to attempt the same with the porous molybdenum. Unfortunately, the results were less than desirable. Significant cracking developed for reasons not understood. Traditional TIG welding was certainly not an option due to the inelegant nature of an arc weld.

With traditional options quickly exhausted, solid-phase welding, also known as diffusion bonding, was essentially the only option left. Diffusion bonding is certainly not a new process and in fact it is the only way to join metals to non-metals. This process works via a mechanism similar to sintering: atomic kinetic transport of material. When two dissimilar materials (with similar coefficients of thermal expansion) are placed together under heat and pressure, the atomic vacancies in each part will begin to allow material to slowly flow across the boundary. In fact, the porous molybdenum-carbon bonding accident from Section 5.3.4.1 is a perfect example of diffusion bonding. The two dissimilar materials managed to atomically “mix” enough that a stable interface was formed.

The same atomic “mixing” concept can certainly be applied to refractory metals of similar composition. However, the parameters required for a stable bond were not initially known and nothing in the literature made any suggestions. It was reasonable to assume that this process would take place near the same temperature and pressure that the original porous plate was created. To prepare the porous plate, a channel was milled on one side to ensure that the porous interface was flat and free of any residual boron-nitride mold release. However, the disc was not machined down to the requisite inner and outer dimensions due to the difficulties

associated with machining parts whose inner and outer diameter are very close. The unneeded porous material would be removed after bonding. The molybdenum anode blank was also prepared by enhancing the flatness of the interfacial surface on a lathe.

The porous disc was placed into the vacuum hot press first, with the machined surface facing upwards. The molybdenum anode blank was then placed in that groove and the second ram was installed. Several attempts at diffusion bonding were attempted before usable results were obtained. It was found that pressing at 1300 psi (the interface area is only 0.30 in<sup>2</sup>) and heating for two hours at 1100°C would produce some bonding. However, it was not strong enough to withstand the stresses induced on the bond when the remaining porous material was trimmed off using a lathe. Throughout the development, the opportunity to place a diffusion bonded sample in the electron microscope presented itself. Figure 63 is an SEM image of the diffusion bond interface. The full density molybdenum is mixed into the porous molybdenum over an approximately 10µm bond zone.

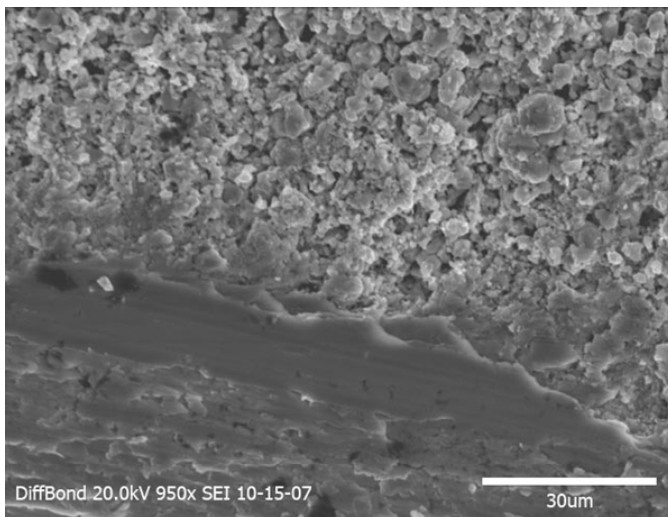


**Figure 63 - A SEM image of a diffusion bond. Porous molybdenum (top) is bonded to full density molybdenum (bottom).**

Successful and sturdy bonding was finally achieved by using a pressure of 3,330 psi (22.75 kPa), a temperature of 1200°C and a hold time of 2.5 hours. The resulting piece was trimmed up on the lathe and finished product is shown in Figure 64.

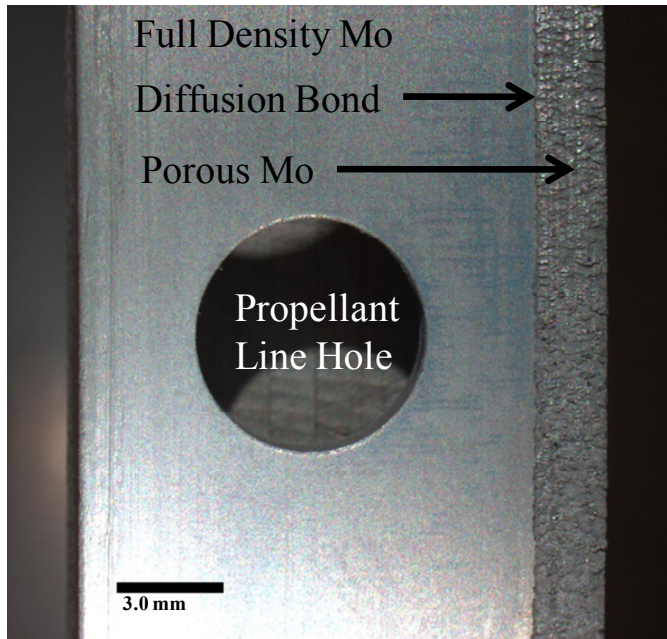


**Figure 64: Edge-on photo of a completed molybdenum anode with diffusion bonded porous face**

### **5.3.6 Integrating Bismuth Reservoir with Mo Anode**

After the porous diffuser plate was attached to the molybdenum body, the final step was to attach the bismuth reservoir and drain tubes. Tube attachment was done as the last step due to space constraints inside of the vacuum hot press. A vain attempt at welding the tubes in place with a TIG welder was made but rapid oxidation of the molybdenum created large cracks. After a new anode was fabricated, the anode and propellant tubes were then sent out to be professionally electron beam welded. As the name suggests, electron beam welding relies upon a very intense energetic beam of electrons which can be focused precisely and directed around the weld area. The power density possible with electron beam welding allows one to locally melt/weld very

small areas without affecting nearby material. This was a very important advantage as the diffusion bond between the porous and solid Mo would likely not respond well to the large thermal gradients created by less elegant methods of welding. Figure 65 is a photo of the completed anode illustrating one of the propellant lines and the diffusion bonded porous plate.



**Figure 65: Completed anode with diffusion bonded porous plate and electron beam welded propellant tube**

However, refractory metal welding problems became quite evident after several thermal cycles of the newly fabricated anode. The extreme temperatures required for the welding of molybdenum have the tendency to create very large grains in the weld region creating a brittle, unstable weld[70]. As the part is repeatedly heated and cooled, the large grains begin to merge with the bulk grains; a process that eventually will lead to cracking and in this case leaks. Initially the cracks were not sufficiently large enough to allow for bismuth flow (a 30 $\mu$ m or less crack will not permit liquid bismuth to flow under normal hydrostatic conditions) but eventually the cracks exceeded that threshold creating a slow leak around the weld joint. One such crack is shown in Figure 66.

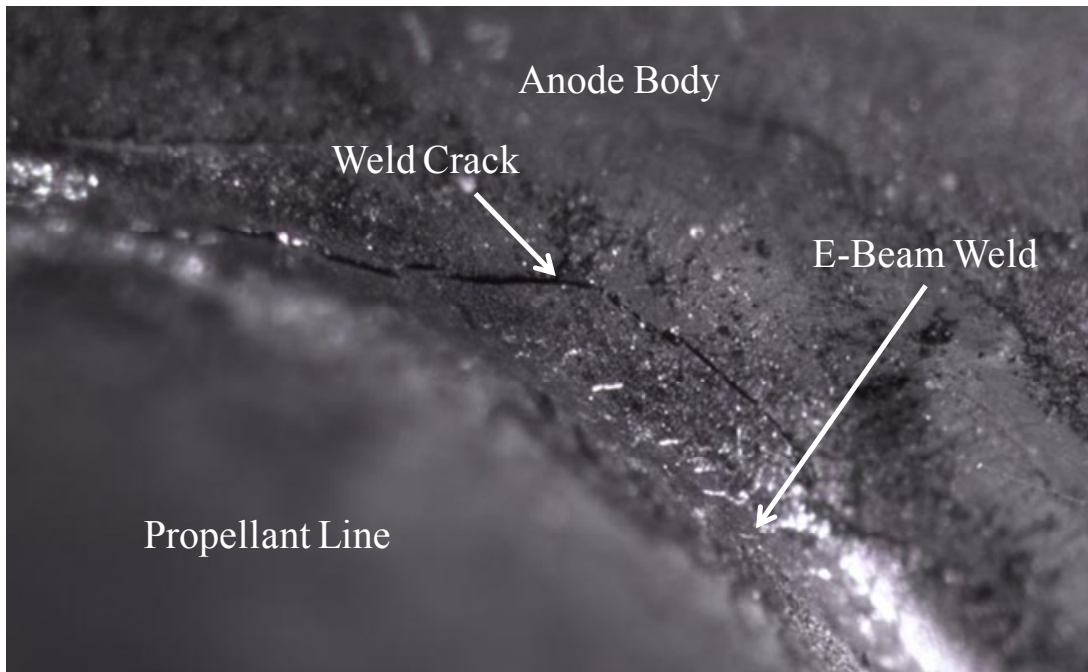


**Figure 66: Crack in the propellant line weld**

The liquid that escaped through the cracks caused several problems. If there was sufficient flow, the very hot liquid would burn through insulation in the freezing valve exposing the underlying propellant line which was at anode potential. This would rapidly arc to ground and if energetic enough would open a large hole in the line effectively ending the test. If the bismuth leaked out the top of the anode, it would tend to rapidly evaporate creating a gas jet in the region of the bismuth reservoir which was at anode potential. In this case, significant arcing events between the reservoir and the grounded magnetic circuit would ensue.

### **5.3.7 Monolithic Molybdenum Anode**

The welding of the tube stubs into the molybdenum anode was proving to be a very unreliable process. With the success of the diffusion bonding process it was a natural conclusion that a similar process may work for bonding the propellant tube stubs and the anode body

together. However, several issues prevented that from occurring. First, designing a fixture to perfectly align the tube stub interface and the hole is a daunting task. The high temperatures involved mean that any fixture would have to be fabricated out of carbon or steel but no bolting would be permitted since the nut would almost certainly fuse to the bolt. Second, to obtain a diffusion bond, the materials essentially must be in atomic alignment. The curved nature of the anode makes realizing that requirement difficult at best. The vaporizer diffusion bond works because under the pressure of the press, the material deforms until it breaks or comes into contact. Which brings up the final problem: the thin walls of the molybdenum anode body would be unlikely to be able to withstand the force created by the tube stub being pressed into the junction.

The final solution seemed was to make the whole anode and tube assembly out of a single piece of molybdenum. The main concern with this design was the high aspect ratio hole that would have to be drilled to permit bismuth to flow in and out of the anode. However, via precision CNC machining, an anode assembly was successfully fabricated out of a single piece of molybdenum plate. Figure 67 is a photograph of the completed monolithic anode. It should be noted though that experimental results with this monolithic anode are not included in this dissertation and are the subject of future work.



**Figure 67: The completed monolithic molybdenum anode assembly**

### ***5.4 Summary***

This chapter covered in detail the practical considerations and construction of the porous vaporizer anode assembly. It was found that stainless steel was not thermally stable enough to withstand high temperature operation for an extended duration. This led to the development of a porous molybdenum anode. However, porous molybdenum was not commercially available so an extensive refractory metal powder metallurgy development process ensued. Conventional bonding of molybdenum proved exceptionally problematic so the final anode assembly makes extensive use of diffusion bonds. The electron beam weld for propellant line tube stubs also failed over time leading to the construction of an anode and tube stubs out of a single piece of molybdenum. No data on the performance of monolithic anode is contained within this dissertation.

## **6. Operation of the Bismuth Hall Thruster**

The previous chapters have been largely concerned with the concepts as well as development of the bismuth Hall thruster. In this chapter some of the operational characteristics will be examined. In Section , the general operational phases required for a bismuth thruster test will be detailed. In Section 6.1, the basic phases of a bismuth thruster test are explained as is some of the general operation theory. Section 6.2 will briefly examine some of the steady state open loop transients that occasionally occur. In Section 6.3, some very preliminary diagnostic data will be presented which verify that the thruster is indeed accelerating bismuth ions.

### ***6.1 Anatomy of a Bismuth Test***

The operation of the bismuth thruster can be broken down into four distinct phases: warm-up, ignition transients, steady state operation and cool down. Figure 68 is an example plot showing the relevant features of a typical bismuth thruster test. This section will examine some of the characteristics of each phase.

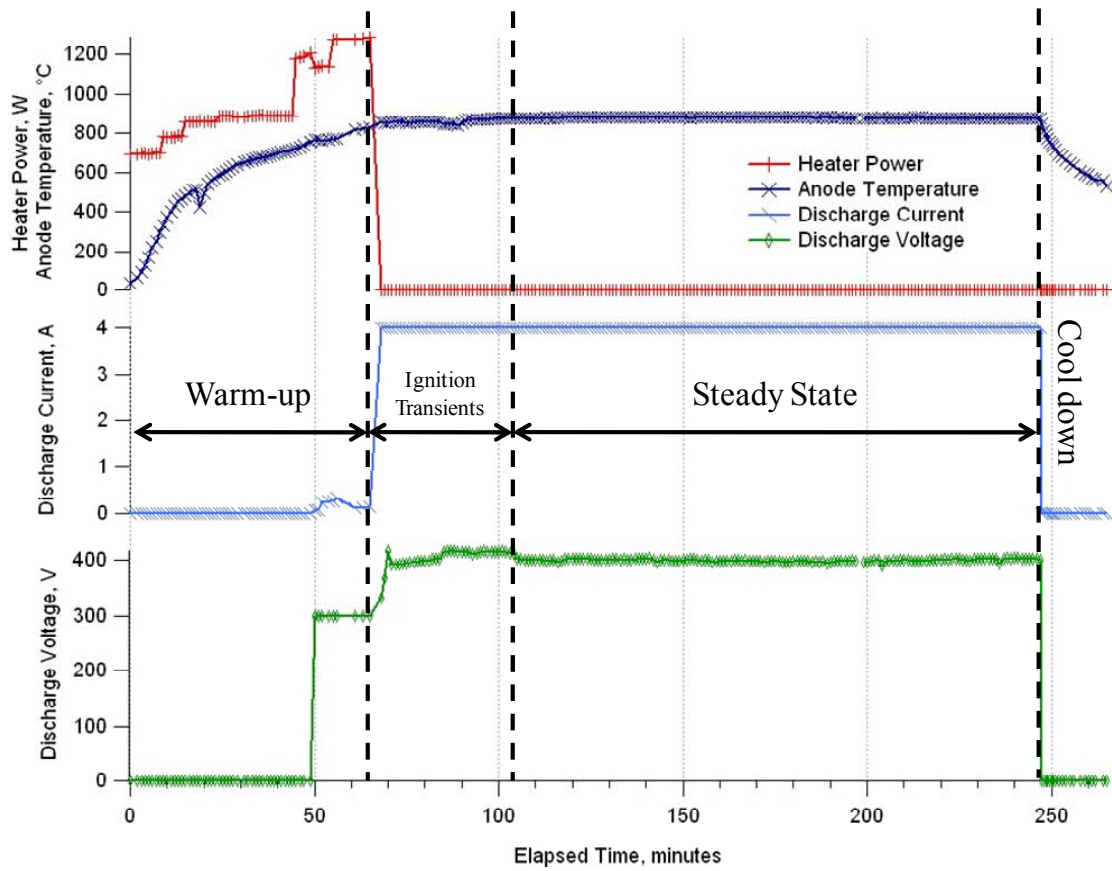


Figure 68: Example operational curve of a bismuth thruster test

### 6.1.1 Warm-up

The phase of operation is the “warm-up”. As the name suggests, the warm-up phase consists of the span of time where the thruster is brought from room temperature to a temperature suitable for ignition. To prevent unnecessarily large thermal transients and thermal shocks to the parts, the warm-up period typically spans an hour. This phase is relatively uneventful with the only anomaly being when the bismuth in the reservoir dumps into the anode. In Figure 68 this instant occurs approximately 20 minutes in and is denoted by a brief dip in the anode temperature. This is the relatively cool bismuth from the reservoir mixing with hotter bismuth in the anode.

### 6.1.2 Ignition Transients

The second phase of operation consists of the ignition transients. This period of time has no analog when compared to traditional xenon thrusters. To initiate ignition, voltage is applied to the anode with some magnetic field applied and the power supply placed into constant-current mode. The magnetic field is decreased until a glow discharge is established. During a glow discharge, the electrons have exceptional mobility and thus lead to a very significant electron current being shunted to the anode. While this not a good situation for a xenon thruster, it is ideal for the direct evaporation bismuth thruster. The diffuse and uniform nature of the glow discharge ensures that the electron current is attaching to the anode in a roughly uniform pattern. It is critical to note that this attached electron current is now *directly* heating the porous molybdenum face which is vastly more efficient than the ohmic heating from the rear that brought the anode to the temperature where this glow discharge was possible.

As the glow discharge continues to heat the anode face and drive up the evaporation rate, the resistive heaters are terminated. This has a drastic impact on the discharge voltage and electron mobility as a very large A/C solenoid was removed. Keep in mind though, the power supply is still set in a constant current mode so the discharge voltage will change to attempt to accommodate that current – so called “open-loop mode”. The discharge voltage will jump as the applied magnetic field, although weak, is not much more uniform and appropriate for electron confinement. Now begins a tricky balance between discharge voltage, current and magnetic field. With the resistive heaters now removed, the only mechanism for heat deposition is electrons impacting the anode and imparting their kinetic energy.

What is lacking from the above description is the impact that the discharge voltage has on the kinetic energy of the electrons. While the “leaked” electron current may be lower at higher

voltages, the imparted kinetic energy will be greater per electron and therefore may be able to compensate. In fact, it is exactly this situation that allows the direct evaporation bismuth thruster to generate thrust and yet self-heat. *Essentially there is an operational margin: how much power that would otherwise be used for thrust must be “leaked” to the anode via electrons to ensure a sufficient supply of propellant.* During the ignition transients phase, the magnetic field is eventually set to a level where a balance between thrust and discharge current (read propellant supply) is reached. There are some voltage oscillations likely do due with thermal masses of the anode face and bismuth but they decay over the span of an hour.

### **6.1.3 Steady State**

Steady state operation is largely uneventful. Discharge current is set to a constant value and the discharge voltage diligently stays near constant. In this static case, the electron current is depositing exactly the right amount of power to evaporate the bismuth at a rate that is exactly right to sustain that discharge current and voltage for *the applied magnetic field*. If magnetic field is changed, then so too will the discharge voltage, thrust and electron current. This is one of the most important aspects of steady state operation: it does not lend itself to optimization easily.

### **6.1.4 Cool down**

The cool down phase is very straight-forward. The discharge power is simply turned off and the anode instantly begins to cool. There was some early concern that bismuth evaporation would continue, but the temperature quickly drops below a point where bismuth has any significant vapor pressure. The resistive anode heater is typically turned back on to facilitate the freezing valve operation. After the freezing valve opens, all heat is removed.

## 6.2 Operational Transients

While open-loop control of the thruster ordinarily does not create many problems, occasionally there are some interesting transients that develop. Figure 69 shows a particularly interesting period of oscillation that began about 60 minutes into stable self-sustaining operation. The oscillation period was approximately 42 seconds with a peak-to-peak change in thrust of about 6 mN. Unfortunately a data acquisition fault did not permit operating voltage to be simultaneously recorded but the discharge voltage was oscillating from 328 Volts to 350 Volts in sync with the thrust oscillations. Cathode keeper voltage was also oscillating similarly. In this case the oscillations rose out of steady state operation initially with a small magnitude perturbation but after two cycles became quite significant. The oscillations continued for approximately 5 minutes where upon they quickly returned to a slight perturbation and then back to steady state – though at a higher power level.

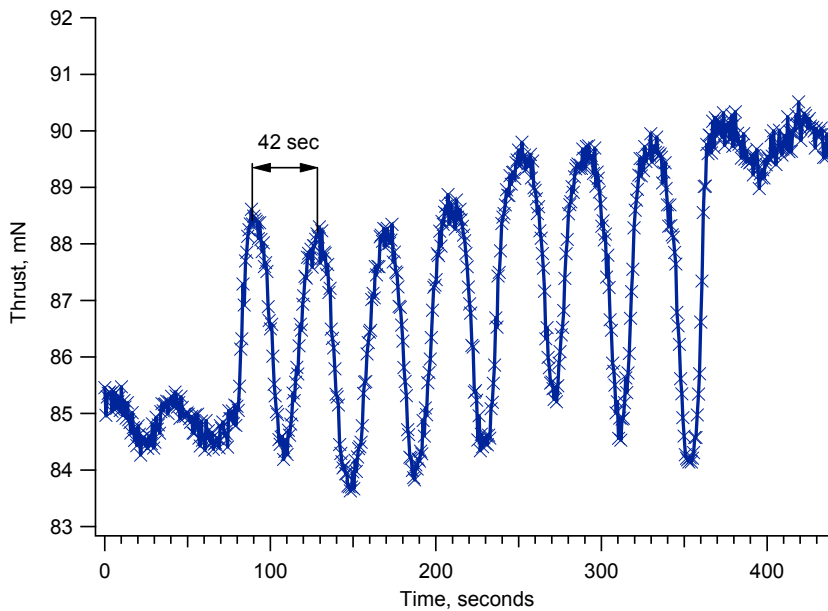


**Figure 69: Plot of thrust showing a transient oscillation with a 42 second period**

Although the cause of the oscillations in this select case is not known, the periodicity can be qualitatively explained by examining the heat flow through the vaporizer. As the discharge voltage changes, the kinetic energy of the electrons impacting the porous vaporizer changes as well. If for some reason there is a decrease in the discharge voltage, the electrons will be imparting less kinetic energy to the porous vaporizer that will cause a decrease in the face temperature. However, since the vaporizer has a finite thickness, specific heat and thermal conductivity, the change in temperature will take some amount of time to reach the bismuth-vaporizer interface where the actual evaporation is taking place. As the temperature decreases at the point of evaporation, the evaporation will slow, decreasing the mass flow rate. When the mass flow rate decreases, the discharge voltage will then increase to compensate. The increase discharge voltage then will impart more kinetic energy to the electrons impacting the porous vaporizer face which will then drive the face temperature higher. While it is not hard to see how this could give rise to an oscillating system, testing has shown that ordinarily there is some unknown damping factor that prevents this oscillation from growing.

Once in a period of oscillations, it is very easy to recover from them. For reasons explained in the previous section, any change in the magnetic field will result in the thruster changing to a completely different operating point.

### ***6.3 Preliminary Diagnostics***

In order to gain a complete picture of thruster performance and efficiency losses it is necessary perform comprehensive set of various diagnostics. While the goal of this thesis was to create a durable bismuth thruster platform and perform subsequent performance analysis and optimization, the development process revealed many unanticipated engineering challenges. Time constraints have limited the amount of performance characterization that has been

performed. Thus, an exhaustive suite of thruster diagnostics will be the subject of future work but there has been a significant amount of preliminary work which can serve as a baseline for future development. This section will cover some preliminary thermal performance, as well as plume divergence and ion energy analysis.

### **6.3.1 Thermal Imaging**

The temperature-dependent direct evaporation scheme has been thoroughly described in the previous sections. Although thermocouples are used to estimate the temperature of the anode, the harsh environment of the discharge chamber prevents attaching a thermocouple directly to the face of the anode. However, since evaporation rate is a function of temperature, it was important to establish whether or not bismuth was evaporating uniformly across the face of the anode. So to conduct a more complete thermal investigation of the thruster, a Mikron Infrared laboratory Model TH5104 thermal imaging camera was used. This camera has a thermoelectrically cooled mercury cadmium telluride (HgCdTe) 255x223 element linear detection array with a 21.5° x 21.5° standard field of view. In the low temperature operating range, the camera is sensitive from -10-200°C with an accuracy of +/- 1% of full scale. In the high temperature operating range, the camera is sensitive from 100-800°C again with an accuracy of +/- 1% of full scale. The traditional glass viewing window that was installed on the vacuum system did not transmit in the 3.0 to 5.3µm spectral range where the camera is sensitive. An optically transparent sapphire viewport with the spectral transmission characteristics shown in Figure 70 was installed to enable thermal imaging in vacuum.

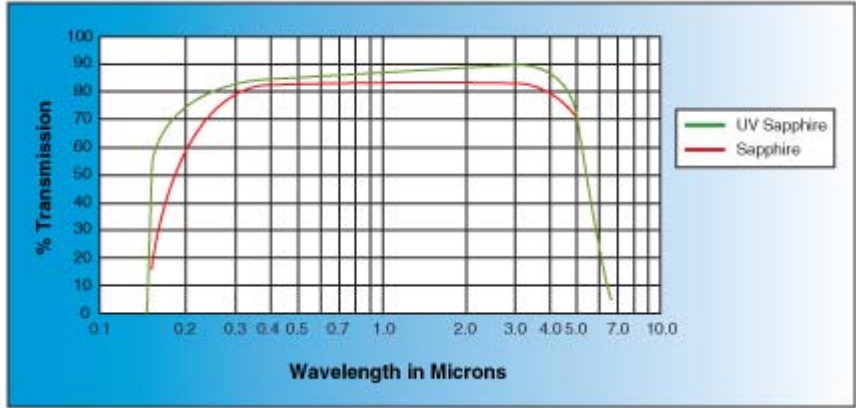


**Figure 70: Transmission characteristics of the sapphire window as provided by the vendor Kurt J. Lesker Co.**

Figure 71 is a thermal image of the face of the thruster immediately after shutting down from a three-hour steady state test. From the figure it can be seen that there is good thermal uniformity across the anode face. This suggests then that propellant was indeed flowing uniformly. Also of interest is that the constituent parts of the magnetic circuit are well below their Curie point so active cooling of the magnetic circuit will not be required.

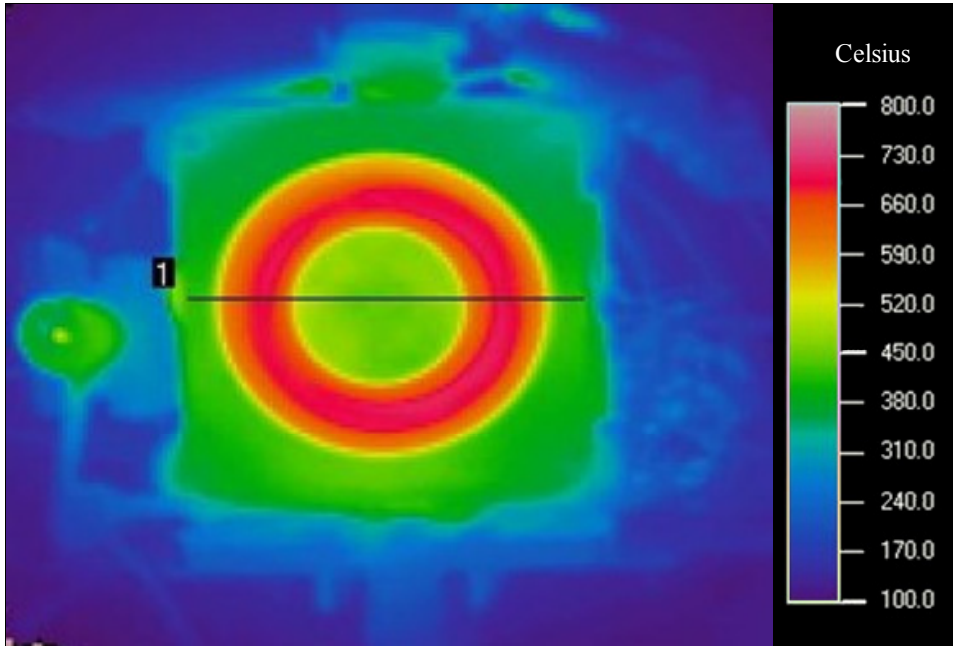


**Figure 71: Thermal image of the thruster after a three hour steady state run**

### **6.3.2 Plume Characterization**

There is much to be learned from examining the exhausted plume of a Hall thruster. Of particular interest is the beam divergence. Ideally, all exhausted ions would leave the thruster with a trajectory parallel to the thruster axis. In reality though, the ions pick up some amount of perpendicular motion as they exit the thruster. To obtain a measurement of this divergence, a Faraday probe is used.

A Faraday probe is a very simple planar electrostatic probe consisting only of an ion collector and an insulator. The ion collector is usually composed of tungsten to minimize the secondary electron yield and is biased negative with respect to local plasma potential. This negative bias repels electrons while simultaneously attracting ions. The ion collector is insulated from the surrounding plasma by an alumina tube. An additional electrode is also present on the outside of the alumina tube which serves to make a more uniform sheath. Figure

72 is a schematic of a Faraday probe while Figure 73 is a photo of the probe used in this study.

The ion collector has a diameter of 2.4 mm.

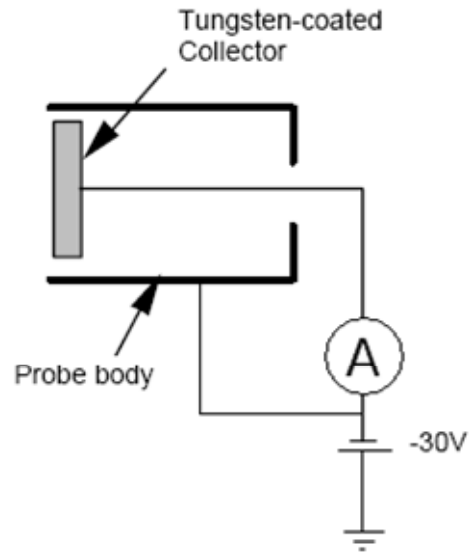


**Figure 72: Schematic of a Faraday probe**



**Figure 73: Photo of a Faraday probe with a dime for size comparison**

To obtain the beam divergence, the Faraday probe is swept in a constant radius arc from the center of the thruster exit plane at a series of discrete points. At each point in the sweep, the

collected ion current is measured and recorded generating an ion current density verses angle off-axis plot. Figure 74 is a Faraday sweep taken in of the bismuth thruster at a distance of 250 mm. The thruster was operating at 382 Volts and a discharge power of 1.72 kW. For comparison, Figure 75 is a Faraday sweep of a xenon plume.

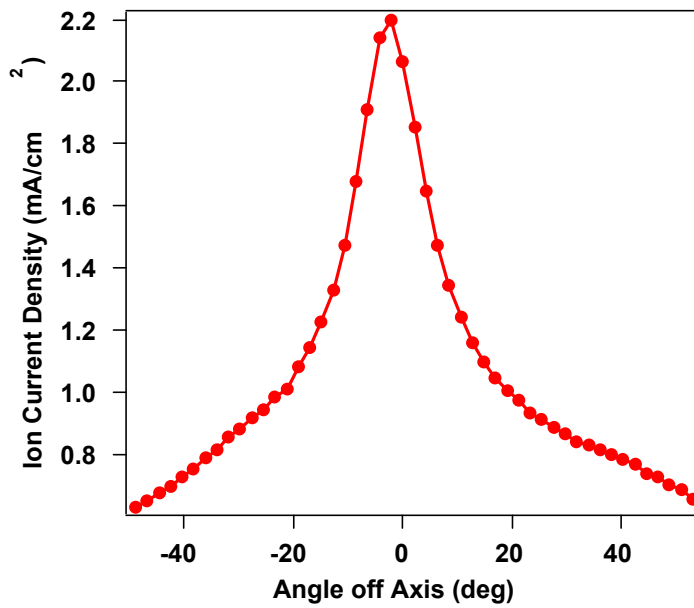


**Figure 74: Faraday probe sweep of the bismuth plume running at a distance 250 mm, 382 Volts and 4.5 Amps of discharge current**

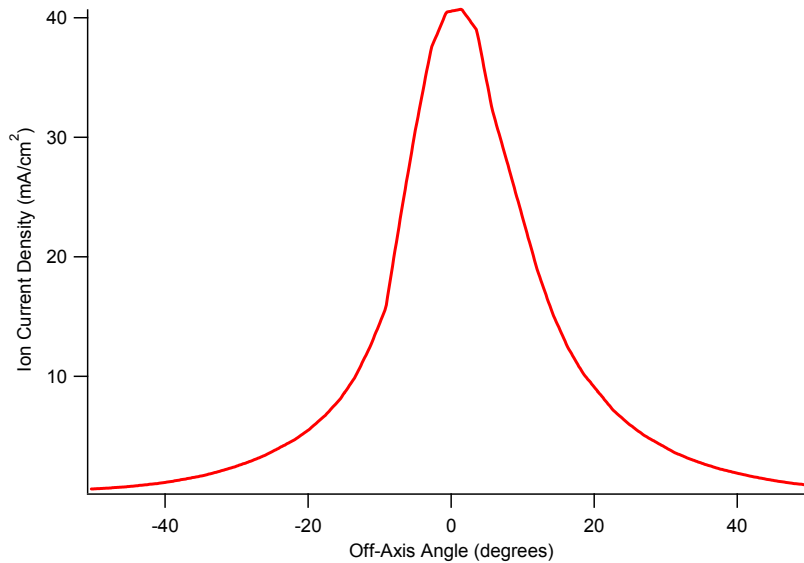


**Figure 75: Faraday sweep of a xenon thruster at 400 Volts and 6mg/s mass flow from Ref [55]. 42 deg**

The half-angle required to intercept 90% ion current for the bismuth thruster was approximately 42 degrees as opposed to 38 degrees for the xenon case. However, the magnetic field plays a critical role in determining beam divergence. In the xenon case, the magnetic field strength was tuned to provide maximum performance. This is currently not possible with the bismuth thruster since instantaneous mass flow measurements are unavailable making it impossible to accurately evaluate thruster performance in real-time.

### **6.3.3 Ion Energy Analysis**

A retarding potential analyzer (RPA) is a plasma probe that is used to ascertain ion energy in the exhausted plume. By examining ion energy it is possible to evaluate how effective the thruster is at accelerating the ions. To do this, the RPA, illustrated in Figure 76, makes use of several grids each with a defined purpose.

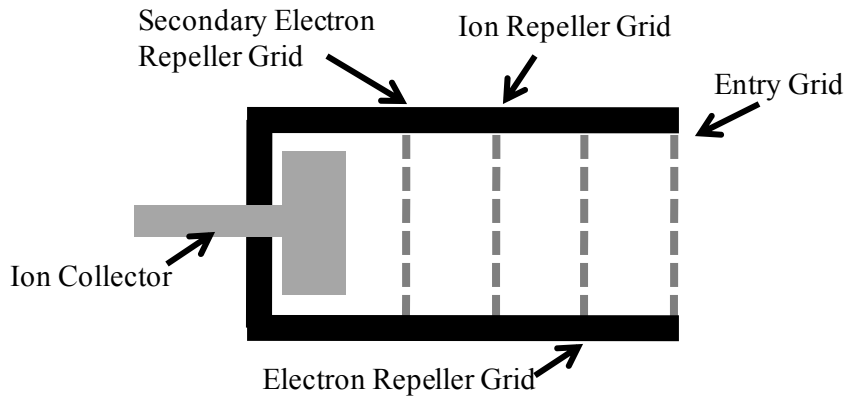


**Figure 76: Schematic of a retarding potential analyzer**

A more complete description of the design and use of RPA probes can be found in Refs [55, 71] but what follows is a qualitative description of the device. The opening orifice of this particular RPA is 12.7 mm in diameter. The first grid is the entry grid which is electrically floating or biased to plasma potential to prevent the probe from perturbing the surrounding plasma. The second grid is the electron repeller grid which is slightly negatively biased so as to repel any electrons in the incident beam. The ion repeller grid is the third and most important grid. The ion repeller acts as a potential hill allowing only ions with sufficient energy to overcome the potential hill to pass through to the detector - as the bias on the grid is increased, fewer and fewer ions will be able to pass. The final grid is the secondary electron repeller grid which acts to direct any electrons that may have been emitted from the collector, back to the collector thus negating their effect. All grids used are composed of stainless-steel mesh with a 0.139 mm average grid gap and 30% open-area fraction. Ion current was measured using a Keithley 2140 Sourcemeter configured in voltage-sweep mode.

Figure 77 is an RPA trace taken in the plume of the bismuth thruster while operating at a discharge voltage of 382 Volts and a discharge power of 1.72 kW at a distance of 500 mm. By

taking the derivative of the ion collector current, it is possible to obtain the most probable ion energy. From the plot, it can be seen that the most probably ion energy is approximately 365 Volts with respect to ground.

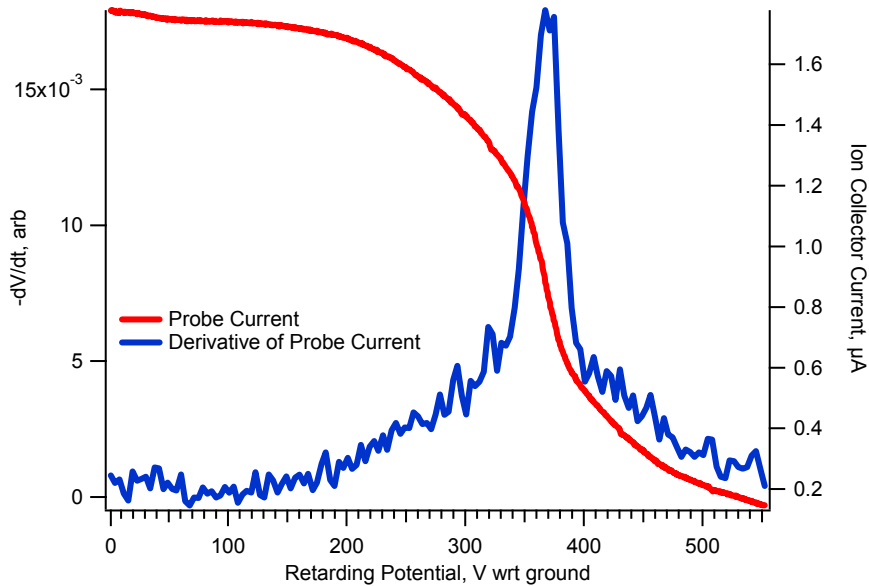


**Figure 77: Retarding potential analyzer data for the bismuth thruster running at 383 Volts**

In comparison, Figure 78 is an RPA trace for a xenon thruster which has the same anode geometry and magnetic circuit as the bismuth Hall thruster. The same RPA probe was also used. In this case, the thruster was running at a discharge voltage of 350 Volts with a xenon mass flow of 5 mg/s and the most probably ion energy corresponded to an ion repeller voltage of approximately 325 Volts with respect to ground. In the xenon case though, the local plasma potential was measured to be 45 Volts with respect to ground which imparts an additional 45 Volts of energy to the ions passing through the grounded grid. This additional voltage was subtracted off giving an actual most probable ion energy of 280 Volts with respect to plasma potential. No such measurement or correction was made with the bismuth Hall thruster but from

the shape of the derivative curve, it is reasonable to infer that the bismuth thruster was accelerating ions in a similar fashion.

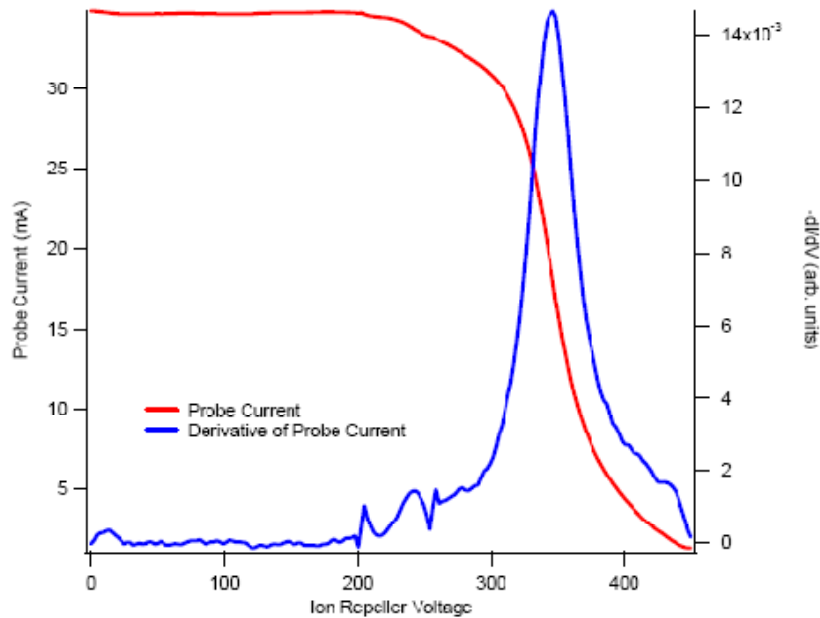


**Figure 78: RPA data from a xenon thruster running at 350 Volts, 5mg/s at a distance of 500 mm. Figure from Ref [55].**

## ***6.4 Summary***

This chapter focused mainly on the operational aspects of the bismuth thruster. The initial warm-up and ignition transients eventually give way to steady-state operation. This steady-state operation is maintained by a balance between back-streamed electrons and efficient operation. While at steady state, thermal imaging verified a uniform anode face temperature which is critical for even propellant distribution. Preliminary Faraday and RPA plume diagnostics were taken indicating that the thruster was indeed operating as a plasma accelerator.

## 7. Conclusions

This dissertation has detailed the development of a bismuth Hall thruster utilizing a very unique propellant delivery scheme. It has been demonstrated that the evaporation of bismuth directly from the anode is a viable way to efficiently deliver the bismuth vapors to the discharge chamber thus avoiding the large resistive power expenditures that plague other bismuth thrusters. The metallurgy involved in this development has yielded an anode that is essentially impervious not only to the thermal stresses of the direct evaporation but also to corrosive nature of the bismuth.

While the end result was a functioning thruster, there are still some very serious issues which need to be addressed. First and foremost is the instantaneous measurement of mass flow. Originally that was to be a central feature of this thesis but the engineering required to develop the thruster expanded to fill all the time allotted for developing mass flow measurement techniques. Second, while open-loop operation is possible, it is prone to oscillations and operational points of the thruster are restricted to those permitted by anode geometry and the characteristics of the porous vaporizer. That said, thermal control with the shim anodes should be pursued though it will certainly require computer control. A final concern is that bismuth may pose a significant spacecraft contamination hazard as the propellant could potentially obscure solar arrays and cause electrical shorts.

Although there have been many technical hurdles which have been overcome and likely many more to come in the future, there does not appear to be any single issue that will present an insurmountable obstacle to the further development of the direct evaporation bismuth Hall thruster.

## ***7.1 Bismuth as a propellant***

When compared to more traditional propellants, bismuth holds many practical advantages. Development of larger, more powerful xenon thrusters is currently hampered by the enormous ground testing infrastructure required to maintain a vacuum level conducive for representative operation of the thruster. Using bismuth as a propellant alleviates much of the pumping requirement as it is a solid at room temperature and any exhausted bismuth will simply re-condense and stick to the vacuum chamber walls effectively turning the entire facility into a pump. In this case then, only enough traditional pumping speed to keep up with leaks and any cathode flow is required.

The lower ionization energy of bismuth allows for significant efficiency gains at high mass flow, low voltage conditions which are characteristic of low specific impulse operation. The larger electron impact-ionization cross-section at low electron temperatures serves to further enhance low specific impulse operation. For example, in a 12-day LEO to GEO transfer, it is reasonable to expect a bismuth thruster to deliver up to 80% more payload than a xenon system for a 5,000 kg spacecraft.

## ***7.2 Direct Evaporation***

Previous bismuth thrusters have relied on vaporizing the bismuth external of the thruster and maintaining gas phase through a series of propellant lines and eventually to the anode. To prevent the bismuth from re-condensing, these propellant lines and the anode must be heated to temperatures in excess of 1000°C. At these temperatures radiation losses become very significant and require the dissipation of a significant amount of non-propulsive power. While these power losses are not included in anode efficiency, they have a drastic negative impact on overall efficiency.

To alleviate the need for gas-phase plumbing, the direct evaporation concept evaporates the bismuth directly inside of the anode. By utilizing the inherent waste heat generated by electrons impacting the anode face, the need for resistive heaters is eliminated. To keep the liquid bismuth contained in the anode but allow for bismuth vapors to enter the discharge chamber, a porous vaporizer is used. The porous vaporizer can be thought of as an array of very small capillaries with bismuth in direct contact on one side. The interfacial engineering concept of non-wetability prevents the liquid bismuth from entering the capillary but provides a free surface from which evaporation may take place. As the temperature of the porous vaporizer is increased the bismuth in contact with the vaporizer begins to evaporate. This evaporated gas enters the discharge chamber where it is then ionized and accelerated.

### ***7.3 Thermal Control with Segmented Anodes***

Substantial testing was done to evaluate the feasibility of thermal control using segmented anodes. Two inert electrically and thermally isolated “shim” anodes were integrated into the thruster. By varying the discharge voltage of the shims with respect to the main anode, it was possible to shift where the plasma current attached to inside of the discharge chamber. By having the capability to change where the discharge current is attaching it was then possible to control the temperature of the main anode. The steady state porous vaporizer temperature is bounded from above when 100% of the current is attached to the main anode and from below when 100% of the current is attached to the shims. A 50°C change in main anode operating temperature was observed which would correspond to nearly an order of magnitude change in the bismuth evaporation rate. Shifting current around in the discharge chamber did not affect performance outside of the margin of experimental error.

## ***7.4 Bismuth Materials Compatibility***

Bismuth has the ability to make low temperature alloys with most metallic elements. For most pedestrian applications, this is generally regarded as an asset. However, the nuclear power industry performed research and had some actual implementation of a lead-bismuth alloy in reactor cooling loops and the seemingly benign ability of bismuth's propensity to form alloys evolved into a critical concern of corrosion. As molten bismuth comes into contact with a metal for which a bismuth binary alloy exists, a mass dissolution attack ensues. This dissolution attack will eventually critically weaken the substrate material as it is pulled into a bismuth solution.

Binary phase diagrams are critical in the evaluation of the material compatibility with bismuth. For instance, iron has favorable resistance to bismuth at lower temperatures but above 800°C, it will slowly corrode. Shifting to titanium or an exotic steel alloy may seem like a cost effective solution, but bismuth is again incompatible with all but the refractory's at anode operating temperatures. However, in this application, stainless steel has sufficient corrosion resistance for the lower temperature components of the thruster such as the reservoir and the freezing valve but may not provide adequate resistance as an anode or porous vaporizer.

Since the fabrication of the anodes requires bonding, it should be noted that typical brazing materials such as silver and nickel are wholly incompatible with bismuth and will not withstand the temperatures required in the bismuth Hall thruster. Homogenous welding or diffusion bonding is the only appropriate way to join materials which will be in contact with high temperature bismuth.

## ***7.5 Stainless Steel Vaporizer Failures***

Stainless steel was used as the initial material for both the anode and the porous vaporizer. The commercial availability of porous stainless steel plates in a variety of average pore size and thickness allowed several different design permutations to be explored. Plate thicknesses ranging from 1.59 mm to 3.16 mm with 0.5  $\mu\text{m}$  and 10  $\mu\text{m}$  average pore sizes were tested. Although stainless steel proved to be a satisfactory material for the initial development of the direct evaporation bismuth Hall thruster, it was not thermally robust enough to sustain extended duration testing.

The thermal failure of the stainless steel vaporizer was always characterized by an initial plasma non-uniformity in the discharge chamber distinguished as a brighter region where the failure was initiating. As the evolution of the failure continued, small bright spots would begin to appear. These bright spots are actually discrete blobs of bismuth that have been extruded through and a pore that had grown exceptionally large. The reason for the expansion of the pore is thought to be that at the temperatures the porous vaporizer must run at, the stainless steel can continue to sinter causing some pores to shrink, while others to grow.

## ***7.6 Molybdenum Anodes and Molybdenum Powder Metallurgy***

To increase the thermal durability of the porous vaporizer, stainless steel was replaced with molybdenum. As there was no commercial supplier available for porous molybdenum, fabrication was done in-house. Using the porous tungsten powder metallurgy experiences from the 1960's and 1970's as a starting point, a method of fabricating a consistent and strong porous vaporizer evolved over the span of several months. Though initial efforts demonstrated the ability to reliably sinter molybdenum, the resulting disc was far too fragile to withstand any sort of bonding. To alleviate that problem, a vacuum hot press was used which vastly increased the

strength of the porous material. The powder was compacted at 1000 psi while being heated at 1100°C for 4 hours. The final resulting discs have densities around 55%.

Attaching the porous vaporizer to a full-density molybdenum anode proved exceptionally difficult. Attempts to TIG weld the vaporizer resulted in severe oxidation and cracking of the anode body as well as irreparable damage to the vaporizer. The anode and vaporizer were also sent out for electron beam welding but the porous molybdenum would tend to crack at the weld interface. The final solution was to perform a solid state weld also known as a diffusion bond. Diffusion bonding relies on the same mechanisms as sintering to create a stable bond. Initial attempts at diffusion bonding indicated that the bonding operation must take place at a temperature and pressure greater than that which formed the porous vaporizer. Excellent mechanical strength was achieved by applying 3,300 psi to the bond interface while at a temperature of 1200°C and remaining at those conditions for 2 hours.

Attaching the propellant supply and drain tubing to the molybdenum anode also proved to be problematic. Again, attempts to TIG weld led to unsatisfactory results. Electron beam welding exhibited some amount of initial success, but after several thermal cycles, the weld eventually failed. The failure mechanism is believed to be additional grain growth caused by the extreme temperatures required by the welding process. To alleviate any additional welding problems, an anode and tube stub assembly was fabricated out of a single piece of molybdenum. However, no data from that anode is included in this study.

### ***7.7 Thruster Operation and Diagnostics***

To initiate the evaporation of bismuth, the anode must first be brought to a temperature in excess of 700°C. The first way of reaching this temperature was to “jump-start” the bismuth evaporation using a unique dual propellant anode. The thruster is initially operated on xenon gas

until the anode achieves a sufficiently high temperature at which the bismuth evaporation rate becomes appreciable. As the anode continues to heat up, xenon flow is slowly reduced until it is eliminated completely leaving the thruster operating on bismuth only. While this method of starting the thruster proved reliable, the power levels at which the xenon-bismuth transition occurred at were too much for many of the thruster parts to withstand not to mention that the turbo-pumped facility was struggling to keep up with the xenon flow.

A resistive heater was developed to solve the problems associated with the xenon-bismuth anode. In this case, the anode contains only bismuth and is heated to the required ignition temperature by a boron-nitride insulated rhenium-doped tungsten heater wire. This heating platform has demonstrated excellent durability and does not thermally over-stress the thruster. The resistive heater is then turned off during steady-state thruster operation.

Although the evaporation rate of bismuth was intended to be controlled by discharge power sharing inert shim anodes, it was found that the thruster could be run with a single anode in what is essentially open loop mode. The only feedback for the system is that which is provided by setting the discharge power supply into constant current mode. While in constant current mode, the discharge voltage is allowed to rise and fall which has the effect of increasing or decreasing the temperature of the anode and therefore bismuth evaporation rate. The mechanism by which this works is presently not well understood and will be the subject of future investigations.

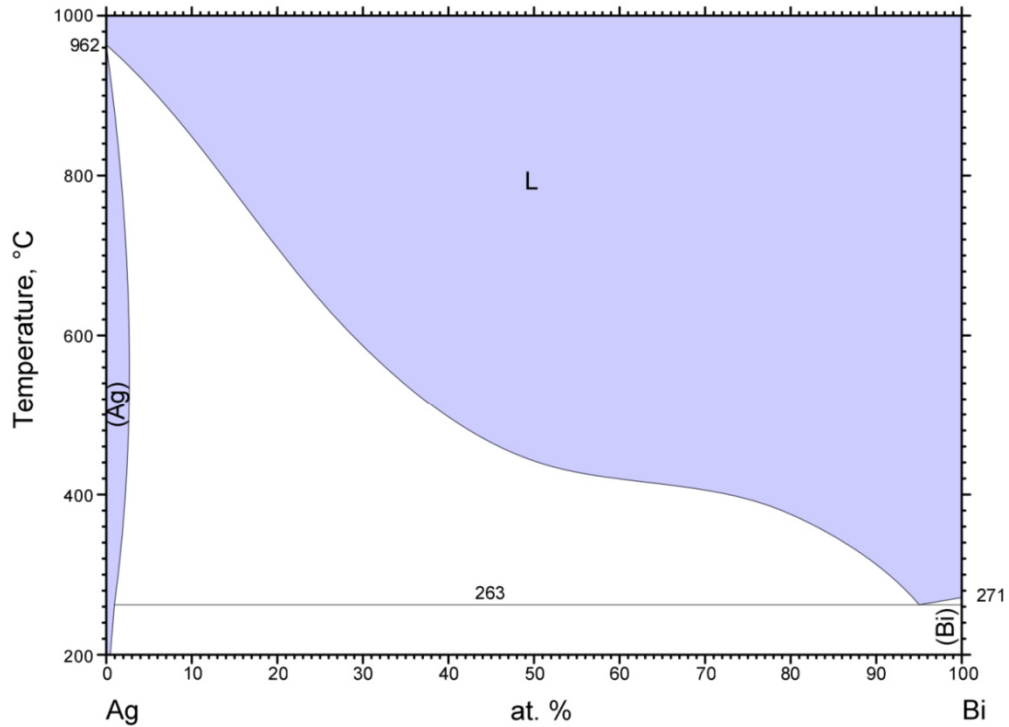
While running in open loop mode, there have also been some interesting oscillations observed. While discharge current oscillations are expected in Hall thrusters, they generally occur in the kHz range. In this case though, additional oscillations had a period of approximately 40 seconds. The root cause of these oscillations is believed to be an interaction of the thermal

mass of the vaporizer and the subsequent bismuth evaporation rate which actually controls the overall discharge power.

Due to time constraints only preliminary plume diagnostics were performed on the bismuth thruster. When compared to xenon thrusters of similar anode geometry and magnetic circuit, the bismuth thruster performs similarly though with poorer performance in the case of beam divergence. These performance liabilities could likely be recovered by optimizing the applied magnetic field to maximize performance – a task which is easy with the xenon thruster, but quite daunting with the bismuth thruster.

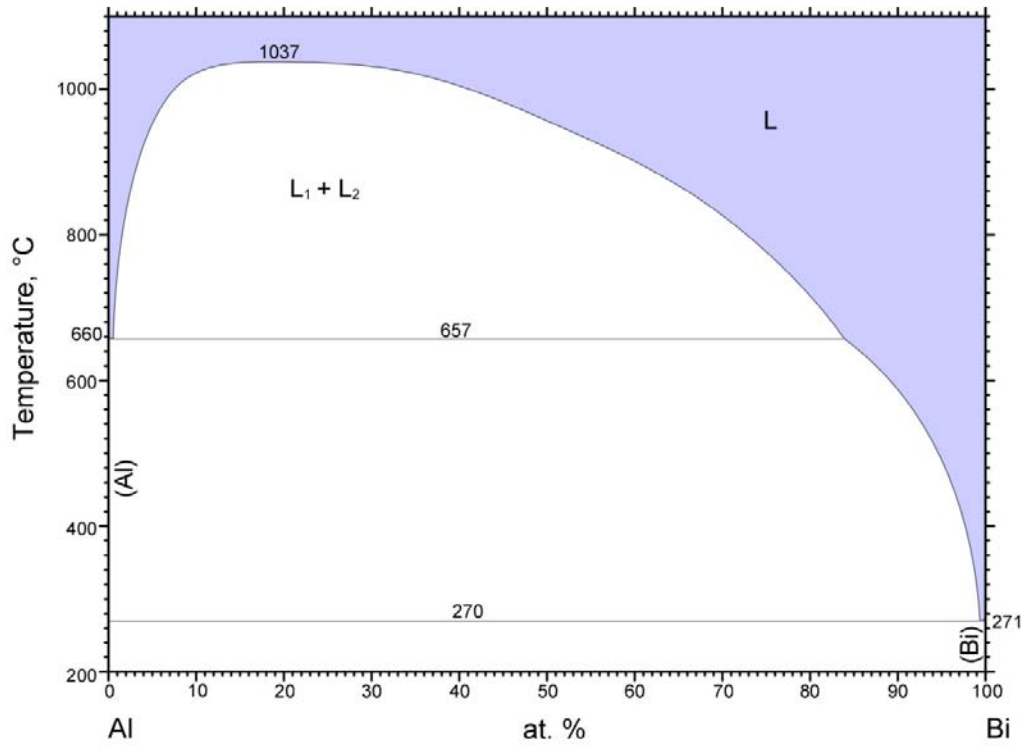
# Appendices

## Appendix.A Phase Diagrams



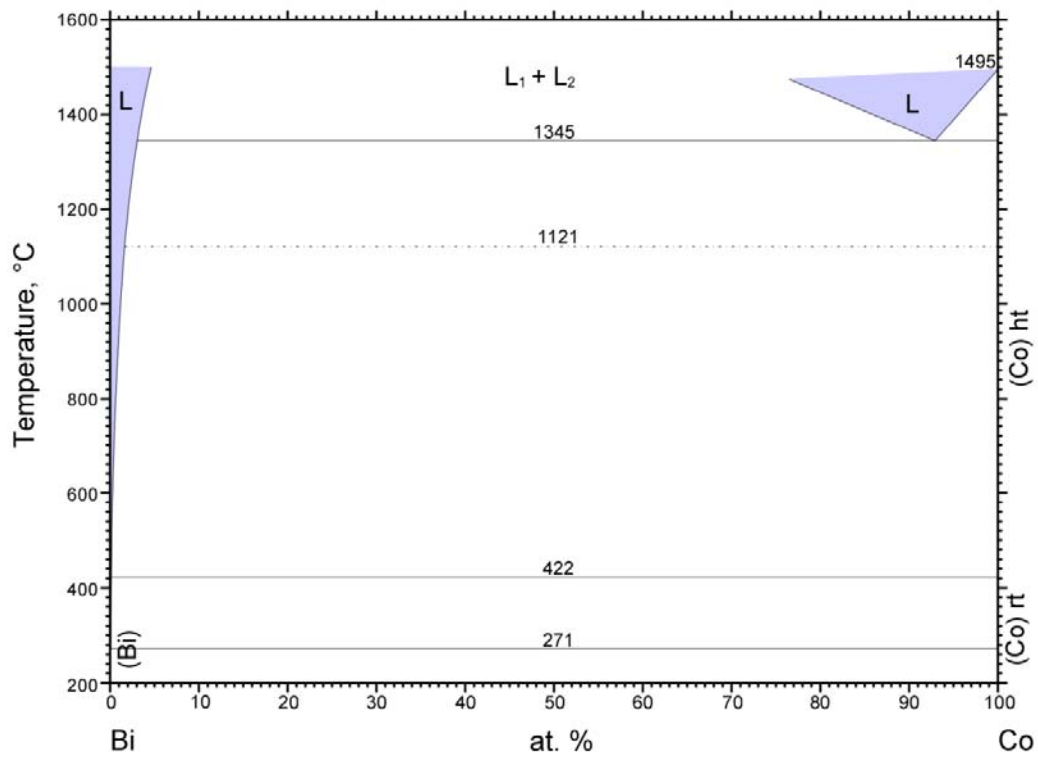
© ASM International 2006. Diagram No. 981026

**Figure 79: Silver-Bismuth phase diagram from Ref. [72]. According to the phase diagram, a silver substrate should not be expected to withstand molten bismuth. Reprinted with permission of ASM International®. All rights reserved. Permission letter can be found in Appendix D.**



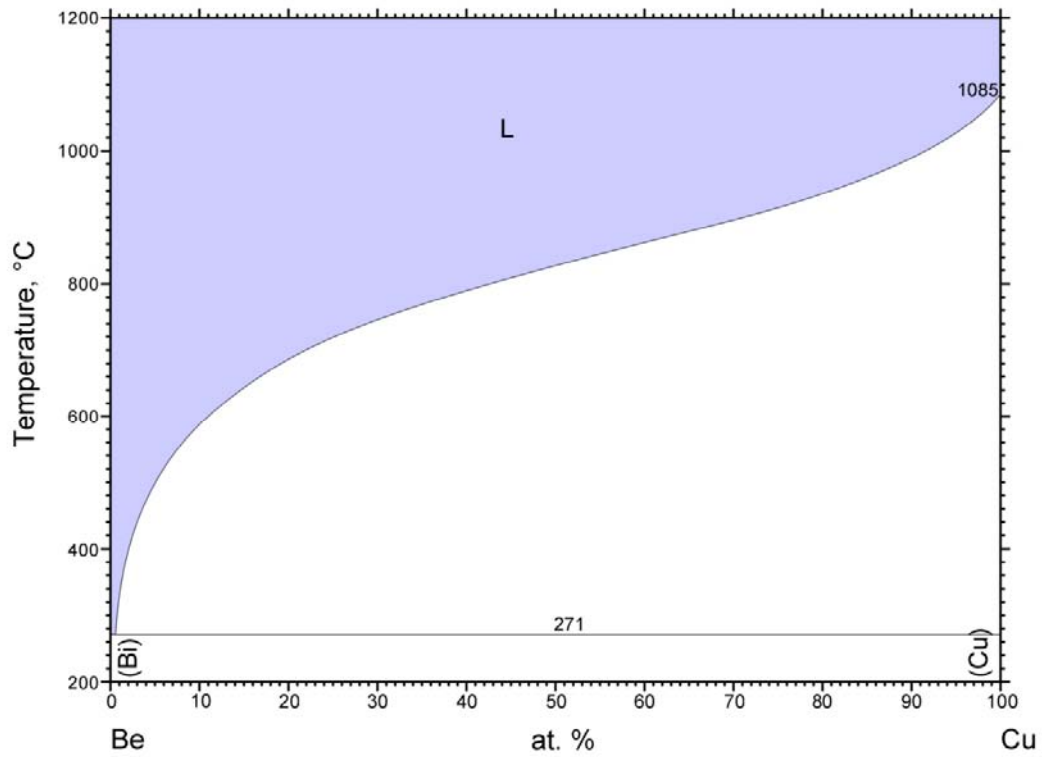
© ASM International 2006. Diagram No. 900078

**Figure 80: Bismuth-Aluminum phase diagram from Ref. [73]. According to the phase diagram, an aluminum substrate should not be expected to withstand molten bismuth. Reprinted with permission of ASM International®. All rights reserved. Permission letter can be found in Appendix D.**



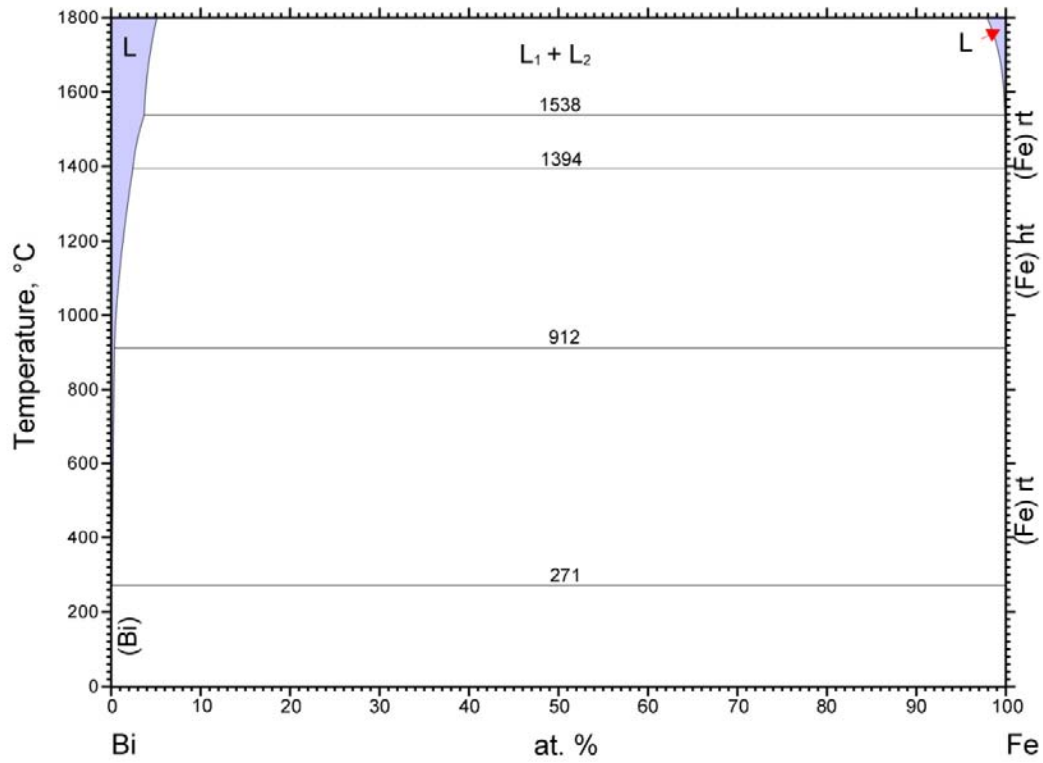
© ASM International 2006. Diagram No. 900429

**Figure 81: Bismuth-Cobalt phase diagram from Ref. [73]. According to the phase diagram, a cobalt substrate should not be expected to withstand molten bismuth. Reprinted with permission of ASM International®. All rights reserved. Permission letter can be found in Appendix D.**



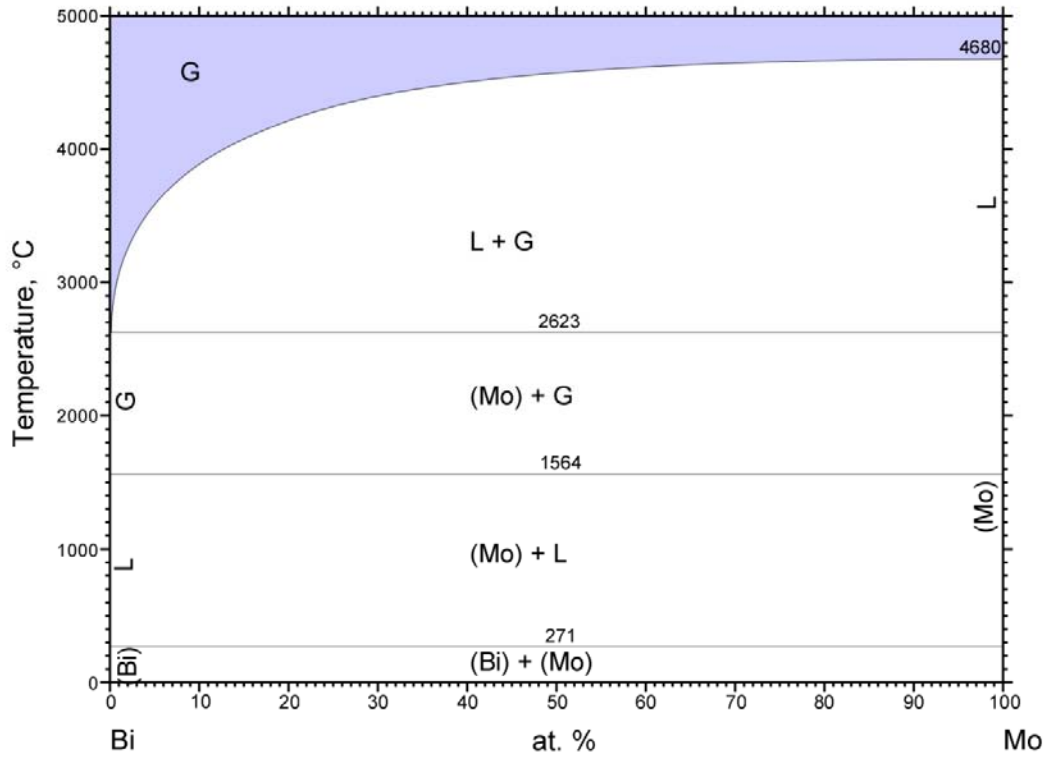
© ASM International 2006. Diagram No. 900432

**Figure 82: Bismuth-Copper phase diagram from Ref. [56]. According to the phase diagram, a copper substrate should not be expected to withstand molten bismuth. Reprinted with permission of ASM International®. All rights reserved. Permission letter can be found in Appendix D.**



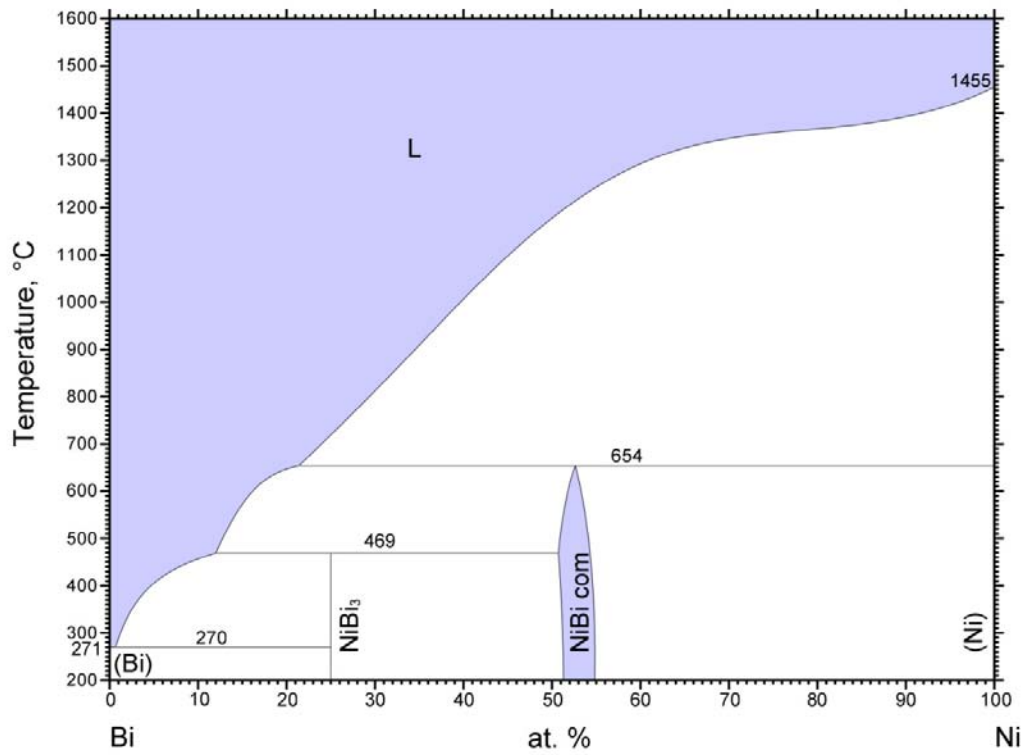
© ASM International 2006. Diagram No. 900435

**Figure 83: Bismuth-Iron phase diagram from Ref. [74]. According to the phase diagram, iron will have some high temperature susceptibility to molten bismuth. Reprinted with permission of ASM International®. All rights reserved. Permission letter can be found in Appendix D.**



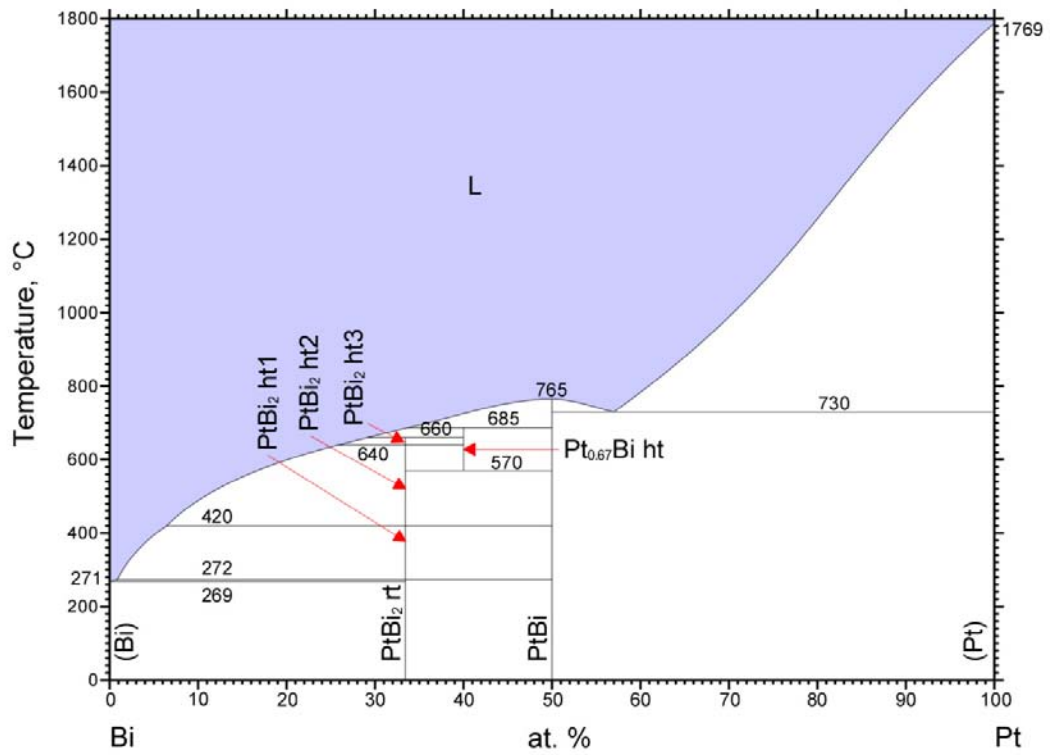
© ASM International 2006. Diagram No. 900451

**Figure 84: Bismuth-Molybdenum phase diagram from Ref. [74, 75]. According to the phase diagram, the use of molybdenum in a molten bismuth environment should not create any adverse material compatibility issues. Reprinted with permission of ASM International®. All rights reserved. Permission letter can be found in Appendix D.**



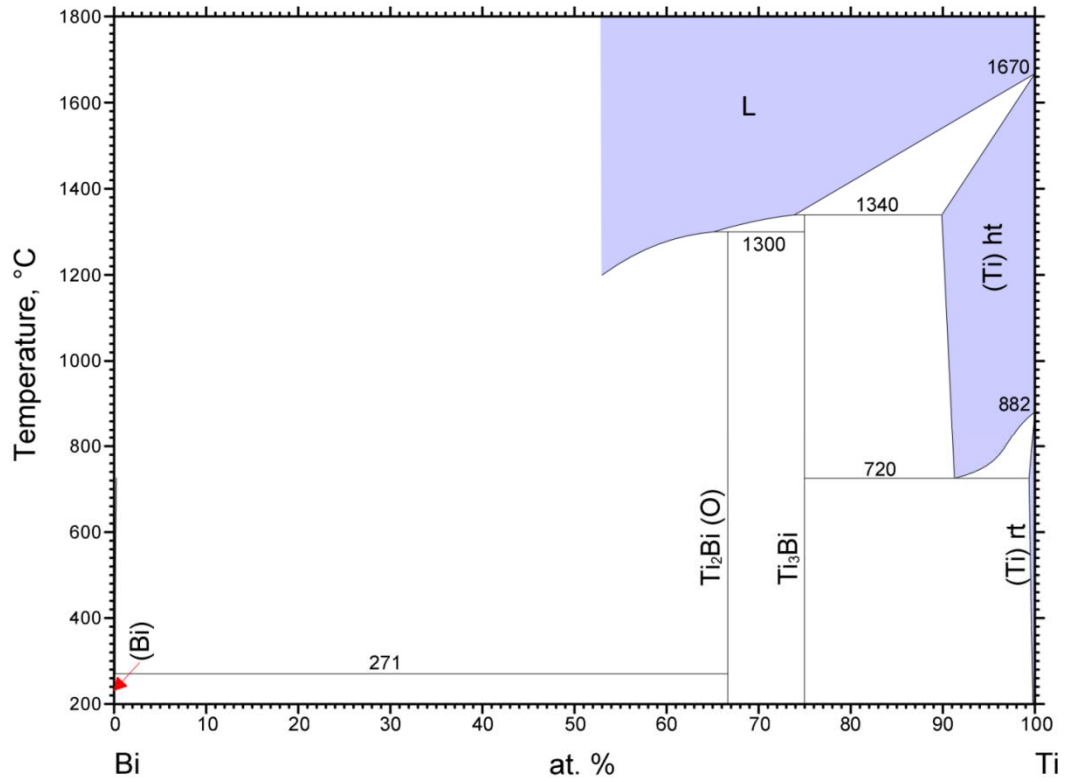
© ASM International 2006. Diagram No. 900455

**Figure 85: Bismuth-Nickel phase diagram from Ref. [75]. According to the phase diagram, a nickel substrate should not be expected to withstand molten bismuth. Reprinted with permission of ASM International®. All rights reserved. Permission letter can be found in Appendix D.**



© ASM International 2006. Diagram No. 979935

**Figure 86: Bismuth-Platinum phase diagram from Ref. According to the phase diagram, a platinum substrate should not be expected to withstand molten bismuth. Reprinted with permission of ASM International®. All rights reserved. Permission letter can be found in Appendix D.**



© ASM International 2006. Diagram No. 900477

**Figure 87: Bismuth-Titanium phase diagram from Ref. [76]. According to the phase diagram, a titanium substrate should not be expected to withstand molten bismuth. Reprinted with permission of ASM International®. All rights reserved. Permission letter can be found in Appendix D.**

## **Appendix.B Molybdenum Anode Fabrication Procedure**

The molybdenum anode is central to the successful operation of the bismuth Hall thruster. However, to facilitate enhanced performance, it may be necessary to fabricate a new anode with different geometric dimensions and porous diffuser properties. This chapter will walk through the recommended procedure to fabricate a completely new anode. This process has four major steps: anode blank fabrication, porous disc fabrication, diffusion bonding and propellant line attachment. Each will be independently addressed.

### ***B.1 Molybdenum Anode Blank Fabrication***

In most cases, fabricating a new anode blank should be unnecessary as the porous face is easily machined off. However, in the unlikely event that a completely new anode must be fabricated there are only a few considerations to be addressed.

From a practical standpoint, machining molybdenum is not exceptionally difficult but does require the use of sharp carbide tools. If the tools are not sufficiently sharp, they will tend to cleave into the bulk molybdenum causing irreparable damage to the part and potentially people and machinery. It is also not valid to assume that anything arriving from a supplier is actually flat. The process used to make fully dense molybdenum produces raw stock that is not necessarily of consistent thickness.

If the anode dimensions are remaining unchanged from what is reported in this work, then the minimum size of the raw material is a plate 3.5"x3.5" that is 0.6" thick. The plate area is of course fixed by the anode outer diameter but the thickness has been minimized down to the point where the 0.25" diameter propellant line fits in the middle without hitting the back of the anode or interfering with the porous plate. The holes for the propellant line should be drilled

prior to diffusion bonding to eliminate the chance of overstressing and breaking the bond. The channel width is exactly 0.25” which was deemed to be the smallest face grooving tool that could be used without significant tool deflection. If the piece is to be fabricated on a mill rather than a lathe, it is also not recommended to move to a narrower channel width.

## ***B.2 Porous Disc Fabrication and Diffusion Bonding***

The fabrication of the porous disc is a much more involved process than the initial anode blank fabrication. It is not recommended to attempt to fabricate a porous disc outside of a vacuum hot press as the lack of hot compaction yields very brittle parts. Changing the powder size, sintering temperature, sintering time and compaction pressure will have very tangible results of the resultant disc. No parametric study was done to quantitatively establish exactly which parameter has more effect on a given property from qualitative experience and the kinetic nature of the process, temperature and compaction pressure will have created the most significant change in the final result.

## ***B.3 Porous Disc Fabrication***

The porous disc fabrication procedure is straightforward though rather time consuming. The first step in the process is to prepare the graphite die for use. Depending on the condition of the die, this requires some amount of scraping with a blade to remove any material that may remain from the previous user. This is important as it ensures purity in the sample but also makes releasing the finish product from the die vastly easier. Do not apply the boron-nitride mold release to the walls of the die as this will change the dimensions enough to cause problems with the rams scraping the boron-nitride into a heap on top of the powder to be pressed which has obvious disastrous implications.

The top and bottom rams are prepared similarly. The first step is to shave off any remaining sample or boron-nitride mold release using a frosting knife. This should leave the surface of the ram smooth and clean. Now apply enough of the spray-on boron-nitride mold release to turn the pressing interface white. The spray contains acetone so wait until it has completely evaporated. The ram interface surface should now be uniformly and smooth in appearance. To facilitate the installation and removal of the ram, again use the frosting knife to scrape away any boron-nitride that may have coated the perpendicular surface. The die and ram assembly should look similar to Figure 88.

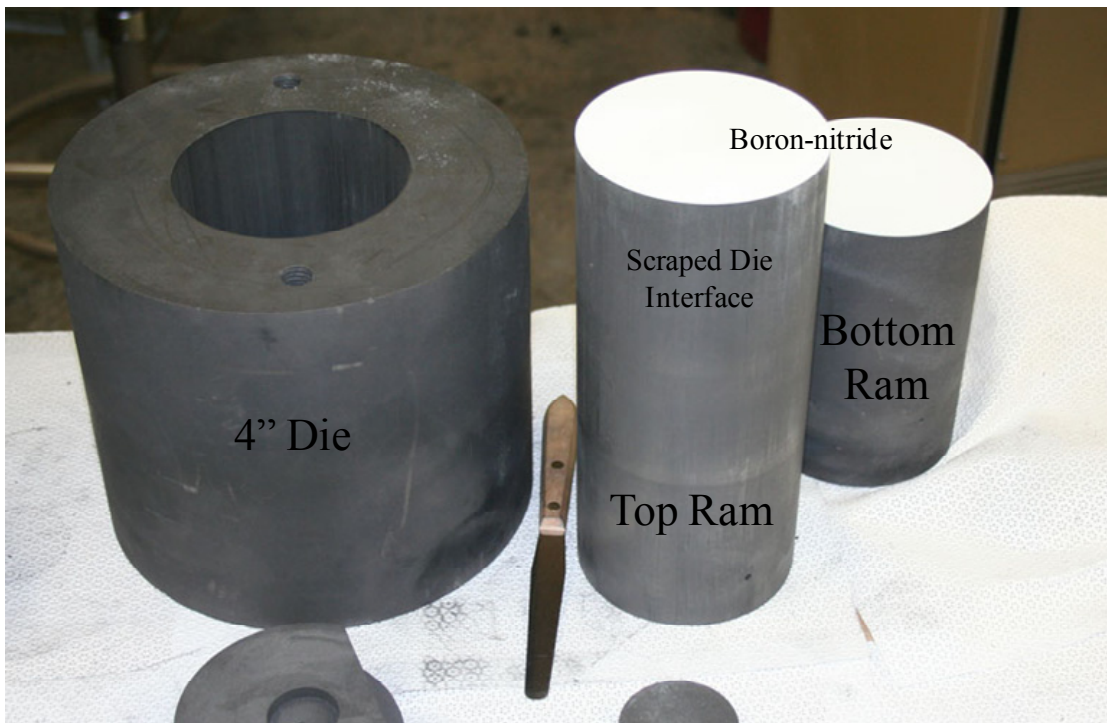


**Figure 88: Prepared die with boron-nitride coated rams**

The molybdenum powder does not require any additional preparation. The particle size and distribution of the powder are essentially irrelevant in terms of the fabrication procedure. If the 4'' ram is being used, 125 grams of molybdenum will yield a plate approximately 0.1'' thick.

This is useful thickness for diffusion bonding since it offers a good balance between strength and the need to machine away excess material. Discs that are too thin will not have the requisite internal strength to reconcile the differences in flatness between the disc and the anode blank.

With the powder massed and the rams and die prepared, insert the die and the lower ram into the hot press. Next add the molybdenum powder. Spend a moment or two leveling out the powder on the ram with the frosting knife taking special care that there are no large lumps of molybdenum near the die walls. With the powder is somewhat level, insert top ram. When it settles on top of the powder, spin it several times to further spread the powder evenly. The sample installation is now complete but pressure should not be applied until later. Subsequent vacuum hot press pump-down procedures should be followed.

As the chamber is pumping down, configure the PID controller with the temperature set point and turn the heater control switch to "ON". When the vacuum hot press has achieved a pressure safe to enable heat, the sample will begin heating at a rate of 10°C /min. When the control system indicates the temperature is above 400°C but below 1000°C, apply pressure to the sample. Waiting until 400°C allows for many of the organic volatiles to evaporate and should improve the quality of the results while pressing after 1000°C could cause densification problems due to high temperature molybdenum malleability and non-uniform temperature distributions across the die face.

Unfortunately, the vacuum hot pressed used in this research did not have closed loop control on the applied pressure. The implications of this are that if the pressure is applied at 400°C, the pressure at 1200°C has been observed to increase up to 20% due to the thermal expansion of the graphite rams and the mild steel pressing ram. The competing mechanism of sample densification serves to balance out some of the thermal expansion effects but it is critical

that the sample not be pressed near the limit at lower temperatures since thermal expansion may cause the press to exceed its ratings.

*Although the intention of this chapter is to detail the procedure of hot pressing rather than comment on the validity of various conditions, pressing at temperatures below 1100°C and below compaction pressures of 8,000 lbs on a 4" die (655 psi, 4.5 MPa) will not produce favorable results.*

After the initial warm-up to the pressing temperature, the typical hold time has been 4 hours. This number has been chosen to be consistent with powder metallurgy's typical 1, 4 and 20 hour hold times. Four hours has been proven to be a reasonable duration as most of energetically favorable kinetic particle fusion takes place in approximately the first hour so unless achieving maximum density is the goal, there is little reason to hold the temperature longer. *It should also be noted that the vacuum hot press used in this study is not capable of achieving fully density molybdenum due to both temperature and pressure limitations – 60 to 70% is the likely maximum density possible.*

When the hold time has elapsed, the PID controller set point should be set to zero rather than just terminating heater power. By allowing the PID controller to retain control of the heating system, the cooling rate will proceed at 10°C/min until about 200°C when such a cooling rate is difficult to sustain considering the thermal masses and the vacuum conditions involved.

If expediency is in required, the heat may be immediately terminated and the vacuum chamber may be flooded with argon when the temperature drops below 800°C and opened to atmospheric forced convection below 500°C. Regardless, the die and rams will take at least two hours to cool but due to the high thermal conductivity of graphite will remain essentially isothermal. This creates a very significant burn hazard since the process thermocouple is not

integrated into the die / ram assembly and simply reports the ambient air temperature. The expedited vent has not shown to induce any ill effects in the resulting discs but is potentially hazardous to the user.

#### ***B.4 Diffusion Bonding Preparation***

Preparation of the constituent parts of the diffusion bonding process is a key element in the success of the bond. The porous disc that was previously fabricated should have a thin film of boron-nitride on it. Experience has shown that boron-nitride film from the release agent is weakly soluble in acetone so it is suggested that the part be immersed in an ultrasonic cleaner with an acetone cleaning medium for at least 30 minutes. The boron-nitride will slowly settle out to the bottom of the ultrasonic cleaner but the acetone should be changed as soon as it takes on a consistently opaque appearance. To prevent the auto-ignition of the acetone during machining, the part should be thoroughly purged with water and surface dried. Unless it is baked out beyond the boiling point of water, it will be impossible to dry the entire disc so density measurements should not be taken unless proper bake out procedures have been followed; pulling vacuum is not enough to ensure the water did not turn to ice rather than evaporate.

Since the ram and die alignment angles are not guaranteed much beyond a few angular degrees – especially under pressing, the porous disc stands almost no chance of emerging completely flat. To regain control of the flatness and provide as favorable a bonding surface as possible, the porous disc must have the bond interface machined. It is imperative that the machined bond interface is created by a carbide tool with a diameter larger than the channel width. If a smaller tool is used, there is a significant risk that the inherent gouging caused by the tool flutes on a boundary will cause excess and detrimental spacing in the diffusion bond

(anything above 30 $\mu$ m has the potential to flow liquid bismuth through it in normal operating conditions).

After machining, the porous disc should be flat enough for diffusion bonding but the same cannot be said for the destination anode blank. If the anode blank is new, it was probably created on a mill and is not properly prepared for the diffusion bonding process. The only way to guarantee the flatness is to use a CNC lathe. If the anode blank is being recycled, ensure that the previous porous plate was completely removed and the surface was again flattened. Incidentally, the tool marks from flattening the anode blank seem to have no adverse impact on the diffusion bond and may actually aid in the process as they serve as a thermodynamic stress point thus inducing higher density sintering.

When the machining process is complete it is imperative to verify the porosity of the porous plate to ensure that machining process did not close off porosity. The lack of low temperature malleability of molybdenum should preclude this unless excessively high feed rates and tool speeds allow heat to build up. Surface grinding will cause pore closure. As a rule of thumb, if the porous surface is elementally shiny, it is not porous anymore. Acetone seems to be the best indicator of open porosity since it appears to be the most wetting on the molybdenum substrate. Isopropyl alcohol and normal tap water are also excellent indicators of porosity and actually emulate bismuth from a surface energetics standpoint more accurately than acetone[77] though acetone has proven more useful for identifying potential leaks (likely due to acetone's wettability on molybdenum or residual molybdenum oxide).

### ***B.5 Diffusion Bonding Procedure***

The diffusion bonding procedure is very similar to the molybdenum disc fabrication in both underlying physical process as well as procedure. If the preparation steps laid out in the previous

section were followed with due diligence, the diffusion bonding process should prove to be every bit as consistent as the porous disc fabrication.

The diffusion bonding process does not require a die but the top and bottom ram are still required to provide the bonding pressure. In fact, if the anode blank is being recycled, using the die is not an option anyway since the propellant line tubes will not fit into the die therefore for consistency sake, *using the die is not recommended*. On the other hand, care must be taken to ensure the tube stubs are short enough to allow for the anode to be positioned in the center of the rams and away from the carbon heating elements. Although stainless steel threads and alumina insulator tubes will survive this process it is absolutely not recommended that any Swagelok fittings besides the permanently attached nut and ferrule are included. The stainless steel cold weld that is responsible for the Swagelok seal will fuse together resulting in a very permanent junction that is not at all responsive to mechanical or thermal coercion.

The same boron-nitride mold release spray that was applied to the rams during the fabrication of the porous disc should also be applied to the rams during diffusion bonding. The carbon in the rams will certainly form an untenable bond with porous molybdenum under the conditions required of the diffusion bond (see Section 5.3.4.1).

Since the die is not used, only the lower ram needs to be installed before anode blank and porous plate are placed in the hot press. Whether the porous disc is on the bottom or the top doesn't matter from a technical standpoint, it is much easier to center the anode blank when the porous disc is on the bottom.

Once the position of anode blank and porous plate are centered on the rams as best as possible, the vacuum hot press is ready to operate. Subsequent vacuum hot press pump-down procedures should be followed to establish a favorable bonding environment.

As the chamber is pumping down, configure the PID controller with the temperature set point and turn the heater control to “ON”. When the vacuum hot press has achieved a pressure safe to enable heat, the sample will begin heating at a rate of 10°C /min. No pressure should be applied to the sample until the temperature has reached at least 1000°C as molybdenum gains a slight bit of malleability which reduces the chances of fatal cracking. Once 1000°C has been eclipsed, slowly apply pressure keeping in mind the very limited area that pressure is being applied to.



**Figure 89: Diffusion bonded anode immediately after bonding**

The last remaining task is to machine off the excess porous plate. Although both milling and using the lathe have been done, the lathe seems to be the easiest.

## **Appendix.C      Operation of the Bismuth Hall Thruster**

Successful operation of the bismuth thruster does require a significant amount of handling and preparation that is not required for xenon Hall thrusters. For reasons explained later in this appendix, the thruster must be almost completely rebuilt after every single run whether the test was successful or not. This appendix will walk through all the steps required for the safe and reliable operation of a bismuth thruster from start to finish.

### ***C.1 Anode Preparation***

The first step in the rebuilding of the thruster concerns the anode. If the freezing valve emptied cleanly, there should be little residual bismuth left in the reservoir, anode and the freezing valve itself. The less bismuth remaining the better as residual bismuth makes reloading troublesome. In the infrequent case that there is significant residual bismuth left in the reservoir, it is un-swaged from the anode and emptied with an acetylene torch (vastly faster than a propane torch). To prevent potential damage, the anode is never heated, regardless of the amount of residual bismuth contained within. With the reservoir and anode as clean as they are going to get, they are again swaged back together and massed. This mass will be used to calculate how much bismuth was added to the system.

The bismuth that is to be used in the thruster does not undergo any additional purification or other manipulation; it is simply crushed with a hammer into a coarse powder with a grain size similar to very coarse sand. A piece of tape is placed over the exit of the freezing valve to prevent any bismuth from traversing the entire anode assembly. The pulverized solid is then funneled into the empty reservoir and through a process of vibration, the finer material settles out of the reservoir and into the anode cavity. This process is repeated until the reservoir is full of

powder. To prevent any spillage, the top of the reservoir is heated with a propane torch to melt the top most layer of bismuth. When the heat is removed, the bismuth freezes, encapsulating the remaining powder.

Preparation of the freezing valve depends on which type of anode is being used. If a stainless-steel anode is being used, a tube stub greater than 8.5” will remain sufficiently cool so as not to drain the anode early. If a molybdenum anode is in use, the vastly higher thermal conductivity requires a liquid-cooled freezing valve. The liquid-cooled freezing valve illustrated in consists of two stainless-steel tubes welded in a cross pattern that is swaged onto a shorter tube stub on the lower part of the anode. Figure 90 is a photograph of the liquid cooled freezing valve.

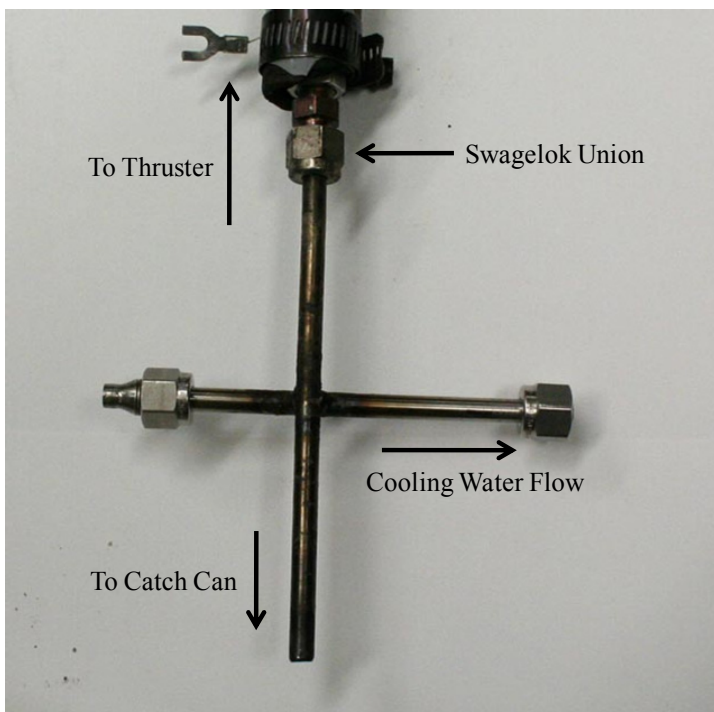


**Figure 90: Photograph of the liquid cooled freezing valve**

Water flows through the horizontal cross cooling the valve, thus preventing premature draining of the anode. Regardless of which is used, to prime the freezing valve, the anode is

flipped so the top of the reservoir is pointing downward. The tape that was preventing any bismuth from making it all the way through the anode is removed and a very fine bismuth powder is added and vibrated until the entire length of the tube stub is completely full. Heat is again applied to the tube stub but stops about an inch short of the anode to prevent any liquid bismuth from forming in the anode cavity. As the powder compacts as it is melted, more bismuth is added to tube until the entire tube is full of liquid. At this point, heat is removed and the now properly primed freezing valve is allowed to cool. The anode and reservoir assembly is then massed to establish the total amount of bismuth in the system. It should be noted that when calculating maximum possible run times, only the bismuth remaining in the reservoir after the anode has been filled is used because running with a partially full anode could have disastrous consequences.

With the anode full of bismuth, electrical connections and thermocouples can be attached and not be subjected to the damaging effects of a propane torch. The electrical connection to the anode is made by spot welding a stranded 16 AWG wire with very high temperature insulation directly to a random spot on the reservoir. This wire and any thermocouples are then routed out through the top of the reservoir. Thermocouples are not always included in the instrumentation though for several reasons. First, every connection that is made to the anode will have to be at anode potential. This creates a serious liability since it requires that insulation on every inch of thermocouple wire is perfect otherwise there will be arcing and the thermocouple wire will burn up like a fuse until it gets to something important. Second, after running many tests, the thermal responses of things such as the freezing valve and reservoir are very predictable and are therefore not worth risking the success of the test for redundant information. Third, the thermocouple that is spot welded as close to the vaporizer as possible tends to interact with the plasma. This interaction can cause the temperature reading to be 1°C to 1500°C degrees higher or lower than it

actually is so the only way to get the actual temperature is to turn off the discharge voltage. Every second the discharge voltage is off, the probability that the thruster will be able to restart without heaters drops drastically.

After the requisite instrumentation is attached, the reservoir heater is installed over the reservoir. The reservoir heater consists of a piece of laminated garolite alumina tightly wrapped with several feet of tungsten wire. Three wraps of stainless steel foil are wrapped around the heater assembly to reflect radiative heat back towards the reservoir. To prevent the stainless steel foil from shorting the tungsten heater wire, Tescil high temperature fiberglass insulation is wrapped around the top and the bottom providing an effective standoff. Instrumentation wires are fed through the heater core but are not taped into place until much later.

## ***C.2 Heating System Preparation***

The resistive heating system used to bootstrap bismuth evaporation is very sturdy but after several uses the tungsten heater wire tends to get brittle and break while the thruster is being removed. Using 2% rhenium-doped tungsten greatly extends the time it takes for embrittlement, but it still occurs. Rebuilding the heater takes only a matter of minutes but it still must be properly done to ensure even heating and to prevent cross-channel shorts. Two 48" pieces of the rhenium-doped tungsten are used during each heater rebuild and constitutes the bulk of consumables for the bismuth thruster. The two pieces are placed side by side and make four isolated loops in the narrow grooves in the lower boron-nitride heater and are then routed out to the back of the thruster via a hole in the heater and boron-nitride body assembly as illustrated in Figure 91.

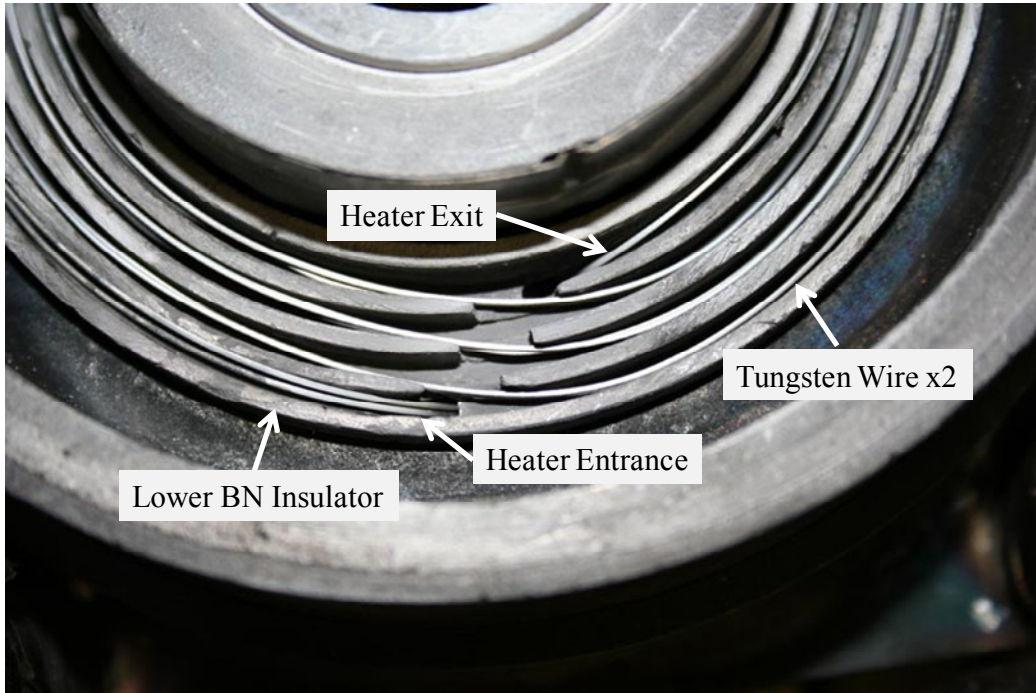


**Figure 91: Close view of the tungsten heater wire installed in the lower boron-nitride insulator**

The upper heater part with the anode alignment ring fits snugly over the lower heater part, effectively isolating the tungsten wire contained within from the discharge chamber. This assembly is carefully inserted into the lower part of the boron-nitride body that is already sitting on the magnetic circuit back plate.

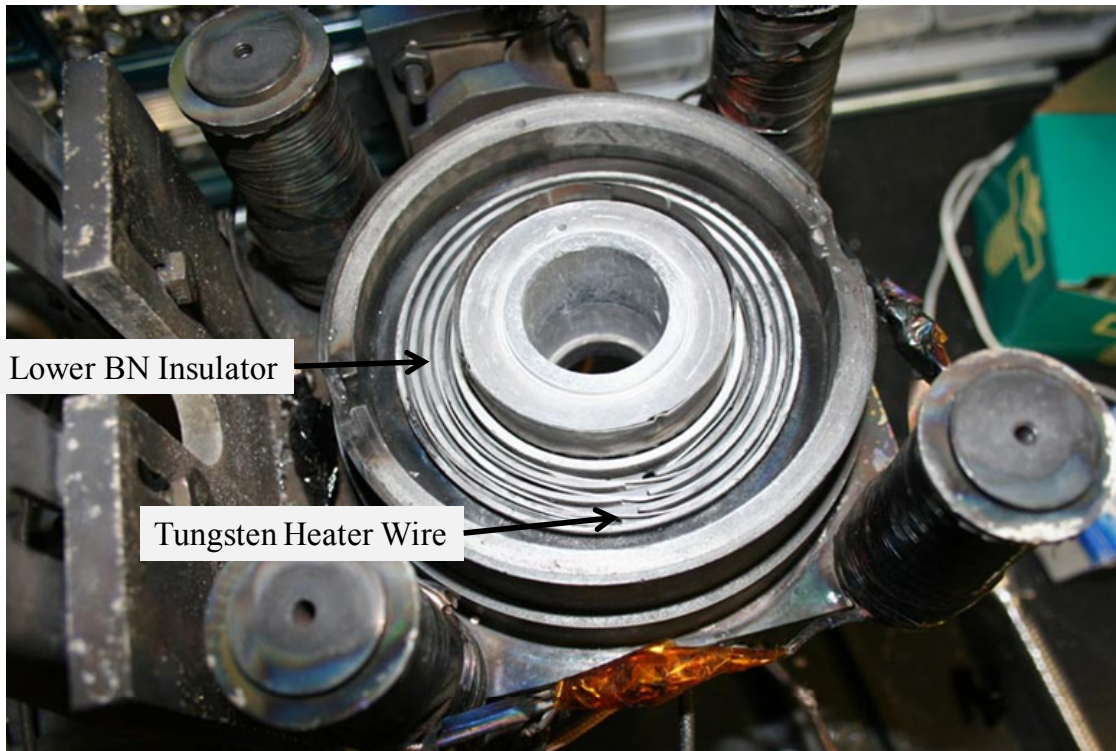


**Figure 92: Photograph of the anode heater before the upper BN insulator is installed**

To enhance the thermal performance of the discharge chamber, multi-layer insulation (MLI) consisting of strips of stainless steel, molybdenum or tantalum are placed in key areas. The MLI acts as a radiation reflector with each subsequent layer reflecting most of the thermal radiation back to the direction it came from. In a typical setup, each of the three areas where MLI is used has between three and five layers of foil.

### ***C.3 Final Assembly***

After the heater assembly is installed, the thruster is now ready to receive the anode / reservoir assembly. The anode / reservoir assembly is carefully placed on top of the upper heating part which centers the anode in the discharge chamber. Alumina tubes are slid down into

the 0.5” hole in the boron-nitride body as illustrated in Figure 93 to provide electrical isolation of the propellant line tubes.

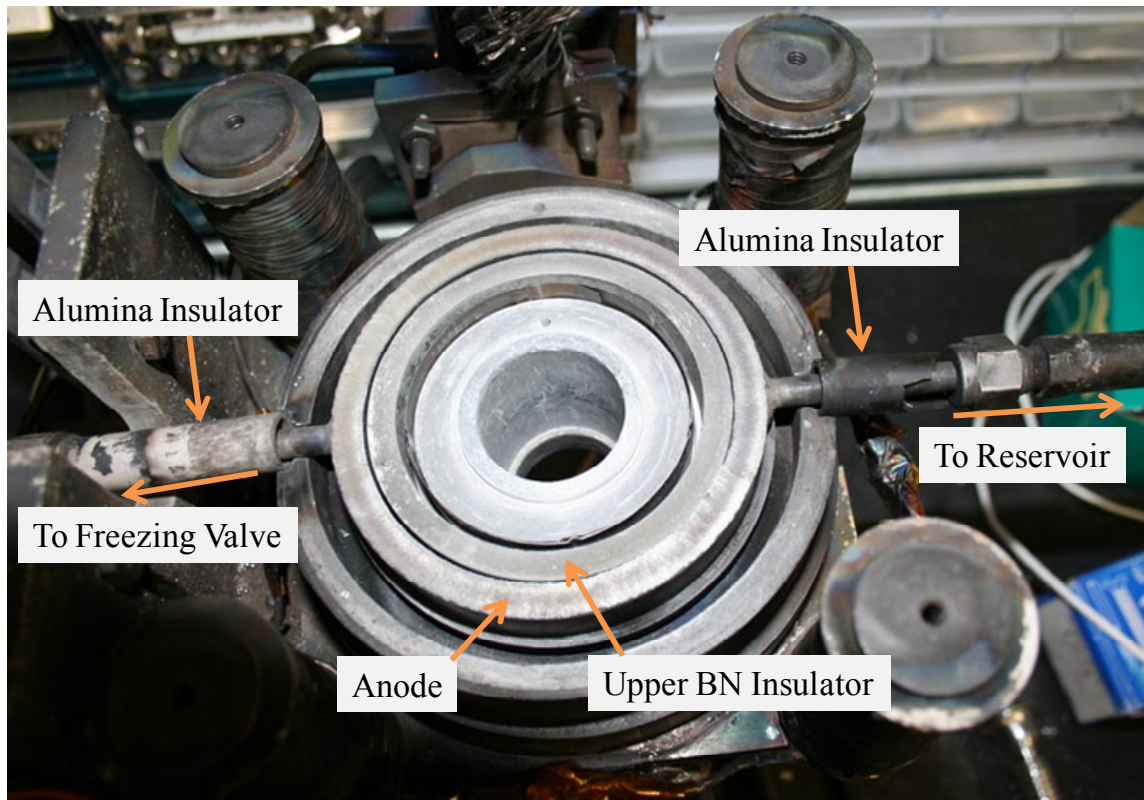


**Figure 93: Photograph of the anode and anode heater installed**

The top part of the boron-nitride body is then installed, followed immediately by the outer guard ring and finally by the front magnetic plate which is bolted to the electromagnets. The holes in the boron-nitride for the reservoir feed tube and freezing valve prevent the anode from rotating in place. The garolite insulating tube from the reservoir heater is slid down until it contacts the boron-nitride body. At this point, the instrumentation wires are fusion-taped together at the top of the garolite, which prevents movement of the reservoir heater.

The passively cooled freezing valve is insulated by using a method similar to the reservoir heater. A garolite tube several inches longer than the freezing valve tube is pressed into contact with the boron-nitride body and is friction fit in a narrow gap in the mounting plate of the thruster. To provide heat to open the freezing valve, several wraps of tungsten wire are wound around the garolite and secured with hose clamps. No MLI is used in this case because it is imperative the freezing valve remain as cool as possible until the appropriate time.

The liquid-cooled freezing valve has a different method of preparation since it requires a high temperature swage joint near the thruster. It is imperative to secure the alumina tube that will provide electrical insulation for the tube stub near the anode. There are a variety of ways to do this, but the best way is to slide the alumina tube into place and use a combination of fusion tape and kapton tape to secure the end nearest to the freezing valve. There is no expectation that these adhesives will retain any ability to secure parts other than by their own eventually charred mass. Before swaging the freezing valve onto the tube stub, two short pieces of garolite must be placed on either side of the swage joint. After tightening the union, the garolite is pressed into contact with the boron-nitride body and is friction fit in a narrow gap in the mounting plate of the thruster. The second piece is secured to the first by using several wraps of fusion tape. This union will remain cool enough so as to not compromise the integrity of the adhesive. With the garolite secured in place, the remaining exposed tubes can be insulated by simply wrapping them with fusion tape. The liquid-cooled nature of the valve will prevent the fusion tape from thermally failing. The liquid-cooled freezing valve is not likely to open when cooling water is turned off so it is prudent to add some additional heat to ensure proper operation. The supplemental heat is provided by wrapping a couple of feet of tungsten heater wire around the drain leg of the freezing valve and securing it on both ends with hose clamps. Care should be taken not to compromise the fusion tape. With the anode assembly secured and insulated, the

inner guard ring and the center magnetic pole are installed and secured. The thruster is now ready to be moved into the vacuum chamber for the final installation tasks.

#### ***C.4 Vacuum System Integration***

If the thruster is rigidly attached to the vacuum system, the fixture used to rebuild the thruster is simply integrated as appropriate. If the thrust stand is used, stand-offs raise the thruster high enough above the cooling shroud to allow enough room for the freezing valve and catch can. The laboratory cathode is typically mounted on one of the sides of the thruster as the propellant feed system prevents the more conventional top mounted cathode.

The electrical schematic for the bismuth thruster with the usual wire lead number, and potential current and voltage loads is shown in Figure 94. The electrical infrastructure of the Bismuth Test Facility can currently provide twelve 600+Volt connections capable of continuously carrying 33 Amps each to the thrust stand; even with the high current requirements of some of the heaters, there is no danger of overloading the wiring.

## Electrical Schematic, Wiring Requirements and Pinouts for the Bismuth Hall Thruster

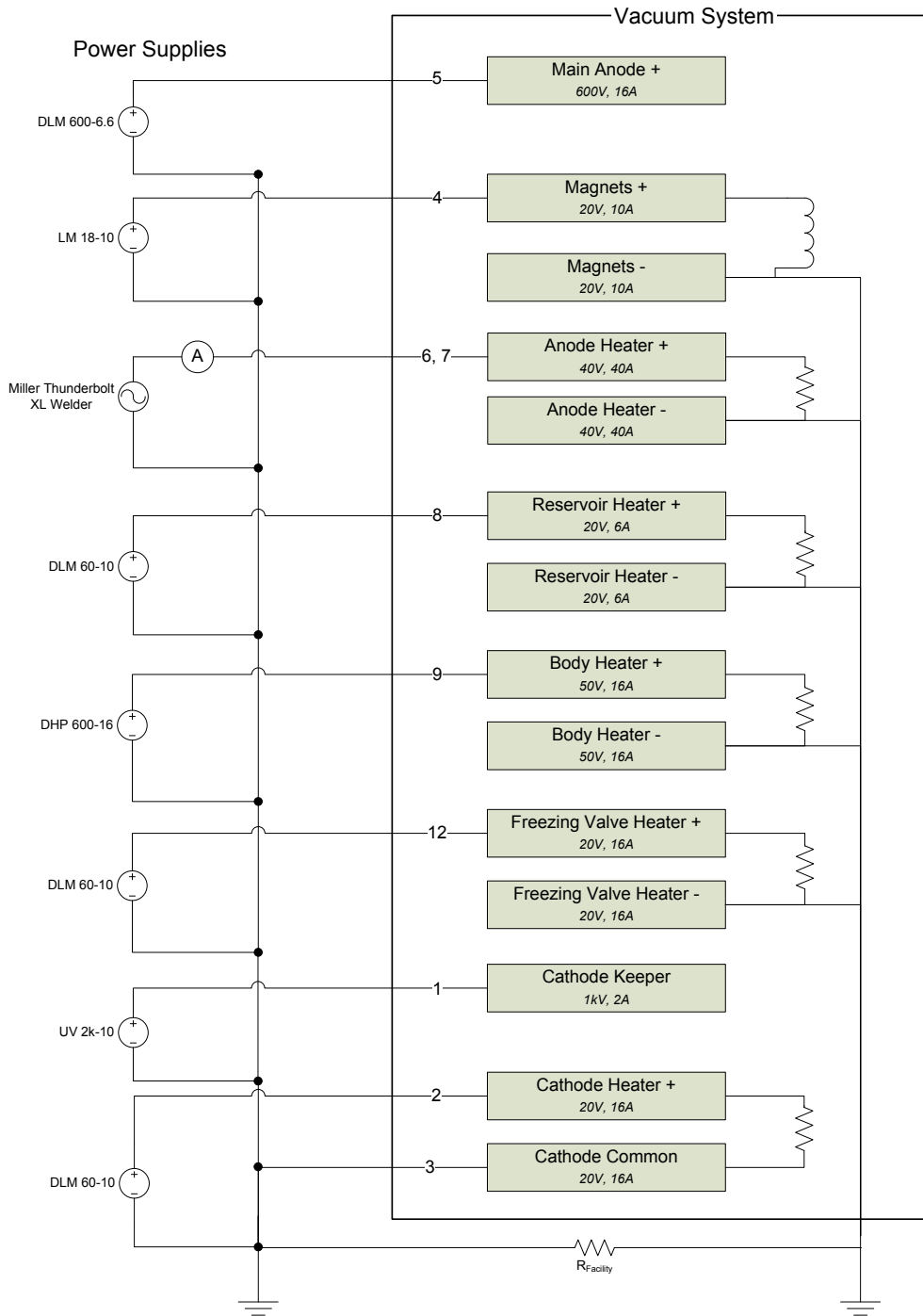


**Figure 94: Electrical schematic**

The last electrical connections are made to the anode heater and the reservoir heater to reduce the chances of breaking the relatively fragile tungsten wire. For safety and instrumentation reasons, this thruster has always been run in a grounded condition meaning that there is no electrical isolation between the vacuum system and the thruster body. As such, return lines for the reservoir heater, body heater, freezing valve heater and anode heater are simply tied to facility ground. If thermocouples are being used on high-voltage areas of the thruster, the entire length of the thermocouple wire is additionally insulated with a layer of fusion tape until it connects to the facility infrastructure. This additional precaution arose from many thermal radiation-induced failures of thermocouple insulation.

If necessary, flexible nylon tubing is used to draw the cooling water from the thrust stand or facility water supply. The non-conductive nature of the plastic provides a very effective electrical isolation of the freezing valve with very minimal leakage current through the cooling water itself. Cryobreaks could also be used for electrical insulation, but their rigid nature makes routing water lines cumbersome. It is imperative that any connective nut in contact with the nylon and high voltage be well insulated as an arcing event may breach the nylon causing a very large pressure spike as the water freezes which could cause severe damage to the turbomolecular pumps.

In order for the freezing valve to open, it is necessary to purge the water from the valve when it is time to drain it. The simplest way to do this is to isolate the supply and return water lines from the thruster cooling system and purge the remaining water out of the lines with an inert gas. For added safety, vacuum is pulled on the isolated lines so in the event of a line breach during heating, the potential for pump damage is minimized. Figure 95 is the functional diagram of the freezing valve system with inert gas purge and vacuum enhancement.

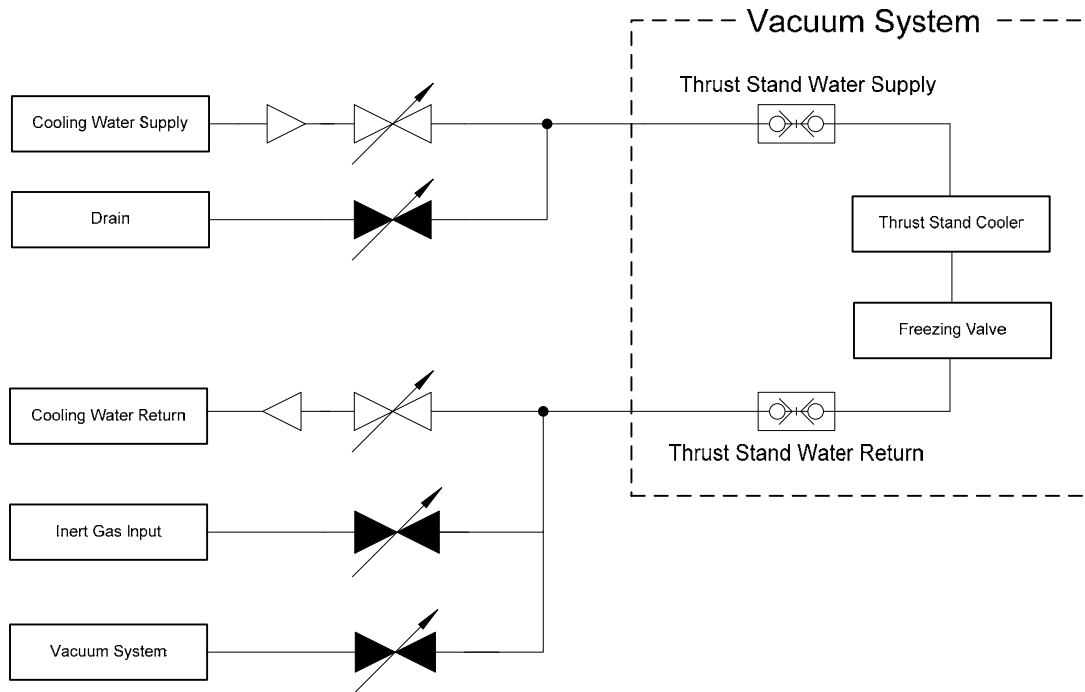


**Figure 95: Functional diagram of the freezing valve purge system.**

The last thruster-related task is to mass and install the bismuth catch-can in a position that will not interfere with thrust stand operation and with the freezing valve exit slightly inside of the catch-can. This step prevents any bismuth from splashing out of the catch-can in the event the valve opens in a non-uniform manner. At this point, the thruster is ready to run and should look similar to Figure 96.

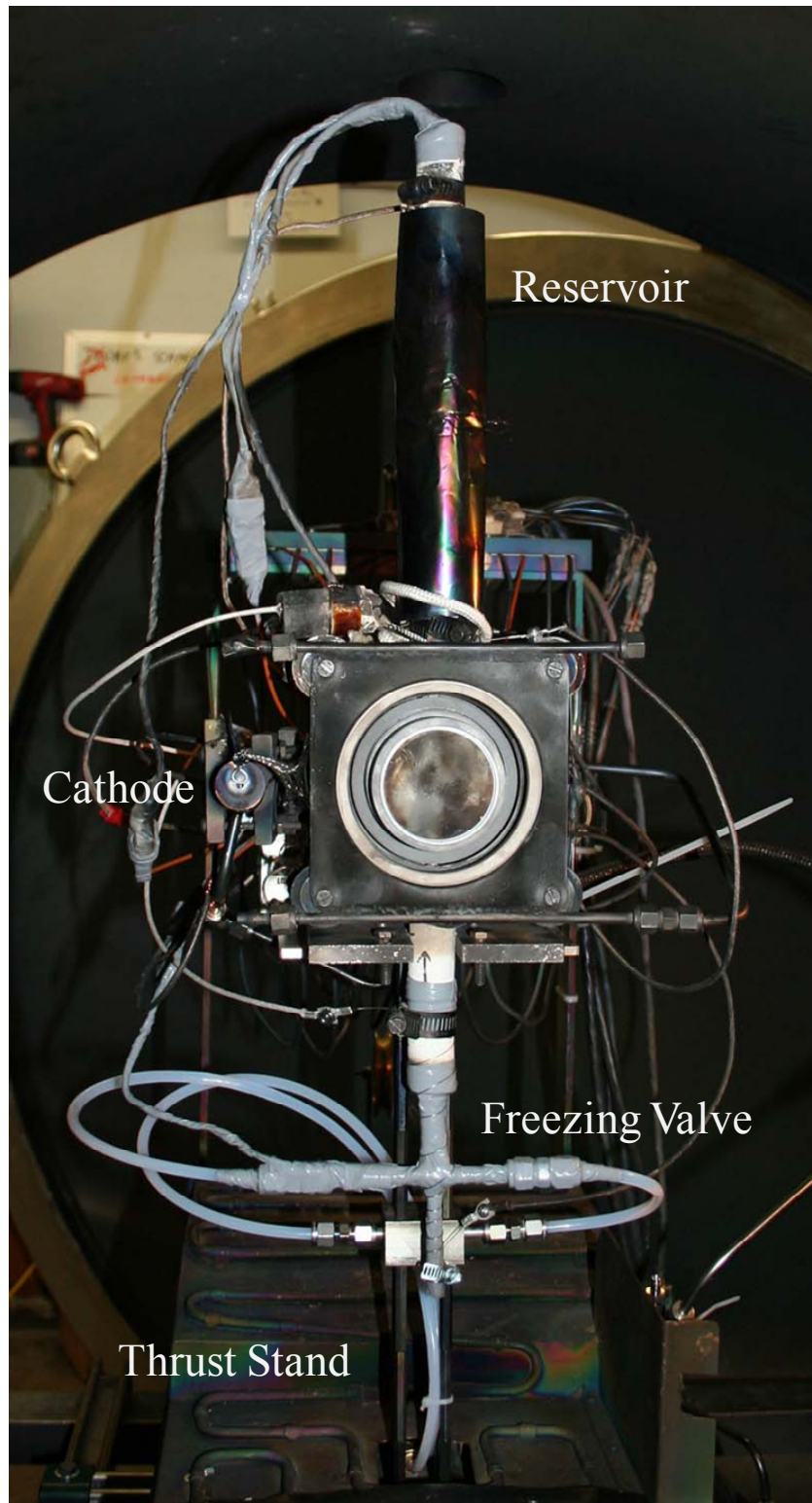


Figure 96: Thruster mounted on the thrust stand ready to run

## ***C.5 Warm up***

Before any heat is applied to the thruster, the cathode operation is verified and voltage is applied to the anode to check for any arcing. The sole reason for this is that once the anode is heated it must be drained at the conclusion to prevent any bismuth expansion damage. If the cathode, high voltage and auxiliary diagnostics all check out, it is safe to begin heating the anode.

The initial heating has two stages. The first stage consists of a lower power level which is intended to melt the bismuth throughout the reservoir and anode as well as provide an initial warm-up of the thruster body reducing later thermal transients. The second stage is meant to bring the anode to a temperature suitable for operation. In the first stage, the Miller welder is set to the lowest possible AC current which is between 21 and 23 Amps at 24 to 30 Volts depending on the I-V characteristics of the anode heater wire. 60 Watts is also applied to the reservoir heater to melt the contents and ensure the anode is completely filled with bismuth before the thruster is ready to light. If thermocouples are used, there will be periods when the anode temperature will rapidly drop and then increase again; this is the relatively cool bismuth draining into the anode. The first heating stage is complete when the anode temperature has begun to stabilize and the reservoir temperature is above 300°C. This process takes between 30 and 45 minutes.

At the start of the second stage of heating, the anode should be near 600°C and completely full of liquid bismuth though the bismuth evaporation rate is still essentially zero. To approach starting heat, current on the anode heater is increased until welder output is approximately 850 Watts. The reservoir heater is turned down to 50 Watts at this time as well. After several minutes the anode temperature should be climbing past 750°C though slowing down.

The final move to starting heat is to bring the welder output to 950 Watts should get the anode to approximately 800-850°C. As soon as the power is increased to the starting level, the magnets are set to 1 Amp and the anode discharge voltage are turned on to 300 Volts with a 4 Amp current-limit to give a measure of the evaporation progress. If for some reason the anode does not achieve a sufficiently high temperature using only the anode heater, 10 Amps can be applied to the body heater to deliver the last few degrees.

As the starting temperature is approached, the discharge current slowly increases. When there is approximately 0.5 Amps of discharge current, the thruster will be prone to anode arcing events due to the high electron mobility in the weak magnetic field. At this point, the thruster can potentially be lit. To light the thruster, the magnetic field strength is slowly decreased which will induce a significant increase in anode arcing events. Eventually, when the magnetic field is low enough, the anode power supply will enter a current limited mode with a discharge stable voltage between 60 and 100 Volts. When a steady discharge is present, the anode heater and body heater are completely turned off. The effect of this is very drastic as a 90-200 Amp-turn solenoid inside of the thruster has just been removed. The magnetic field is now increased slowly until the nominal 300 Volt thruster operating voltage is reached but is still running at a constant current. At this point, the thruster is placed in a self-moderating mode, by increasing discharge voltage to 400 Volts while leaving the current fixed. The thruster now has a mechanism by which to increase or decrease the power level which subsequently controls the bismuth mass flow rate.

### ***C.6 Ignition Transients***

With the discharge current now stabilized for the given magnetic field configuration, the thruster enters a period of thermal ignition transients. Although previously explained in Section 4.8, it is worth repeating the mechanism behind the thermal transients. Consider again the

representative I-V behavior shown in Figure 45 for two different values of mass flow. For constant current operation, if the mass flow increases, the discharge voltage necessarily decreases from V2 to V1 as the thruster transitions to the higher I-V curve. This decrease in voltage, with current constant, reduces the power deposited into the anode face and, hence, reduces the bismuth evaporation rate. The same stabilizing effect would happen for a decrease in mass flow – the overall power would increase and would tend to restore the mass flow to its design value. The effect is then to correct thermal excursions away from the thruster “set point,” which is determined through thermal design of the device and the geometry of the vaporizer. The voltage oscillations slowly damp out over a period of approximately an hour. It should be noted though, that changing the discharge current or the magnetic field will cause additional thermal transients even if the changes are made from steady state operation.

### ***C.7 Shutdown and Propellant Dumping***

Shutting down the thruster is certainly more involved than simply extinguishing the discharge voltage, though that is the first step. Once the discharge voltage is turned off, the anode will drop several hundred degrees quite quickly. However, in an effort to get as much bismuth out of the system and in to the catch-can as possible, the anode heater is turned back on though at the lowest possible current; 60 Watts is also applied to the reservoir heater. The ionization gauge is turned off at this point since several gauge tubes have been damaged by leaving the filament on when the very hot bismuth empties into the catch can causing a bit of a pressure spike.

The next step depends on which type of freezing valve is being used. If the passive freezing valve is installed, this process is very easy: 10 Amps are applied to the freezing valve heater. After about 5-10 minutes, if the thruster is on the thrust stand, a significant change in

thrust is measured when the anode and reservoir drain. Otherwise, a thermocouple in the catch-can is an accurate indicator as well.

Getting the liquid-cooled freezing valve to open requires significantly more work. The first step is to turn off the cooling water and purge the liquid out of the freezing valve which makes it vastly easier and safer since there is not a need to boil water in the cooling lines. To do this, water feed lines outside of the vacuum chamber are disconnected and purged with some compressed gas at a reasonable pressure. Once the water stops flowing, the cooling lines are capped off to prevent a vacuum breach if a line is compromised during heating. Now the process is similar to the passive freezing valve. 10 Amps are applied to the freezing valve heater and about 5-10 minutes and the thruster is on the thrust stand, a significant change in thrust will be measured when the cooling lines are purged and the anode and reservoir drain.

When the anode has successfully drained, the anode and reservoir heaters are left on for an additional half hour. This evaporates some of the residual bismuth in the anode and also provides the opportunity for any additional bismuth to flow out. When sufficient time has elapsed, all the heaters are turned off and the thruster is cooled under vacuum.

# Appendix.D Copyright Permissions

## COPYRIGHT PERMISSION REQUEST

**TO:** ASM International Permissions  
Ann Britton  
Editorial Assistant  
ASM International  
9639 Kinsman Road  
Materials Park, Ohio 44073-0002 USA  
Phone: + 440 338-5151 ext 5672  
FAX: +440 338-4634  
Email: [Permissions@asminternational.org](mailto:Permissions@asminternational.org)

**FROM:** Complete all contact information  
Your name: Dean Massey  
Title:  
Affiliation: Michigan Technological University  
Address: 1400 Townsend Drive, Houghton MI 49931  
Phone: [REDACTED]  
FAX: [REDACTED]  
Email: dmassey@mtu.edu

I am preparing an article/chapter for publication in the following formats (check as applicable):

Print only                       Internet only                       Print & electronic media

The information will be used for (check as applicable):

Journal article                       Internal company records                       Student Course Material

Conference presentation                       Dissertation                       Commercial Publication\*

The article/chapter title will be: Experimental Development of the Bismuth Thruster  
The publication title will be: Development of a Direct Evaporation Bismuth Hall Thruster  
The publisher is: ProQuest/UMI  
Planned year of publication: 2008                      Book print run: \_\_\_\_\_

I hereby request permission for non-exclusive world rights in the above publication and all subsequent editions, revisions, and derivative works in English and foreign translations, in the formats indicated above for print or any electronic (CD/web) media, from the following copyrighted content by ASM International:

Book ISBN \_\_\_\_\_ Copyright date: \_\_\_\_\_ 1<sup>st</sup> Author Name: \_\_\_\_\_

Book/Publication Title: ASM Alloy Phase Diagram Center (Electronic Database)

Article title: \_\_\_\_\_

Text pages (enclose copy or scan of materials) \_\_\_\_\_

Figure Numbers (with page numbers and copy/scan of figures) Diagram #'s 900432, 901026, 900078, 900129

Table Numbers (with page numbers and copy/scan of tables) 900477, 900435, 900454, 900455, 979635

Please sign this release form below. Sincerely, [REDACTED] Date: 4/21/08

I (we) grant permission requested above. Please ensure that ASM International® receives proper credit as publisher by citing the above ASM publication as a reference, and by including the following: Reprinted with permission of ASM International®. All rights reserved. [www.asmiinternational.org](http://www.asmiinternational.org)

Signed: [REDACTED] Date: 4-21-2008

Re: Figure Permission

**Subject:** Re: Figure Permission  
**From:** Brad King <lbking@mtu.edu>  
**Date:** Tue, 2 Sep 2008 14:50:53 -0400  
**To:** Dean Massey <drmassey@mtu.edu>

You have my permission.

On Sep 2, 2008, at 2:30 PM, Dean Massey wrote:

Brad,  
Do I have your permission to include the Hall thruster diagram from your dissertation?  
It is Figure 1 in my dissertation.

Dean

(They need email proof that it is ok)

--  
-----

Dean Massey  
[REDACTED]

Lyon (Brad) King, Ph.D.  
Michigan Technological University  
815 RL Smith Building  
1400 Townsend Drive  
Houghton, MI 49931

[mtu.edu/researchAreas/isp/index.html](http://mtu.edu/researchAreas/isp/index.html)  
[REDACTED]

## Works Cited

1. Newton, I., *The Principia, A New Translation by I.B Cohen and A. Whitman*. 1999, University of California Press: Berkeley.
2. Larson, W.J., Wertz J.R., *Space Mission Analysis and Design*. 3rd ed. 1999: Microcosm Press.
3. R.W. Humble, G.N.H.a.W.J.L., *Space Propulsion Analysis and Design*. 1995, New York: McGraw-Hill.
4. Griffin, M.D., French, J.R., *Space Vehicle Design*. 1991, Washington DC: AIAA.
5. Jahn, R.G., *Physics of Electric Propulsion*. 1968, New York: McGraw-Hill.
6. Martinez-Sanchez, M., *Spacecraft Electric Propulsion - An Overview*. Journal of Propulsion and Power, 1998. **14**(5).
7. King, L.B., *Transport-Property and Mass Spectral Measurements in the Plasma Exhaust Plume of a Hall-Effect Space Propulsion System*, Ph.D. Dissertation in Aerospace Engineering. 1998, University of Michigan: Ann Arbor. p. 262.
8. Artsimovich, L., Andronov, I., Esipchuk, I., Morozov, A., Snarsky, R., et al, *Development of a stationary plasma thruster (SPT) and its testing on the earth artificial satellite 'Meteor'*. Kosmicheskie Issledovania. **12**(3): p. 451-468 (in Russian).
9. *Busek Promotional Brochure*. [cited.
10. S. Grisnik, J.P., *A Large High Vacuum, High Pumping Speed Space Simulation Chamber for Electric Propulsion*, in *23rd International Electric Propulsion Conference*. 1994: Seattle, WA.
11. *Technology Transfer & Partnership Office: Electric Propulsion Laboratory [at NASA Glenn]*. 2007, NASA Glenn Research Center.
12. *CRC Handbook of Chemistry and Physics 84th Edition*, ed. D.R. Lide. 2003, Boca Raton: Chemical Rubber Publishing Company.
13. Carlin, J.F., *Bismuth*, in *USGS 2006 Minerals Yearbook*. 2006, United States Geological Survey.
14. Mazokin, V.A., *Problems of Dismantling of Multi-Purpose Nuclear Submarines with Liquid-Metal Coolant Reactors*. 2003, International Atomic Energy Agency.
15. Dawson, J.K., *Chemical Aspects of Nuclear Reactors*. 1964, London: Butterworths.
16. Wang, L.L., *Elements of Nuclear Reactor Engineering*. 1974, London: Gordon and Breach Science Publishers.
17. Li, N., *Active control of oxygen in molten lead–bismuth eutectic systems to prevent steel corrosion and coolant contamination*. Journal of Nuclear Materials, 2001. **300**(1): p. 73-81.
18. Muller, G., *Behavior of Steels in Flowing Liquid PbBi Eutectic Alloy at 420-600 C after 4000-7200 h*. Journal of Nuclear Materials, 2004. **335**(2): p. 163-168.
19. Kammerer, O.F., et al., *Zirconium and Titanium Inhibit Corrosion and Mass Transfer of Steels by Liquid Heavy Metals*. Trans. Met. Soc. AIME; Vol: 212, No. 1, 1958: p. Pages: 20-5.
20. J.J. Park, J.J.B., *Selection of Flowing Liquid Lead Target Structural Materials for Accelerator Driven Transmutation Applications*, in *International Conference on Accelerator Driving Transmutation Technologies and Applications*. 1994: Las Vegas, NV.
21. P. Roy, M.K.S., *An analysis of corrosion of steels by liquid sodium*. Journal of Nuclear Materials, 1973. **47**(1).

22. B. F. Gromov, Y.S.B., E. I. Yefimov, M. P. Leonchuk, P. N. Martinov, Yu. I. Orlov, D. V. Pankratov, Yu. G. Pashkin, G. I. Toshinsky, V. V. Chekunov, B. A. Shmatko and V. S. Stepanov, *Use of lead-bismuth coolant in nuclear reactors and accelerator-driven systems*. Nuclear Engineering and Design 1997. **173**: p. 207-217.
23. Forsberg, C.W., *Thermal- and Fast-Spectrum Molten Salt Reactors for Actinide Burning and Fuel Production*, in *Global 07: Advanced Nuclear Fuel Cycles and Systems*. 2007, American Nuclear Society: Boise, Idaho.
24. K.D. Weaver, J.S.H., P.E. MacDonald, *Performance Comparison Of Metallic, Actinide Burning Fuel In Lead-Bismuth And Sodium Cooled Fast Reactors*, in *0th International Conference on Nuclear Engineering*. 2001.
25. N. Todreas, P.M., et al, *Design of an Actinide Burning, Lead or Lead-Bismuth Cooled Reactor that Produces Low Cost Electricity*. 2000, Idaho National Engineering and Environmental Laboratory and Massachusetts Institute of Technology University Research Consortium.
26. Hofer, R.R., *Development and Characterization of High-Efficiency, High-Specific Impulse Xenon Hall Thrusters*, Ph.D. Dissertation in *Aerospace Engineering*. 2004, University of Michigan: Ann, Arbor.
27. J.L. Ross, L.B.K., *Ionization Efficiency in Electric Propulsion Devices*, in *30th International Electric Propulsion Conference*. 2007: Florence, Italy.
28. Larson, C.W., Brown, D. L., and Hargus, W. A., *Thrust Efficiency, Energy Efficiency, and the Role of the VDF in Hall Thruster Performance Analysis*, in *43rd AIAA/ASME/SAE/ASEE Joint Propulsion Conference and Exhibit*. 2007: Cincinnati, Ohio.
29. Hofer, R.R., Gallimore, A.D., *Efficiency Analysis of a High-Specific Impulse Hall Thruster*, in *40th AIAA/ASME/SAE/ASEE Joint Propulsion Conference & Exhibit*. 2004: Ft. Lauderdale, Florida.
30. Kim, V., *Main physical features and processes determining the performance of stationary plasma thrusters*. Journal of Propulsion and Power, 1998. **14**(5).
31. R.S. Freund, R.C.W., R.J. Shul and T.R. Hayes, *Cross-section measurements for electron-impact ionization of atoms*. Journal of Physical Review A, 1990. **41**(7).
32. D. Staack, Y.R.a.N.J.F., *Temperature Gradient in Hall Thrusters*. Applied Physics Letters, 2004. **84**(16).
33. D. Manzella, D.J., *Investigation of Low-Voltage / High-Thrust Hall Thruster Operation*, in *39th Joint Propulsion Conference*. 2003: Huntsville, Alabama.
34. D.H. Manzella, R.S.H.a.R.R.H., *Laboratory Model 50kW Hall Thruster*, in *38th AIAA Joint Propulsion Conference*. 2002: Indianapolis, Indiana.
35. Grishin, D.S., Efofeev, V.S., Zharinov, A.V., Naumkin, V.P. and Safronov, I.N., *Characteristics of a Two-Stage Ion Accelerator with an Anode Layer*. Zhurnal Prikladnoi Mekhaniki i Tekhnicheskoi Fiziki, 1978. **2**: p. 28-36.
36. Choueiri, E.Y., *A Critical History of Electric Propulsion: The First 50 Years (1906–1956)*. Journal of Propulsion and Power, 2004. **20**(2).
37. Tverdokhlebov, S., Semenkin, A., Polk, J., *Bismuth Propellant Option for Very High Power TAL Thruster*, in *38th AIAA/ASME/SAE/ASEE Joint Propulsion Conference*. 2002: Indianapolis, IN.
38. Jankovsky, R., McLean, C., and McVey, J., *Preliminary Evaluation of a 10kW Hall Thruster*, in *35th Annual Joint Propulsion Conference*. 1999: Los Angeles.

39. Tverdokhlebov, O.S., Tverdokhlebov, S.O., Semenkin, A., *An Overview of the TsNIMASH / TsE efforts under VHITAL Program*, in *29th International Electric Propulsion Conference*. 2005: Princeton University, Princeton NJ.
40. Tverdokhlebova, S.A., Tverdokhlebov, O.S., *VHITAL-160 Thermal Model Building and 3D Thermal Modeling Carrying-out*, in *29th International Electric Propulsion Conference*. 2005: Princeton University, Princeton, NJ.
41. Markusic, T.E., Polzin, K.A., Dehoyos, A., *Electromagnetic Pumps for Conductive-Propellant Feed Systems*, in *29th International Electric Propulsion Conference*. 2005: Princeton University, Princeton NJ.
42. Markusic, T.E., Polzin, K.A., Stanojev, B.J., Dodson, C., and Dehoyos, A., *Liquid Metal Flow Sensors for Electric Propulsion*, in *JANNAF*. 2005, CPIC: Monterey, CA.
43. Polzin, K.A., Markusic, T.E., Stanojev, B.J. and Marrese-Reading, C., *Integrated Liquid Bismuth Propellant Feed System*, in *42nd AIAA/ASME/SAE/ASEE Joint Propulsion Conference & Exhibit*. 2006: Sacramento, CA.
44. Marrese-Reading, C., Swindlehurst, R., Owens, A., Markusic, T., Polizin, K., Knowles, T., and Mueller, J., *The Development of a Bismuth Feed System for the Very High Isp Thruster with Anode Layer (VHITAL) Program*, in *42nd AIAA/ASME/SAE/ASEE Joint Propulsion Conference & Exhibit*. 2006: Sacramento, CA.
45. J. Szabo, C.G., V. Hrubby, M. Robin, *Bismuth Hall Effect Thruster Development*, in *JANNAF*. 2005, CPIC: Monterey, CA.
46. Zakharenkov, L., Semenkin, A., *Development and Study of the Very High Specific Impulse Bismuth TAL*, in *30th International Electric Propulsion Conference*. 2007: Florence, Italy.
47. Gambosi, T., *Gasketic Theory*. 1994, Cambridge: Cambridge University Press.
48. Jankovsky, R., Tverdokhlebov, S., and Manzella, D., *High Power Hall Thrusters*, in *35th AIAA Joint Propulsion Conference*. 1999: Los Angeles, CA.
49. T. Reynolds, L.K., *Gas Flow, Emittance, and Ion Current Capabilities of Porous Tungsten*. NASA Technical Note, 1961. **D(871)**: p. 1-44.
50. *Aerojet website, 2003*.
51. Haag, T.W., *Thrust stand for high-power electric propulsion devices*. Review of Scientific Instruments, 1991. **62(5)**.
52. Y. Raitses, L.A.D., A. A. Litvak, and N. J. Fisch, *Plume Reduction in Segmented Electrode Hall Thruster*. Journal of Applied Physics, 2000. **88(3)**.
53. N. J. Fisch, a.Y.R., b) L. A. Dorf, and A. A. Litvak, *Variable operation of Hall thruster with multiple segmented electrodes*. Journal of Applied Physics, 2001. **89(4)**.
54. Y. Raitses, D.S.a.N.J.F., *Plasma Characterization of Hall Thruster with Active and Passive Segmented Electrodes*, in *38th AIAA/ASME/SAE/ASEE Joint Propulsion Conference*. 2002: Indianapolis, IN.
55. Kieckhafer, A., *The Effect of Segmented Anodes on the Performance and Plume of a Hall Thruster*, Doctoral Dissertation in *Mechanical Engineering-Engineering Mechanics*. 2007, Michigan Technological University: Houghton. p. 144.
56. Chakrabarti D.J., a.L.D.E., *Binary Alloy Phase Diagrams*. Vol. 1. 1990.
57. German, R.M., *Sintering Theory and Practice*. 1996, New York: Wiley.
58. Headly, L.C., *Status of Porous Ionizers for Contact Ionization of Cesium*. NASA Technical Note, 1967. **D-3997**.
59. Saunders, N., *Experimental Method of Producing Porous Tungsten for Ion Rocket Engines*. NASA Technical Note, 1961. **D(864)**: p. 1-23.

60. D.L. Lockwood, R.J.C., *Performance Evaluation of a Two-Dimensional Ion Rocket Using Through-Feed and Porous Tungsten Ionizers*. NASA Technical Note. **TN(D-766)**.
61. A. V. Pustogaro, G.N.M.n., V. V. Glagolev, M. A. Fedotov, I. N. Aleinikov and D. D. Chepiga, *High-Temperature Properties of of Porous Tungsten and Molybdenum*. Soviet powder metallurgy and metal ceramics, 1975. **14**(10): p. 867.
62. Association, I.M., *Molybdenum*. 1998, BSC Print Ltd: London.
63. P. Garg, S.J.P., R.M. German, *Effect of die compaction pressure on densification behavior of molybdenum powders*. International Journal of Refractory Metals & Hard Materials, 2007. **25**(16-24).
64. O Kubaschewski, B.H., *Oxidation of Metals and Alloys*. 1962, London: Butterworths.
65. Tei SABURI, H.M., Tatsuya SUZUKI, Yasuhiko FUJII and Kiyoshi KIUCHI, *Oxygen Plasma Interactions with Molybdenum: Formation of Volatile Molybdenum Oxides*. Journal of Plasma and Fusion Research, 2002. **78**(1).
66. Tudbury, C.A., *Basics of Induction Heating*. Vol. New Rochelle, NY. 1960: John F. Rider, Inc.
67. Zhang, C., Van Hove, M.A., Somorjai, G.A., *The Interaction of Oxygen With the Molybdenum(100) and Molybdenum(111) Single-Crystal Surfaces: Chemisorption and Oxidation at High Temperatures* Surface Science, 1985. **149**(2-3): p. 326-340.
68. A. V. Savin, N.D.S.a.L.S.V., *Shaping and growth of tungsten oxide and molybdenum oxide crystals during annealing and reduction*. Powder Metallurgy and Metal Ceramics, 1968. **10**(7): p. 568-572.
69. J. Goldstein, D.N., et al, *Scanning Electron Microscopy and X-ray Microanalysis*. 2003, New York: Springer.
70. H. McCracken, J.B., *Electron Beam Welding of High Temperature Thrusters for Spacecraft Propulsion Systems*, in *22nd ASME, SAE, and ASEE, Joint Propulsion Conference*. 1986, AIAA: Huntsville, AL.
71. Hutchinson, I.H., *Principles of Plasma Diagnostics*. 2002, Cambridge: Cambridge University Press.
72. Karakaya I., a.T.W.T., *The Ag-Bi (Silver-Bismuth) System*. J. Phase Equilib, 1993. **14**: p. 525-530.
73. McAlister, A.J., *Binary Alloy Phase Diagrams*. 2nd ed, ed. T.B. Massalski. 1990.
74. Okamoto, H., *Binary Alloy Phase Diagrams*. 2nd ed, ed. T.B. Massalski. Vol. 1. 1990.
75. Nash, P., *Binary Alloy Phase Diagrams*. 2nd ed, ed. T.B. Massalski. Vol. 1. 1990.
76. Murray, J.L., *Binary Alloy Phase Diagrams*. 2nd ed, ed. T.B. Massalski. Vol. 2. 1990.
77. Allan Ferguson, E.I., *On Surface Energy and Surface Entropy*. Proc. Phys. Soc, 1940. **53**(2): p. 182-185.